Stony Brook University

Growth Mechanisms and Defect Structures of $B_{12}As_2$ Epilayers

Grown on 4H- and 6H-SiC Substrates

A Dissertation Presented

by

Yu Zhang

to

The Graduate School

in Partial Fulfillment of the

Requirements

for the Degree of

Doctor of Philosophy

in

Materials Science and Engineering

Stony Brook University

May 2011

Stony Brook University

The Graduate School

Yu Zhang

We, the dissertation committee for the above candidate for the

Doctor of Philosophy degree, hereby recommend

acceptance of this dissertation.

Michael Dudley – Dissertation Advisor
Professor, Chair, Department of Materials Science and Engineering

Jonathon Sokolov - Chairperson of Defense
Professor, Department of Materials Science and Engineering

Balaji Raghothamachar
Research Assistant Professor, Department of Materials Science and Engineering

Dong Su
Associate Scientist, Center for Functional Nanomaterials
Brookhaven National Laboratory

This dissertation is accepted by the Graduate School

Lawrence Martin
Dean of the Graduate School

Abstract of the Dissertation

Growth Mechanisms and Defect Structures of $B_{12}As_2$ Epilayers

Grown on 4H- and 6H-SiC Substrates

by

Yu Zhang

Doctor of Philosophy

in

Materials Science and Engineering

Stony Brook University

2011

As a member of icosahedra boride family of materials, icosahedral boron arsenide ($B_{12}As_2$)**,** with a wide band gap of 3.2eV at room temperature, possesses extraordinary resistance against radiation damage mediated via a "self-healing" mechanism which makes it attractive for applications in high radiation environments. Such properties could potentially be exploited in developing high-power beta-voltaic cells which are capable of converting nuclear power into electrical energy. In addition, $B_{12}As_2$ has exceptional mechanical properties, high melting point and large Seebeck coefficient at high temperatures which make it promising for the fabrication of high temperature thermoelectronics. Lastly, $B_{12}As_2$ has also attracted considerable attention as a potential material for compact solid-state neutron detectors due to the neutron-absorbing ability of the $_{10}B$ isotope.

The absence of native substrates necessitates the growth of $B_{12}As_2$ via heteroepitaxy on non-native substrates with compatible structural parameters. To date, growth on Si substrates with (100), (110) and (111) orientation, on (11-20) and (0001) 6H-SiC substrates has been attempted. However, degenerate epitaxy, manifested by the presence of high densities of twin boundaries (rotational variants), was observed in the epilayers in all of these cases and is

expected to have a detrimental effect on device performance which has severely hindered progress of this material to date. $B_{12}As_2$ epilayers grown on a variety of 4H- and 6H-SiC substrates were studied using synchrotron white beam X-ray topography, high resolution transmission electron microscopy, scanning transmission electron microscopy as well as other characterization techniques. High quality single crystalline $B_{12}As_2$ epilayers and the elimination of degenerate epitaxy in the growth of $B_{12}As_2$ were achieved on 4H-SiC substrates intentionally misoriented from (0001) towards [1-100] and the growth mechanisms were proposed. The influence of the defect structures in $B_{12}As_2$ films on their physical properties was also investigated. The goals of the studies are to understand the growth mechanisms and defect structures present in $B_{12}As_2$ epitaxial films so as to develop strategies to reduce defect densities, obtain single crystalline epilayers and better film quality for future device fabrications. The following detailed studies have been carried out:

1) The defect structures in $B_{12}As_2$ epitaxial layers grown at two different temperatures on on-axis (0001) 6H-SiC by chemical vapor deposition (CVD) was studied using synchrotron white beam x-ray topography (SWBXT) and high resolution transmission electron microscopy (HRTEM). SWBXT reveals the observed epitaxial relationship of (111) $_{B12As2}$ $<10\text{-}1>_{B12As2}$‖ (0001) $_{6H\text{-}SiC}$ $<11\text{-}20>$ $_{6H\text{-}SiC}$ and the presence of $B_{12}As_2$ twins in both samples. Cross-sectional HRTEM observation reveals the different twinned structures of the $B_{12}As_2$ epilayers in the samples. The observed differences in microstructures were correlated with the differences in nucleation at the two growth temperatures arising from the "lock-and-key" effect. The effect of the difference in microstructure on macroscopic properties of the $B_{12}As_2$ was illustrated using the example of thermal conductivity which was measured using the 3-ω technique.

2) Investigation on the nucleation mechanism of 6H-SiC polytype inclusions in physical vapor transport (PVT) grown 15R-SiC boules. Synchrotron white beam and monochromatic beam X-ray topography and HRTEM were employed in this investigation. Inhomogeneous densities of screw dislocations replicated from the 15R-SiC seed lead to uneven growth rates resulting in a quasi-vicinal growth surface. Subsequent interference between advancing vicinal growth steps and screw dislocation spiral growth steps lead to complex step overgrowth processes which can suppress all or part of the 15R 1c screw dislocation Burgers vector through the creation of Frank faults and Frank partial dislocations on the basal plane. Combined with stacking shifts induced by the passage of basal plane partial dislocations, it is shown that

suppression of 9/15 of the 15R 1c dislocation Burgers vector by such step overgrowth can leave behind a residual Burgers vector corresponding to a 1c dislocation in 6H-SiC. This residual dislocation then acts as a nucleus for reproduction of the 6H-SiC structure at the surface of the 15R-SiC crystal. Competition between the 6H-SiC nucleus and the surrounding 15R-SiC matrix eventually leads to lenticular shaped 6H-SiC inclusions approximately parallel to the 15R-SiC basal plane.

3) The microstructures of $B_{12}As_2$ epitaxial layers grown on on-axis c-plane 4H-SiC substrates were studied using characterization techniques composed of SWBXT, scanning electron microscopy (SEM), HRTEM and scanning transmission electron microscopy (STEM). SWBXT and SEM revealed a mosaic structure consisting of a solid solution of matrix and twin epilayer domains. The epitaxial relationship was determined to be $(111)_{B12As2}$ $<1\text{-}21>_{B12As2}\|$ $(0001)_{4H\text{-}SiC}$ $<1\text{-}100>_{4H\text{-}SiC}$. $B_{12}As_2$ twinned domains were found in the epilayer and the twinning relationship was consisted of a 180° rotation about $[0001]_{B12As2}$. HRTEM observations reveal that the transition layer was suggested to arise from the coalescence of different domains of translational and rotational variants nucleated at the various nucleation sites on the on-axis (0001) 4H-SiC surface. Boundaries between domains of translational variant were shown to have unfavorable high-energy bonding configurations while the formation of a 1/3[0001] $B_{12}As_2$ Frank partial dislocation enabled the elimination of the high energy boundaries during mutual overgrowth process. Consequently, the film quality beyond thickness of ~20nm can be improved as the translational variants grow out leaving only the rotational variants. (0003) twin boundaries in the regions beyond 20nm are shown to possess fault vectors such as $1/3[1\text{-}100]_{B12As2}$ which originates from the mutual shift between the different nucleation sites of the respective adjacent domains.

4) Investigation of $B_{12}As_2$ epitaxial layers grown on (0001) 4H-SiC substrates intentionally misoriented from (0001) towards [1-100] using SEM, SWBXT, HRTEM and STEM. SWBXT revealed that only one orientation of $B_{12}As_2$ was present in the epitaxial layer, which was grown along (111) surface normal. The SWBXT also revealed that $B_{12}As_2$ diffraction spots have much better-defined shapes compared to those grown on other SiC substrates. This indicates the film grown on off-axis (0001) 4H-SiC substrate is highly single crystalline and has much higher quality. Cross-sectional HRTEM also confirmed the presence of only one orientation in the $B_{12}As_2$ grains grown along (111) surface normal. It is proposed that the single

crystalline, untwinned nature of the $B_{12}As_2$ film resulted from the tendency to nucleate on the isolated junctions between close-packed (-3304) step risers and (0001) terraces present on the hydrogen etched off-axis 4H-SiC substrate surface.

Elimination of the effects of degenerate epitaxy in the $B_{12}As_2$ films were also analyzed by using off-axis (0001) 4H-SiC substrates. Ease of nucleation on this unique substrate with ordered step structures overrides symmetry considerations and dominates the nucleation process of $B_{12}As_2$.

Table of Contents

List of Figures

List of Abbreviations

B	boron
As	arsenic
Si	silicon
C	carbon
CVD	chemical vapor deposition
HRTEM	high resolution transmission electron microscopy
STEM	scanning transmission electron microscopy
SAD	selective area diffraction
SEM	scanning electron microscope
SWBXT	synchrotron white beam X-ray topography
TEM	transmission electron microscopy
SS	spiral step
VS	vicinal step
TSD	threading screw dislocation
TED	threading edge dislocation
BPD	basal plane dislocation

List of Symbols

A	site A in the ABC layered structure
B	site B in the ABC layered structure
C	site C in the ABC layered structure
d	lattice spacing of crystallographic plane
f	focus condition in HRTEM

Acknowledgments

First I would like to give my deep and sincere gratitude to Professor Michael Dudley, my Ph.D. advisor, for providing me this great opportunity to work in the field of semiconductor characterization. His wide knowledge and helpful guidance have been of great value for me. No doubt his understanding, encouragement and personal guidance have always been providing an excellent basis for my Ph.D. research.

Second, I would like to thank Professor Jonathan Sokolov and Balaji Raghothamachar, for being my defense committee members.

I would like to thank Dr. Dong Su for being my defense committee member and his invaluable help on HRTEM and STEM experiments. And thanks to Dr. Lihua Zhang for her great help on HRTEM experiments.

I would like to thank Professor James H. Edgar and his research group for supplying useful samples and instructive discussions on the epitaxial growth of $B_{12}As_2$. Thanks are also given to Professor Martin Kuball and his research group for their collaboration in measuring the physical properties of $B_{12}As_2$ samples and device-related research.

I would also like to thank my colleagues: Dr. Hui Chen, Mr. Vishwanath Sakar, Mr. Fangzhen Wu, Ms. Huanhuan Wang, Ms. Mengjia Gaowei, Mr. Shayan Byrappa, Ms. Gloria Choi and Ms. Shun Sun for their help during my research.

Financial support from the National Science Foundation Materials World Network Program under Grant No.0602875 and by the Engineering and Physical Science Research Council (EPSRC) under Grant No. EP/D075033/1 under the NSF-EPSRC Joint Materials Program is acknowledged. The SWBXT work was carried out at Stony Brook Topography Facility (Beamline X19C) at the National Synchrotron Light Source (NSLS), Brookhaven National Laboratory (BNL), which is supported by the U.S. Department of Energy (D.O.E.) under Grant No. DE-AC02-76CH00016. TEM and STEM was carried out at the Center for Functional Nanomaterials (CFN), BNL, which is supported by the U.S. Department of Energy, Office of Basis Energy Science, under Contract No. DE-AC02-98CH10886.

Publications

1. **Y. Zhang,** H. Chen, M. Dudley, Y. Zhang, J. H. Edgar, Y. Gong, S. Bakalova, M. Kuball, L. Zhang, D. Su, Y. Zhu, "Elimination of Degenerate Epitaxy in the Growth of High Quality $B_{12}As_2$ Single Crystalline Epitaxial Films", *Mater. Res. Soc. Symp. Proc.*, to be published
2. C.E. Whiteley, **Y. Zhang**, A. Mayo, J.H. Edgar, Y. Gong, M. Kuball, and M. Dudley, "Solution Growth and Characterization of Icosahedral Boron Arsenide ($B_{12}As_2$)", *Mater. Res. Soc. Symp. Proc.*, to be published
3. C.E. Whiteley, A. Mayo, J.H. Edgar, M. Dudley and **Y. Zhang**, "Defect-Selective Etching of Icosahedral Boron Arsenide ($B_{12}As_2$) Crystals in Molten Potassium Hydroxide", *Mater. Res. Soc. Symp. Proc.*, to be published
4. **Y. Zhang**, H. Chen, G. Choi, B. Raghothamachar, M. Dudley, J. H. Edgar, K. Grasza, E. Tymicki, L. Zhang, D. Su, Y. Zhu, "Nucleation Mechanism of 6H-SiC Polytype Inclusions inside 15R-SiC Crystals", *J. Electron. Mater.*, Vol. 39, No. 6 (2010)
5. **Y. Zhang**, H. Chen, M. Dudley, Y. Zhang, J.H. Edgar, Y. Gong, S. Bakalova, M. Kuball, L. Zhang, D. Su, K. Kisslinger, and Y. Zhu, "Mechanism for Improved Quality $B_{12}As_2$ Epitaxial Films on (0001) 4H-SiC Substrates Offcut towards [1-100]," *Mater. Res. Soc. Symp. Proc.*, Vol. 1246, Warrendale, PA (2010)
6. Y. Gong, **Y. Zhang**, M. Dudley, Y. Zhang, J.H. Edgar, and M. Kuball, "Demonstration of Boron Arsenide Heterojunctions: A Radiation Hard Wide Band Gap Semiconductor Device", *App. Phys. lett.*, Vol. 96, Issue: 22, Article Number: 223506 (2010)
7. Y. Gong, **Y. Zhang**, M. Dudley, Y. Zhang, J. H. Edgar, P. J. Heard, and M. Kuball, "Thermal Conductivity and Seebeck Coefficients of Icosahedral Boron Arsenide Films on Silicon Carbide", *J. Appl. Phys.*, 108, 1 (2010)
8. S. Bakalova, Y. Gong, C. Cobet, N. Esser, Y. Zhang, J. H. Edgar, **Y. Zhang**, M. Dudley, and M. Kuball, "Energy Band Structure and Optical Response Function of Icosahedral $B_{12}As_2$: A Spectroscopic Ellipsometry and First-Principles Calculational Study", *Phys. Rev. B* 81, 075114 (2010)
9. S. Bakalova, Y. Gong, C. Cobet, N. Esser, Y. Zhang, J. H. Edgar, **Y. Zhang**, M. Dudley and M. Kuball, "Electronic Excitations in $B_{12}As_2$ and Their Temperature Dependence by

Vacuum Ultraviolet Ellipsometry", *J. Phys.: Condens. Matter* 22, 395801 (2010)

10. M. Dudley, N. Zhang, **Y. Zhang**, B. Raghothamachar and E. K. Sanchez, "Nucleation of C-axis Screw Dislocations at Substrate Surface Damage During 4H-Silicon Carbide Homo-Epitaxy", *Mater. Sci. Forum*, Vol. 645-648, pp 295-298 (2010)
11. M. Dudley, N. Zhang, **Y. Zhang**, B. Raghothamachar, S. Byrappa, G. Choi, E. K. Sanchez, D. Hansen, R. Drachev and M. J. Loboda, Characterization of 100 mm Diameter 4H-Silicon Carbide CrystalsWith Extremely Low Basal Plane Dislocation Density*Mater. Sci. Forum*, Vol. 645-648, pp 291-294 (2010)
12. M. Dudley, S. Byrappa, H. Wang, F. Wu, **Y. Zhang**, B. Raghothamachar, G. Choi, E. K. Sanchez, D. Hansen, R. Drachev, and M.J. Loboda, "Analysis of Dislocation Behavior in Low Dislocation Density, PVT-Grown, Four-Inch Silicon Carbide Single Crystals", *Mater. Res. Soc. Symp. Proc.*, Vol. 1246, Warrendale, PA (2010)
13. **Y. Zhang**, H. Chen, N. Zhang, M. Dudley, Y. Gong, M. Kuball, Z. Xu, Y. Zhang, J.H. Edgar, L. Zhang, and Y. Zhu, "Origins of Twinned Microstructures in $B_{12}As_2$ Epilayers Grown on (0001) 6H-SiC and Their Influence on Physical Properties", *Mater. Res. Soc. Symp. Proc.*, Vol. 1164, Warrendale, PA (2009)
14. N. Zhang, Y. Chen, **Y. Zhang**, M. Dudley and R.E. Stahlbush, "Nucleation Mechanism of Dislocation Half-loop Arrays in 4H-silicon Carbide Homoepitaxial Layers", *Appl. Phys. Lett.*, 94, 122108 (2009)

Fields of Study

This section summarizes my major research fields and accomplishments. Growth mechanisms and defect structures of $B_{12}As_2$ epilayers on various SiC substrates have been studied in depth. Based on the numerous results obtained during my research work, the most significant accomplishments which are expected to have the biggest impact on the crystal growth process and the semiconductor industry as well as those constituting major contributions to techniques for semiconductor characterizations are summarized below.

1) Detailed studies at the atomic level of growth mechanisms and defect structures in the $B_{12}As_2$ films on a series of SiC substrates have been carried out using the combined characterization techniques of Normaski optical microscopy, scanning electron microscopy, synchrotron white beam X-ray topography, high resolution transmission electron microscopy and scanning transmission electron microscopy. Epitaxial relationships corresponding to the growth on different substrates have been determined which provide the basic understanding to study and compare the differences between the growth mechanisms of $B_{12}As_2$ on different substrates.

2) Based on the TEM and STEM observation combined with HRTEM simulations from previous reports, structural projections of $B_{12}As_2$ atomic structures have been accurately assigned to the atomic features observed in the HRTEM and STEM images and simulated using the crystal visualization software, CrystalMaker and CaRine 4.0. This enables the detailed investigation of defect structures in the $B_{12}As_2$ films grown on the various types of SiC substrates at an atomic resolution and provides a deeper insight into the growth mechanisms of these films by considering the surface step configurations of the substrate after hydrogen etching and the mutual bonds between $B_{12}As_2$ and SiC.

3) The difference in microstructures of $B_{12}As_2$ epilayers grown under different conditions was compared and correlated with the physical properties of the epilayers. This provides the first insight into the influence of defect structures of $B_{12}As_2$ epilayer on its physical properties and thus the device performance. In addition, it gives guidance to the growth process to produce samples that meet specific application requirements.

4) The detailed investigation on the polytype inclusions and defect structures of SiC substrates has been carried out. A new model of the nucleation mechanisms of 6H-SiC polytype

inclusions in the 15R-SiC boule have been proposed. It is shown that inhomogeneous densities of screw dislocations replicated from the seed lead to uneven growth rates in the boule resulting in a quasi-vicinal growth surface. Subsequent interference between advancing vicinal growth steps and screw dislocation spiral growth steps lead to complex step overgrowth processes. Combined with stacking shifts induced by the passage of basal plane partial dislocations it is shown that suppression of 9/15 of the 15R 1c dislocation Burgers vector by such step overgrowth can leave behind a residual 1c dislocation in 6H-SiC. The residual dislocation then acts as a nucleus for reproduction of the 6H-SiC structure at the surface of the 15R crystal. This model illustrates the nucleation mechanisms of polytype inclusions in the growth of SiC crystals, provides strategies to eliminate impurities in the growth process and is possible to be extended to the study of other crystalline materials with similar structures.

5) High-quality single crystalline $B_{12}As_2$ grown on c-plane 4H-SiC with offcut toward [1-100] direction has been discovered. A model illustrating the unique step structures of the substrate surface and the atomic bonding configurations across the film/substrate interface has been constructed to interpret single growth orientation of $B_{12}As_2$ on this off-axis c-plane 4H-SiC substrate with specific offcut direction. This shreds much light on improving the film quality by choosing a potentially excellent and commercially available substrate, such as 4H-SiC with offcut toward [1-100] direction. The strategies to eliminate degenerate epitaxy are also studied and summarized. It is proposed that the absence of degenerate epitaxy is attributed to the introduced vicinality of c-plane 4H-SiC substrate with offcut toward [1-100] direction. This sheds much light on the growth process of epitaxial materials by choosing the suitable substrates and provides a feasible solution to eliminate the negative effect of degenerate epitaxy on crystal growth and device fabrications.

1. Introduction

1.1. Background of $B_{12}As_2$

The broad applications of wide bandgap semiconductors in the semiconductor fields of high frequency and high power electronics, short wavelength optoelectronics, and chemical, biological and radiation detectors/sensors have led to an explosion of research into SiC [1], AlN, GaN [2] and ZnO [3], etc. However, boron-based wide bandgap semiconductor materials have not been given much attention especially the icosahedral boron-rich compound materials, such as α-boron (B_{12}), $B_{12}As_2$, $B_{12}P_2$ and $B_{12+x}C_{3-x}$. These icosahedral borides with a three-fold symmetric rhombohedral structure hold a special place within chemistry and do not follow the ordinary general bonding rules [4]. Their structures are based on twelve-boron-atom icosahedral clusters residing at the corners of an α-rhombohedral unit cell. Each boron atom occupies a vertex of an icosahedron, and is bonded to five other B atoms as well as either a foreign atom or another icosahedron [4, 5]. The internal bonding of the boron icosahedron is based on an electron-deficient three-center bonding mechanism in which two electrons are shared among three boron atoms. This unique structure and the outstanding strength of the three-center bonding endow these icosahedral boride materials extraordinary mechanical property, high melting temperature and other outstanding properties.

$B_{12}As_2$ is an important member of the icosahedral boride family of materials based on icosahedral clusters of boron atoms and two-atom As-As chains lying along the rhombohedral [111] axis as shown in Figure 1 in two different viewing directions. $B_{12}As_2$ has a wide band gap of 3.2eV [6, 7], high melting point of around 2027 ℃ [8], exceptional mechanical properties and large Seebeck coefficient at high temperatures, which make it promising for the fabrication of high temperature thermoelectronics [9].

In addition, $B_{12}As_2$ possesses extraordinary resistance against radiation damage mediated via a "self-healing" mechanism which makes it attractive for applications in high radiation environments [4, 5, 10-13]. In a study of electron irradiation of a series of boron compounds, Carrard et al demonstrated that neither defect clusters nor amorphization occurs in compounds containing boron icosahedra (twelve boron atom clusters) [10]. Regardless of the electron energy or flux employed (as high as to displace all boron atoms for seven times), no obvious new

defects were observed in the crystals by HRTEM. This surprising characteristic was attributed to the strong Coulombic attraction between positively charged boron interstitial ions and negatively charged regions formed by degraded boron icosahedra. This self-healing property has also been verified through irradiation by heavy (i.e. argon) and light (i.e. helium) atoms at both low and room temperatures. Figure 2 shows a representative example of HRTEM micrographs from identical micro-structural regions of $B_{12}As_2$ before and after a 0.55 MeV electron beam bombardment at a dose of ~$1x10^{17}$ cm^{-2} as well as from $B_{12}As_2$ samples irradiated by neutrons. No permanent point defects are observed by HRTEM, i.e., were induced by the irradiation in the investigated sample areas.

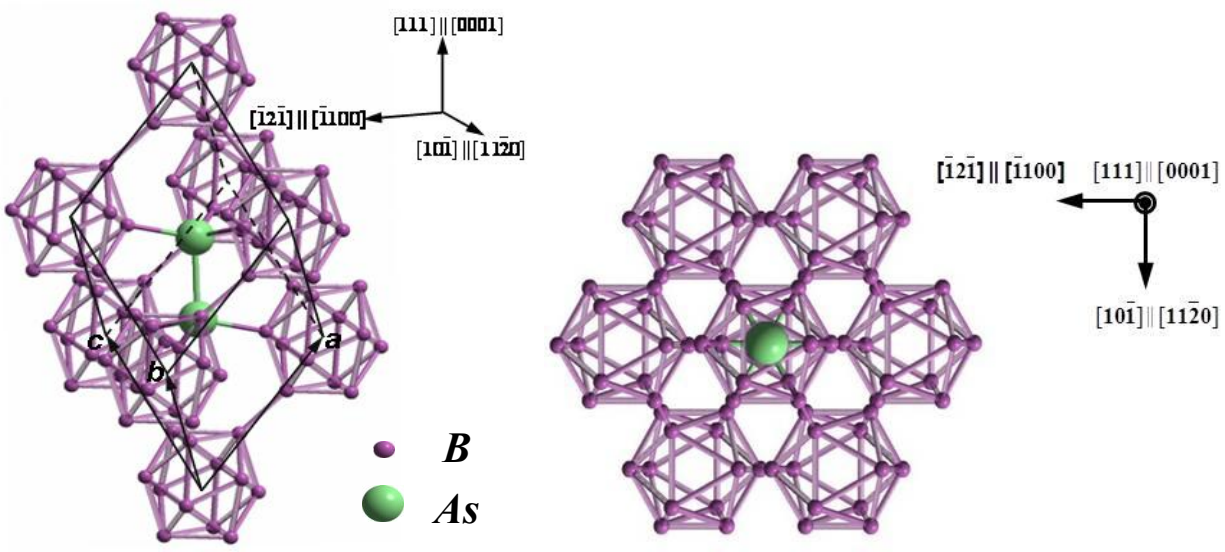

(a) (b)

Figure 1 (a) Side view of $B_{12}As_2$ unit cell showing twelve-atom-boron icosahedra (B atoms are the smaller spheres) and an two-atom As-As chain lying along [111] direction (As atoms are the larger spheres). The structure can be equivalently referred to either a rhombohedral or hexagonal unit cell. *a*, *b* and *c* indicate the rhombohedral unit cell axes. The [111], [1-21] and [10-1] directions are referred to the rhombohedral cell, which are equivalent to [0001], [1-100] and [11-20] directions, respectively, in the hexagonal cell. (b) Plan view of the atomic structure of $B_{12}As_2$ unit cell.

Such properties could potentially be exploited in developing high-power and high-energy-capacity beta-voltaic cells which are capable of directly converting nuclear power into electrical energy by coupling a radioactive beta emitter to a rectifying semiconductor junction (Figure 3) [14, 15]. Such devices, as self-contained and reliable energy source, are analogous to a photovoltaic cell, with the nuclear source replacing sunlight as the energy source. Beta particles (essentially electrons) travelling through a depletion layer can create electron-hole pairs that are

collected in an external circuit. Such nuclear to electrical conversion is able to take advantage of the orders of magnitude higher energy density in nuclear sources compared to chemical and other sources. For most semiconductor materials, the lifetimes of beta cells are very short due to the accumulation of radiation damage [16]. In the boride semiconductor this problem may be eliminated with increased lifetimes, which are measured on a scale of years rather than days or weeks due to their self-healing property, thus enables the use of high energy density nuclear sources within beta cells.

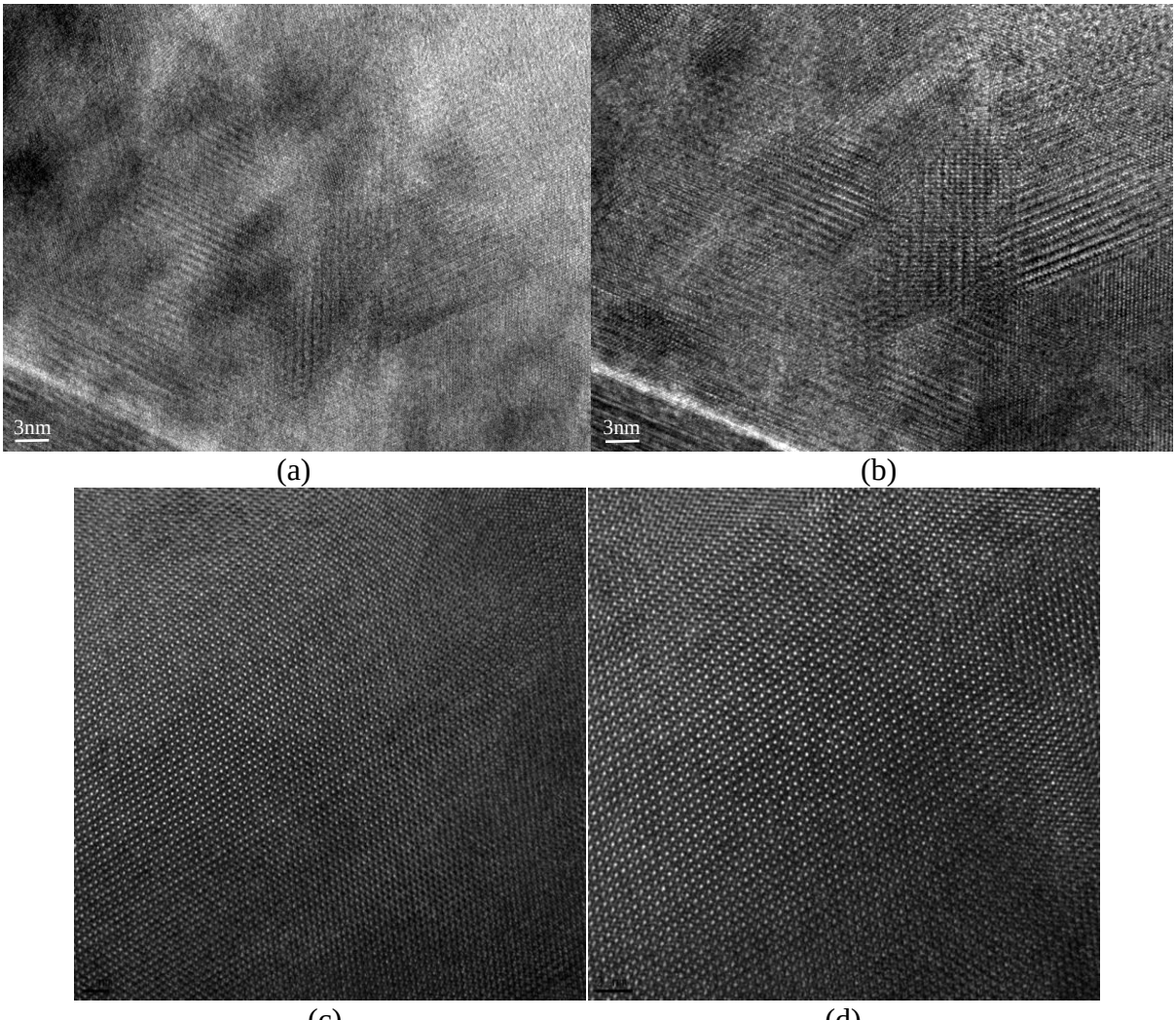

Figure 2 HRTEM micrographs from the identical regions in a $B_{12}As_2$ epitaxial film before (a) and after (b) the bombardment by the electrons with energy of 0.55MeV at a dose of ~$1x10^{17}$ cm^{-2}; HRTEM images of as-grown (c) $B_{12}As_2$ and the sample irradiated by neutrons with a total flux of $2.52x10^{8}$ $cm^{-2}s^{-1}$ for two hours (d).

Lastly, $B_{12}As_2$ has also attracted considerable attention due to the high thermal neutron capture cross-section of the $_{10}B$ isotope, which is 3840 barns. In contrast, most of other elements have values less than 1 barn. Therefore a relatively thin layer of $_{10}B$ containing material is highly effective at capturing neutrons. A boron-based semiconductor could be both a neutron absorber and a detector. Neutrons undergo two reactions with boron atoms which form both $_{7}li$ and alpha particles. The alpha particle has sufficient energy to generate more than 10^5 electron-hole pairs. Collecting even a small fraction of these charge carriers would make the detection of a single neutron event possible [9, 17]. Figure 4 shows a schematic of a $B_{12}As_2$ /SiC heterojunction diode [9].

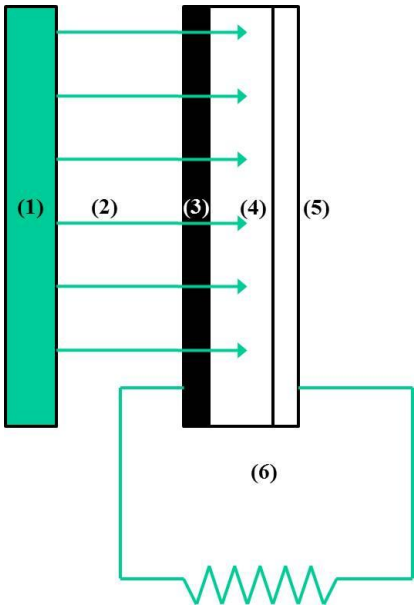

Figure 3 Illustration of an icosahedral boride Schottky barrier device in surface contact with a layer of a beta-emitting radioisotope. (1) beta-emitting radioisotope stratum; (2) beta radiation; (3) thin metal contact which serves as a Schottky barrier (a non-Ohmic contact); (4) icosahedral boride semiconductor; (5) another Ohmic metal contact; (6) device for transmitting the produced electrical energy to a load. (United States Patent No.: US 6,479,919 B1, Nov. 12, 2002)

In the absence of native substrates, foreign substrates with compatible structural parameters are necessary for the growth of $B_{12}As_2$ epitaxial films. Considering the crystal structure of $B_{12}As_2$, although belonging to the space group $\boldsymbol{R\bar{3}m}$ which is a type of rhombohedral structures, it can be represented with a hexagonal cell (a=6.14Å, c=11.91Å) (Figure 5 (a)). This observation suggests the potential for the heteroepitaxial growth of $B_{12}As_2$ on a surface that also possesses hexagonal symmetry. Hexagonal phases of SiC (a=3.08Å), such as

6H-SiC (Figure 5 (b)), have been the substrates of choice to date since they have approximately half of the basal plane lattice constant of $B_{12}As_2$ and attempts to grow $B_{12}As_2$ on on-axis c-, a- and m-plane 6H-SiC have been reported [18, 19]. However, growth of a lower symmetry epilayer on a higher symmetry substrate often produces structural variants (rotational and translational) in the film that are related to each other by a symmetry operation that is present in the substrate but absent in the epilayer. A theoretical treatment of this phenomenon, which has been referred to as degenerate epitaxy [20], was carried out by Flynn and Eades [21]. For the case of $B_{12}As_2$ grown on 6H-SiC of various orientations, rotational and translational variants are both predicted and observed [18, 19], which may have an adverse effect on the electrical properties of $B_{12}As_2$ films.

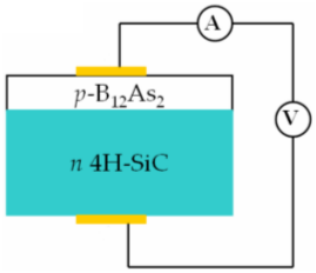

Figure 4 Schematic diode geometry of a $B_{12}As_2$/SiC heterojunction [9].

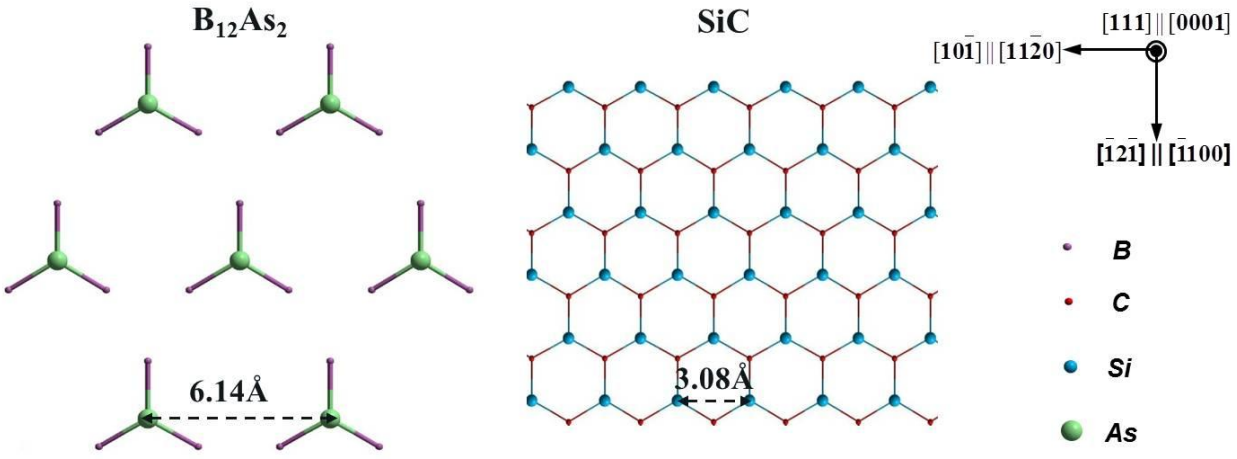

(a) (b)

Figure 5 Plan view of (0001) $B_{12}As_2$ surface and (0001) 6H-SiC surface. The in-plane lattice mismatch between the two materials is around 0.3%.

For films grown on 3.5° off-axis and on-axis (0001) 6H-SiC, Wang *et al* observed polycrystalline grains with preferred orientation of $[0001]_{B12As2}//[0001]_{6H\text{-}SiC}$ and [10-

$10]_{B12As2}$//$[10\text{-}10]_{6H\text{-}SiC}$ [14]. Vetter *et al* confirmed this orientation relationship for films grown on on-axis substrates although double positioning twins were also observed with one occurring more frequently than the other [15]. R. Nagarajan *et al* found that the distribution of double positioning twins varied with different AsH_3:B_2H_6 flow ratios [22]. Michael *et al* theoretically predicted the existence of a number of possible $B_{12}As_2$ structural variants based on the variety of non-equivalent nucleation sites available on the (0001) SiC surface. These were referred to as chemical, translational and rotational variants although this analysis did not take into account the influence of the possible bonding configurations between the $B_{12}As_2$ and the SiC surface, a subject which will be addressed in Chapter 6. Double positioning twins were observed but no evidence was found for any preferred growth. Diffuse boundaries observed within the twin grains were tentatively interpreted as boundaries between translational variants.

1.2. Background of SiC

Silicon carbide (SiC) is steadily replacing conventional semiconductor materials, e.g., silicon (Si) and gallium arsenide (GaAs), under certain extreme applications due to its outstanding properties such as high thermal conductivity, high breakdown voltage and high saturated electron drift velocity.

SiC is noted for its large number of polytypes [23]. Up to now, more than 200 types of phases of SiC have been found [24, 25]. The first SiC structure found is 15R: the same Si-C bilayer repeats every 15 layers with rhombohedral structure, which was labeled arbitrarily as type I; the second one is the hexagonal structure with six-layer repetition labeled as type II; the third one found is 4-layer hexagonal structure labeled as type III. The cubic structure was the fourth one to be discovered, which was naturally labeled as type IV. When more and more structures of SiC were found, it was impractical to keep using this labelling method. L. S. Ramsdell found that the basic unit that SiC is composed of (close-packed Si-C bilayer) is the same for the structures already found and possibly the same for the future structures. The polytypes come from different stacking sequences of the Si-C bilayers. Therefore, Ramsdell created a labelling principle to define the structures already discovered and even for potential structures to be discovered in the future [26]. The label is composed of a number which indicates the number of bilayers in the repeating unit followed by a letter C, H or R corresponding to cubic,

hexagonal or rhombohedral. This is currently the most commonly used nomenclature for SiC polytypes.

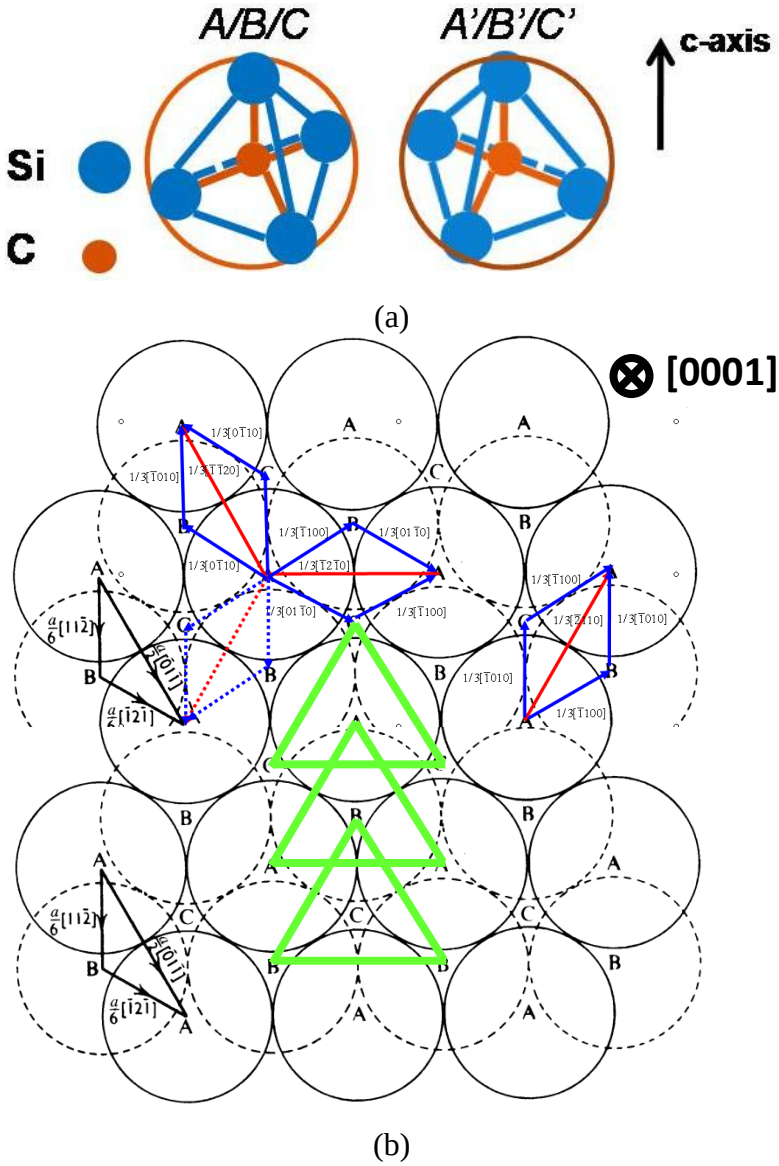

Figure 6 (a) SiC tetrahedra of variants A, B, C and twinned variants A', B' and C'. (b) Three possible sites A, B and C that corner-sharing SiC tetrahedra can occupy on the c-plane.

It is necessary to understand the stacking rules in SiC. The structure of SiC can be considered as an assembly of corner-sharing tetrahedra [27-29]. Every SiC tetrahedron arises from the tetrahedral bondings between silicon and carbon atoms (Figure 6 (a)) and the SiC tetrahedra are joined to each other at their corners. A tetrahedron in an close-packed assembly of corner-sharing tetrahedra can occupy one of the three sites on the c-plane as A, B and C,

respectively (Figure 6 (b)). By rotating the tetrahedron by 180 ° around c-axis, we can get a twinned tetrahedron with twinned variants A', B' or C'. The SiC polytypes constitute various stacking permutations of the six types of tetrahedra A, B and C as well as A', B' and C'.

Corner sharing places certain restrictions on the stacking of two tetrahedra on top of one another [29]. Therefore, we are able to obtain the stacking rules in SiC as: A tetrahedron should be followed by another one of the same variant or twinned variant but with the preceding letter, e.g. ABCA and A'C'B'A', or AC', BA', CB', A'B, B'C and C'A. Based on the stacking rules in SiC, we can get the stacking sequences of all types of SiC polytypes. Figure 7 shows the stacking sequences of 6H- and 15R-SiC respectively.

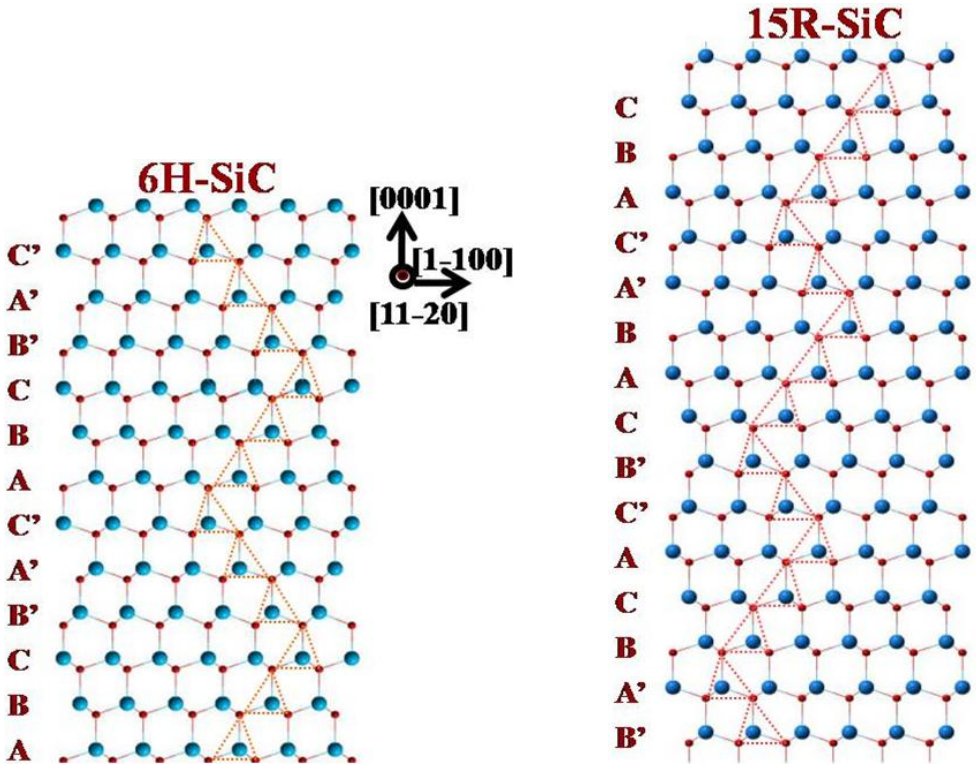

(a) (b)

Figure 7 (a) Stacking sequence of 6H-SiC Structure. Note the symmetric stacking of three untwinned tetrahedra followed by three twinned. (b) Stacking sequence of 15R-SiC Structure. Note the asymmetric stacking of three untwinned tetrahedra followed by two twinned.

Due to the variety of polytypes and the limitation of growth conditions control, it is fairly common to have polytype inclusions embedded in SiC crystals which may lead to nucleation of device-killer----micropipes [30].

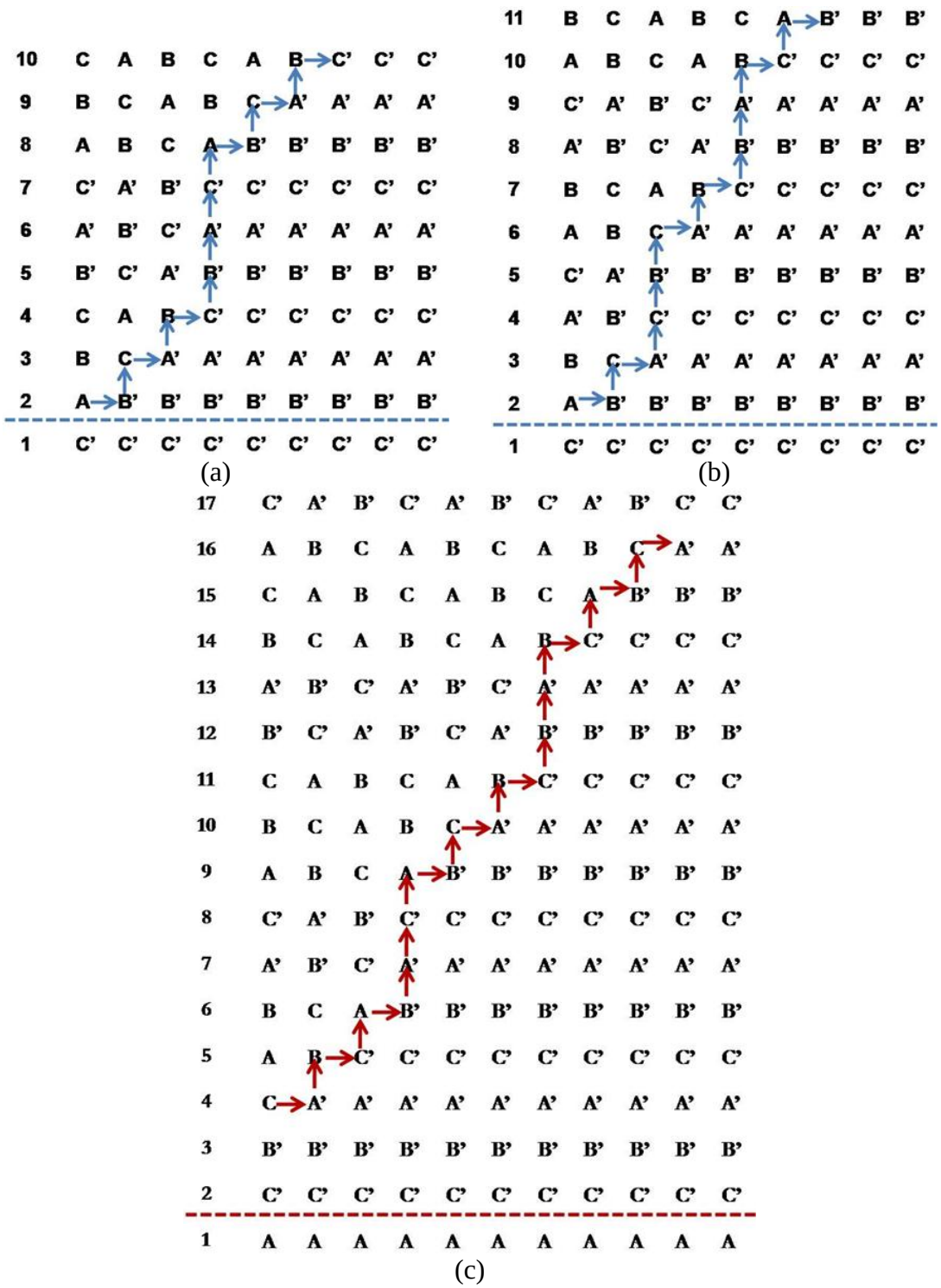

Figure 8 Schematic diagrams of mechanism of polytype transformation from 4H- (a), 6H- (b) and 15R-(c) to 3C-SiC according to Pirouz's theory.

Pirouz and Yang [31] proposed a dislocation model for polytype transformation in SiC. The model is based on the asymmetry in the mobility of partial dislocations in SiC. According to

the Frank-Read mechanism of dislocation multiplication, with one partial dislocation producing a fault as it moves and one partial dislocation almost immobile, a faulted loop is produced on the primary glide plane where the stacking sequence within the loop is changed. The dissociated screw dislocation cross-slips from the primary glide plane onto the next allowed slip plane according to stacking rules. On every faulted glide plane, the tetrahedra on it transform to a twinned variant. Then, the dissociated screw dislocation double-cross-slips back onto the next allowed primary glide plane due to the compressive stress between the partial dislocations. The repetition of glide by the leading partial dislocation followed by cross-slip of the screw dislocation thus leads to phase transformation in SiC. Based on this model, we are able to obtain the similar mechanism of polytype transformation from 4H-, 6H- and 15R- to 3C-SiC (Figure 8).

However, in this model, polytype transformation in SiC requires significant difference in the mobility of Si- and C-core basal plane partial dislocations which is only the case at much lower temperature than the growth temperature and the operation of classic two-ended Frank-Read source. In fact, X-ray topography studies have shown that close to the growth temperature, basal plane dislocations (BPDs) dissociated into partial dislocations which have similar mobility and move together in pairs. In addition, slip of dislocations in non-cubic polytypes of SiC is confined to basal plane [32] and there is no cross-slip. Regarding the operation of two-ended Frank Read sources, the general absence of cross-slip makes it difficult to isolate a segment of BPD pinned at two points. Threading edge dislocations (TEDs) can act as pinning points but they are ineffective at pinning moving BPDs. Threading screw dislocations (TSDs) can also pin BPDs but lock them in position which prevents Frank-Read source activation [33].

1.3. Motivation

As discussed above, for the growth of $B_{12}As_2$ on Si with (100), (110) and (111) orientation and c-plane (0001) 6H-SiC, rotational and translational variants were both predicted and observed. Degenerate epitaxy, manifested by the presence of high densities of twin boundaries, was observed in all of these cases. The detrimental influence of the results of degenerate epitaxy on $B_{12}As_2$ device performance has made its elimination a primary goal of the $B_{12}As_2$ crystal growth community. To avoid the presence of these variants which may largely degrade device performance and to provide guidance for the growth process, it is necessary to

study and understand the formation mechanisms of the defects in the $B_{12}As_2$ films and their adverse influence on the physical properties of $B_{12}As_2$, so as to produce high-quality $B_{12}As_2$ of single crystal nature. However, there is no detailed report so far on the defect structures of $B_{12}As_2$ grown on 4H-SiC and the correlation between defect structures and physical properties of $B_{12}As_2$ remains obscure. Twinning behavior can be diminished by surface roughness or vicinality since the presence of the risers and terraces that comprise the step structures exerts an influence on the nucleation of variants. It has been proposed that m-plane 15R-SiC is potentially a good substrate choice for the growth of untwined $B_{12}As_2$ epilayers [34]. However, due to the limited resource of pure 15R-SiC substrates, it is very important to discover other good substrates which are commercial-available. Therefore, the primary motivation for our research in this area is to investigate the defect structures, to explore growth mechanisms of $B_{12}As_2$ grown on various SiC substrates on an atomic scale and to seek another potentially suitable substrate, which may shed light on the development of strategies to minimize the densities of the defects so as to grow high quality single crystalline $B_{12}As_2$ films and reduce the adverse effects of the defects on device performance.

As discussed above, the model of polytype transformation in SiC by Pirouz cannot explain the nucleation of polytype inclusions during the growth process at a relatively high temperature. Therefore, we need a new model to better explain the nucleation mechanisms for polytype transformation in SiC during growth without the operation of classic two-ended Frank-Read source and cross-slip.

2. Theoretical background

2.1. Fundamentals of x-ray diffraction

X-ray topography is a well-known characterization technique based on both the kinematical and dynamical theories of diffraction of x-ray beams interacting with crystal lattices. When x-ray beams interact with very small crystals, kinematical theory is utilized to provide a good approximation. In kinematical theory, it is assumed that the x-ray beam will be scattered by the atoms in the crystal only one time and the loss of its intensity due to re-scattering is negligible. This theory is commonly used in the characterization of powder crystals or imperfect crystals and it is also suitable for perfect thin crystals in which multiple scattering can be ignored. Kinematical diffraction is an important theory in interpreting the contrast in the X-ray topographs.

In a perfect crystal, the x-ray beam is diffracted dynamically in which multiple scattering occured. Bloch waves are generated inside the crystals when the x-ray beam interacts with the periodic crystal lattice and the wave field inside the crystal is the sum of a series of plane waves [35].

According to the kinematical theory, the diffracted intensity of the x-ray beam is given by [36]:

$$I = F_{hkl}^2 \frac{\sin^2(\pi n_1 q_1)}{\sin^2(\pi q_1)} \cdot \frac{\sin^2(\pi n_2 q_2)}{\sin^2(\pi q_2)} \cdot \frac{\sin^2(\pi n_3 q_3)}{\sin^2(\pi q_3)} \quad (1)$$

where F_{hkl} is the structure factor, n_i (i = 1,2 or 3) is the number of unit cells along $\boldsymbol{a_i}$ direction ($\boldsymbol{a_1}$, $\boldsymbol{a_2}$, and $\boldsymbol{a_3}$ are unit vectors defining the unit cell) and q_i is the deviation component along $\boldsymbol{a_i}$. This equation provides a very good approximation for thin crystals. However, this equation cannot be used for thick crystals. Thus dynamical diffraction has to be analyzed for nearly perfect crystals. In the diffraction theory, a few concepts which help to interpret the contrast in x-ray diffraction topography are briefly introduced below: rocking curve width, the diffracted intensity and penetration depth.

2.1.1. Rocking curve width

The rocking curve width (FWHM) for perfect crystals is given by [37]:

$$2\delta_{hs} = \frac{2r_e\lambda^2}{\pi V \sin 2\theta_B}\frac{1}{\sqrt{|\gamma|}}|C|\sqrt{F_{hkl}F_{\bar{h}\bar{k}\bar{l}}} \quad \text{(Bragg case)} \tag{2}$$

and

$$2\delta_{os} = \frac{2r_e\lambda^2}{\pi V \sin 2\theta_B}\sqrt{|\gamma|}|C|\sqrt{F_{hkl}F_{\bar{h}\bar{k}\bar{l}}} \quad \text{(Laue case),} \tag{3}$$

where r_e is the classical electron radius, λ is the x-ray wavelength, V is the volume of the unit cell, θ_B is the Bragg angle, γ is the asymmetric ratio, C is the polarization factor and F_{hkl} is the structure factor.

The rocking curve width is very important in studying single crystal materials and it is able to directly reflect the quality of the crystal. The narrower the rocking curve, the higher the crystal quality. There are various causes of the broadening of the rocking curve such as dislocations, misorientation or residual strain. The rocking curve width is also very closely related to the extinction contrast, which is one of the most common contrast mechanisms in XRT. The reason is that the rocking curve width determines the volume of the kinematically diffracted region near the highly deformed region around the dislocation core which subsequently determines the width of the dislocation image. The different intensity from kinematically and dynamically diffracted regions will eventually lead to the dislocation images which appearing as darker contrast in the X-ray topographs. This type of contrast mechanism of dislocation image is referred to as "extinction contrast". An example can be found later in Chapter 5.

Huang et al developed a modeling process based on ray-tracing principle to simulate the x-ray topographic images of dislocations in SiC crystals [42]. This model has been successfully used in interpreting the topographic images of TSDs, TEDs and BPDs in various geometries. Large amount of observation indicates that orientation contrast is dominant over the extinction contrast in the x-ray topography of SiC in most cases.

2.1.2. Diffracted beam intensity

The intensity of the diffracted X-ray beam directly determines the intensity of the topographic images and it is an important parameter for us to select the appropriate diffraction vector for imaging the defects inside the crystals. The rocking curve width is also closely related to the magnitude of the structure factor, as we can see from Equations (2) and (3). Therefore, the structure factor is the most critical parameter in the X-ray topography studies. The larger the structure factor, the wider the rocking curve and the narrower the dislocation image we obtain. The structure factor F_{hkl} is defined as [38]:

$$F_{hkl} = \sum_i f_i \exp\{-2\pi \mathrm{i}(\mathrm{hu}+\mathrm{kv}+\mathrm{lw})\}, \quad (4)$$

where f_i is the atomic scattering factor, (*hkl*) are the miller indices of the reflection plane and (*uvw*) are the fractional coordinates of the atoms in the unit cell.

2.1.3. Penetration depth

Penetration depth is also very important to interpret the X-ray topographic images. It provides detailed information about the size of the crystal volume that imaged by X-ray beam and therefore is very helpful in the analysis of the defect configurations, especially in epitaxial materials. It can be applied to imperfect crystals and the photoelectric absorption based penetration depth *t* is given by

$$t = \frac{1}{\mu\left(\frac{1}{\sin\phi_0} + \frac{1}{\sin\phi_h}\right)}, \quad (5)$$

where μ is the absorption coefficient (cm^{-1}), Φ_0 is the incident angle and Φ_h is the exit angle.

2.2. Synchrotron x-ray diffraction topography

X-ray diffraction topography is a powerful technique to image defects in single crystals with low defect density ($<10^6/cm^2$). Synchrotron radiation source is especially suitable for x-ray diffraction topography because it has much higher energy and thus brightness, and lower

divergence of the x-ray beam compared to other sources. Therefore, with low divergence angle as well as long X-ray beam-specimen distance, especially high resolution can all be achieved using synchrotron radiation because of the small dimension of the X-ray source. The vertical divergence angle of synchrotron radiation is given approximately by m_0c^2/E, where m_0 is the electron rest mass, c is the velocity of light and E is the electron energy. This value is typically 10^{-4} rad. The topographic resolution (R_x) is determined by the source size in the incidence plane (S_x), beam-specimen distance (D) and the film-specimen distance (d) and it is given by [39]

$$R_x = d\, S_x / D. \quad (6)$$

The resolution of the X-ray source in Beamline X19C at National Synchrotron Light Source is ~0.4 μm and ~0.06 μm in Beamline XOR-33BM /UNI-CAT at Advanced Photon Source if D=10 cm is used (vertical reflection geometry).

2.3. Contrast on X-ray Topographs

The contrast on X-ray topographs comes from the complicated interactions between the x-ray beam and the lattice inside the crystals. There are two mechanisms in theory to interpret the contrast on X-ray topographs: orientation contrast and extinction contrast. According to Bowen and Tanner, orientation contrast occurs when a region inside the crystal is misoriented by an amount which is larger than the divergence of the beam [40]. It will appear as an undarkened patch on the topographs. The orientation contrast mechanism is often used to study the crystals containing twins and grain boundaries, which exhibit multiple domains that have different orientations separated by domain walls (twin boundaries, grain boundaries, domain boundaries) where the orientation suddenly changes. Orientation contrast can also be observed from crystals containing defects such as dislocations or precipitates. In the synchrotron white beam XRT, the misoriented regions can automatically select the appropriate wavelengths in the beam which satisfies the Bragg condition. The orientation contrast thus appears as either an undarkened patch due to the divergence of the diffracted x-ray beams, or a darkened patch due to the convergence of the diffracted x-ray beams.

Another type of contrast mechanism is extinction contrast. Inside the crystal, the lattice around the dislocation core has kinematical diffraction to the X-ray beam due to the strain field associated with the dislocation. This is because this region falls beyond the full width at half

peak of the rocking curve thus the re-scattering of X-ray beam is negligible. Under low absorption condition, the diffracted beam intensity from the regions close to the dislocation core is stronger than the one from the surrounding matrix regions and its intensity is proportional to the length of the path in kinematical diffracted region. Therefore, the diffracted beam intensity from the dislocation core is higher than that from the matrix, leading to the dark dislocation lines (kinematical diffraction) in a grey background (due to primary extinction from dynamical diffraction) on the X-ray topograph. This is usually the dislocation feathure we observe in transmission mode of X-ray topographs of SiC materials.

3. Investigation methods

In the present work, the combined use of Normaski optical microscopy, SWBXT, SEM, HRTEM, STEM, CaRine 4.0 crystal modeling software and CrystalMaker software has been employed for the characterization of defect structures in $B_{12}As_2$ films, the investigation of growth mechanisms on different substrates and the study of polytype transformation in SiC.

3.1. Normaski optical microscopy

Nomarski optical microscopy is a convenient method to observe unstained and transparent samples by offering differential interference contrast. Compared to traditional optical microscopy, it is based on the principle of interferometry to gain information about the optical density of the sample. The enhanced contrast gives the appearance of a three-dimensional physical relief corresponding to the variation of optical density of the sample, emphasizing lines and edges. In this work, Normarski optical microscopy is used to observe the defect features on the surfaces of the $B_{12}As_2$ epilayers grown on different SiC substrates and the 6H-SiC polytype inclusions inside the 15R-SiC boule.

3.2. SWBXT

With its high strain sensitivity, high intensity, suitable spatial resolution and broad spectral range, SWBXT has been a powerful non-destructive tool to macroscopically investigate the crystallographic orientations and defect structures of various crystals, such as SiC [41-44]. Basically, there are three types of SWBXT techniques, consisting of back reflection, transmission (including scanning mode) and grazing incidence geometries. In this work, one type of SWXBT, transmission mode including scanning transmission mode, are utilized to determine the film/substrate epitaxial relations, the overall quality and macrostructure for the studied samples. For transmission mode SWBXT, the X-ray detecting film is placed behind the sample at the same height to record the diffraction pattern as shown in Figure 9. The recorded diffraction patterns contain the information from both substrate and the epilayer. The surface of the epilayer

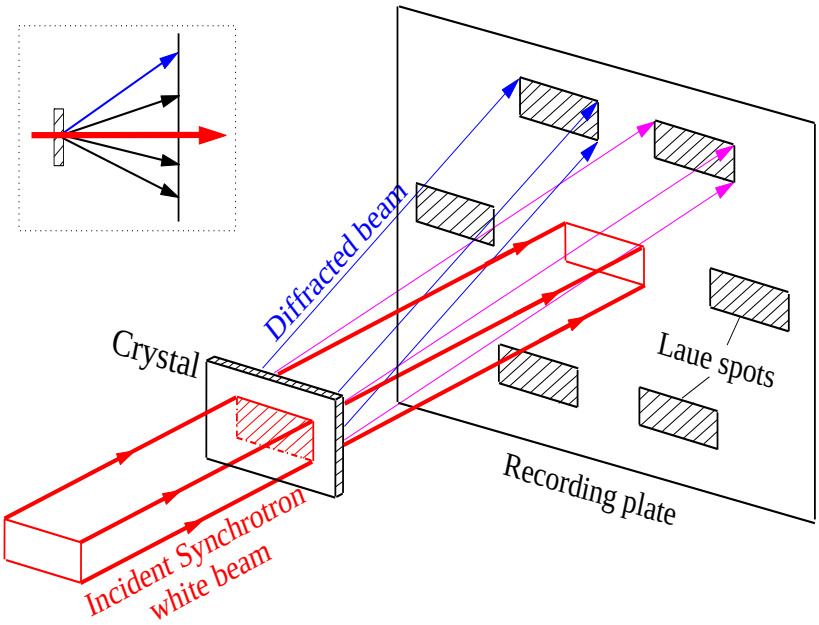

(a)

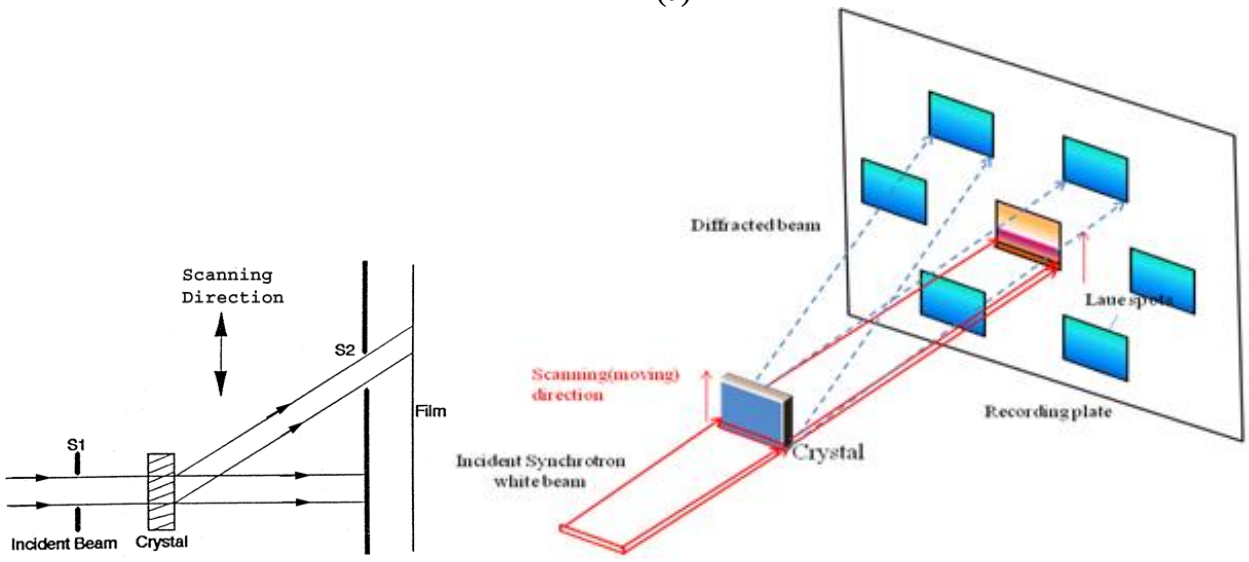

(b) (c)

Figure 9 Schematics of transmission SWBXT (a) and scanning transmission SWBXT (b) and (c).

is set to be the beam exiting surface so as to obtain as much information as possible from the films. To increase the intensity and contrast of $B_{12}As_2$ diffraction patterns and thus to better detect the crystallography information from $B_{12}As_2$ thin films, much longer beam exposure time varying from 30 seconds to 2 minutes is employed compared to normal exposure time which is 5 seconds. In order to determine the film/substrate epitaxial relationship, small beam size is utilized so as to avoid overlapping of diffraction spots and to better facilitate the indexing process. Global views of the quality and structure of the crystals can be obtained by recording

scanning transmission Laue patterns from the whole crystal volume. This was achieved by scanning the crystal and the film in the path of a slit-collimated beam.

3.3. SEM

Scanning electron microscopy (SEM) is a type of electron microscopy technique, which images the sample surface by scanning it with a high-energy beam of electrons in a raster scan pattern. It offers a wide range of depth of field and is widely employed to observe surface morphology of the samples. In this work, SEM is adopted to image the global surface morphologies and growth domain configurations of $B_{12}As_2$ films grown on different SiC substrates.

3.4. TEM

Transmission electron microscopy (TEM) is an important microscopy technique in which an electron beam with high voltage and current passes through and interacts with an ultra-thin specimen. An image is formed from the interaction of the electrons transmitted through the specimen; the image is magnified and focused by a series of electromagnetic lenses onto an imaging device, such as a fluorescent screen, on a layer of photographic film, or to be detected by a digital detector such as a CCD camera.

TEM is capable of imaging at a significantly higher resolution at the atomic level than optical microscopes, due to the small de Broglie wavelength of electrons. This enables the researchers to examine the fine details of the samples—even as small as a single column of atoms in the scale of angstrom. TEM forms a major analysis method in a range of scientific fields, in both physical and biological sciences. It has been widely used in material science as well as the fields of semiconductor materials, especially in terms of developing images of crystals to study their internal structures, interactions and defects.

Among various TEM techniques, high resolution TEM (HRTEM) has become a critical imaging tool to understand material properties by studying material structures at the level of atomic resolution. In this work, all of the HRTEM observation has been done along [10-1] zone axis (equivalent to [11-20] in hexagonal system), from which $B_{12}As_2$ twin boundaries are

expected to be well discerned according to the visualization obtained from CrystalMaker crystal visualization software. In contrast, [1-21] (equivalent to [1-100] in hexagonal system) is not selected to be a viewing direction for HRTEM in that the projections of the $B_{12}As_2$ twin domains along [1-100] zone axis of $B_{12}As_2$ are identical so that $B_{12}As_2$ twin boundaries won't be able to be recognized along this viewing direction. The comparison between the crystal visualization projected from [11-20] and [1-100] of $B_{12}As_2$ is shown in Figure 9 (a)-(d).

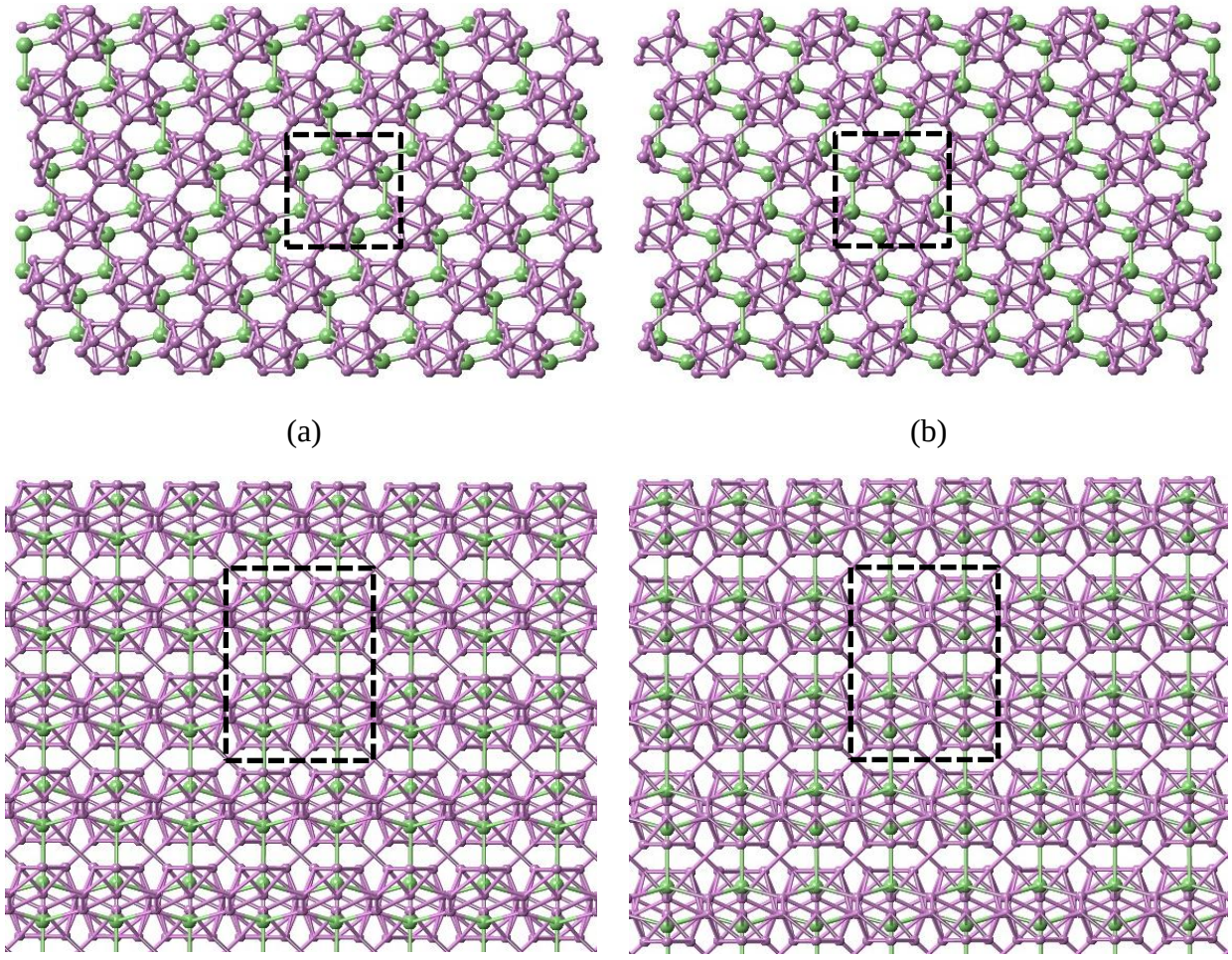

(a) (b)

(c) (d)

Figure 10 Projections of $B_{12}As_2$ atomic structure viewed along [11-20] (a) and its twinned orientation [-1-120] (b) as well as [1-100] (c) and its twinned orientation [-1100] (d).

3.5. STEM

Scanning transmission electron microscope (STEM) is another type of TEM. However, STEM is distinguished from conventional transmission electron microscopes by focusing the

electron beam into a narrow spot which is scanned over the electron transparent sample in a raster.

The rastering of the beam across the sample makes this type of microscope suitable for analysis techniques such as mapping by electron energy loss spectroscopy (EELS), annular dark-field imaging (ADF), high-angle annular dark-field imaging (HAADF) and energy dispersive X-ray (EDX) spectroscopy. These signals can be obtained simultaneously, allowing direct correlation of image and quantitative data.

By using a STEM and a high-angle detector, it is possible to form atomic resolution images where the contrast is directly related to the atomic number (z-contrast image). The directly interpretable z-contrast image makes STEM imaging with a high-angle detector appealing. This is in contrast to the conventional high resolution electron microscopy technique, which uses phase-contrast, and therefore produces results which need interpretation by simulation. In the investigation of $B_{12}As_2$ epilayers grown on SiC substrates, individual Si and As atoms can be distinguished under STEM which is a great advantage for understanding the atomic structure of the defects in the films and the nucleation mechansims by building the atomic models accordingly using CrystalMaker software. The excellent interfacial resolution of STEM has made it an ideal equipment to study the interface configurations in epitaxial materials.

3.6. CrystalMaker software and CaRine Crystallography software

CrystalMaker software is a powerful user-friendly software for crystal/molecular structures visualization and diffraction which has been developed over ten years and become more and more widely used for crystal visualizations in the fields of materials science, physics and life science. It provides the possibility to build any kind of crystal or molecular structure quickly and easily with built-in symmetry and automatic generation of all the bondings and polyhedra. Using CrystalMaker, one can manipulate and measure the crystal structure in real-time and generate versatile crystal models for detailed study of materials at the atomic level. In present work, the software is largely employed to generate crystal projections of $B_{12}As_2$ and SiC from various viewing directions, as exampled in Figure 10 (a)-(d).

CaRine is another crystallography software which has been developed since 1989. It provides multiple flexible ways to generate structural projections of various crystals.

3.7. TEM sample preparation

In this work, three methods are adopted for TEM sample preparation, which includes dimpling, wedge polishing and focused ion beam (FIB) milling. Figure 10 (a)-(f) shows the schematics of wedge and dimpling sample preparation for a TEM specimen. As shown in Figure 10 (a), the original sample wafer contains an epilayer (generally a few μm thick) grown on a substrate (a few hundred μm thick). Two small pieces (~1.5mm x 1mm) are cut from the wafer (Figure 10 (b)) and then stuck with each other by putting each epilayer face to face via a very thin layer of TEM glue. Thus a cross-sectional "sandwich" is formed as shown in Figure 10 (c). After mechanical polishing using a set of TEM T-tool or a semi-automatic polishing machine (Multiprep system) with a series of diamond lapping films, the front side of the sandwich is very smooth with ultra-fine polishing marks that are invisible even under optical microscope (Figure 10 (d)). Then the sample is flipped and further thinned via either back side mechanical polishing or dimpling technique until electron transparent (Figure 10 (e)). Finally the specimen is ion-milled with either the thinnest region at one edge or a hole in the center of the sandwich. The thinnest regions have thicknesses of less than 30nm and are highly electron transparent to be ideally used for HRTEM imaging (Figure 10 (f)).

TEM sample preparation by FIB milling technique is also used in this work. The FIB instrument is very useful for rapid site-specific preparation for cross-sectional TEM specimens. The small beam size and imaging capabilities of the FIB make this instrument ideal for preparing cross-sectional TEM specimens from $B_{12}As_2$ epilayer grown on SiC substrates for epitaxial studies and to locate the film/substrate interface. The beam can be very accurately positioned on the interested interface and defect regions of the sample at high current density to produce large uniformly thin TEM specimens that may be prepared in just a couple of hours. Figure 10 (g) shows the schematics of TEM sample preparation process by FIB technique. Note that in this procedure, preparing cross-sectional "sandwich" of the sample is not necessary. However, it requires a pre-thinning of both side of the specimen until the thickness of 30 μm.

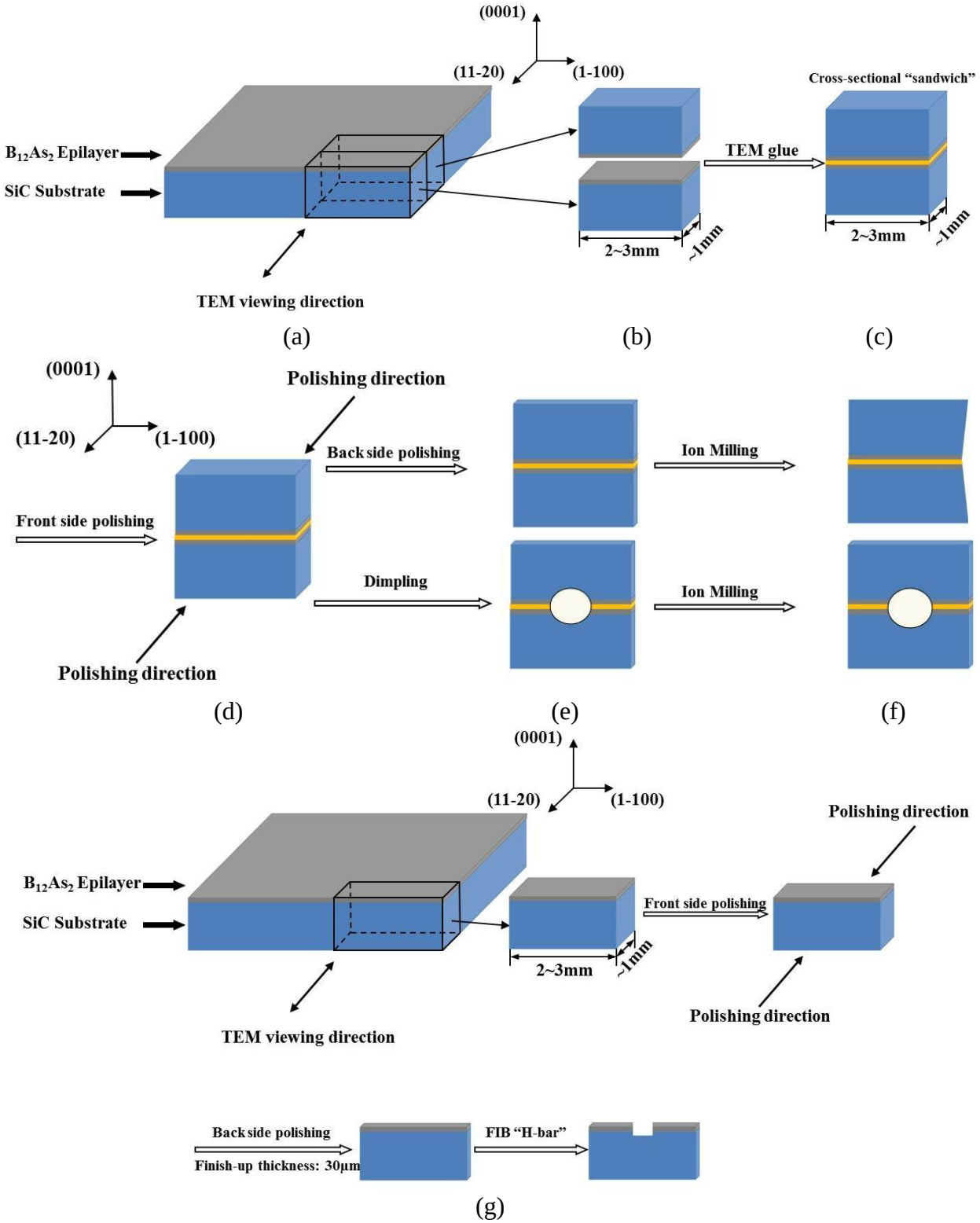

Figure 11 Schematics of TEM sample preparation procedures.

4. $B_{12}As_2$ grown on on-axis c-plane (0001)6H-SiC

4.1. Outline

The defect structure in $B_{12}As_2$ epitaxial layers grown at two different temperatures on (0001) 6H-SiC by chemical vapor deposition (CVD) was studied using SWBXT and HRTEM. The observed differences in microstructures were correlated with the differences in nucleation at the two growth temperatures. The effect of the difference in microstructure on macroscopic properties of the $B_{12}As_2$ was illustrated using the example of thermal conductivity which was measured using the 3-ω technique. The relationship between the measured thermal conductivity and observed microstructures is discussed.

4.2. Introduction

The absence of native substrates necessitates the heteroepitaxial growth of $B_{12}As_2$, typically on 6H-SiC substrates, often achieved using chemical vapor deposition. Epitaxial growth on (0001) 6H-SiC is facilitated by the fact that the in-plane lattice constants of 6H-SiC are close to one half of those of $B_{12}As_2$. Gaining a detailed understanding of its microstructure is essential on the pathway to device demonstration. In this work, we present studies of the influence of growth temperature on the microstructure of $B_{12}As_2$ thin films grown on (0001) 6H-SiC substrates. Implications of the microstructure on selected macroscopic physical properties are discussed.

4.3. Experimental

On axis, c-plane 6H-SiC wafers were used as substrates for the CVD growth of $B_{12}As_2$. The $B_{12}As_2$ films were synthesized by employing gaseous precursors of 1% B_2H_6 in H_2 and 2% AsH_3 in H_2. The c-plane $B_{12}As_2$ was deposited at 1275 ℃ and 1450 ℃, for samples, denoted here as S1 and S2, respectively, with 500 Torr of reactor pressure. Non-destructive SWBXT was carried out at the Stony Brook Topography station at the National Synchrotron Light Source, Brookhaven National Laboratory. Following this, cross-sectional TEM samples were prepared

parallel to (11-20) 6H-SiC. Conventional and high resolution TEM observation was performed using a JEOL 2100 transmission electron microscope with an electron accelerating voltage of 200KeV. To illustrate the implication of the microstructure on macroscopic physical properties of the film, the example of thermal conductivity was considered, measured using the 3-ω technique，which is extensively used to measure thermal conductivities of bulk and thin film dielectric materials [45, 46]. A ~100nm thick silicon oxide film was deposited onto the $B_{12}As_2$ film by plasma enhanced CVD to electrically isolate the sample. After this, photolithography was used to define a pattern of metal line heaters followed by the sputter deposition of the metal. An AC voltage of frequency ω was applied to the line heater, resulting in an increase in temperature. Because the resistivity of the metal depends on temperature, the voltage along the line heater also changes. The 3ω component in the resulting AC voltage was measured, which can be used to calculate the thermal conductivity.

4.4. Results and discussion

4.4.1. SWBXT results

Figure 12 (a) and (b) show the indexed diffraction patterns of sample S1 and S2 obtained via SWBXT in transmission using a $1mm^2$ area incident white beam. The diffraction spots labeled using the four index system correspond to the 6H-SiC substrate and exhibit six-fold symmetry as expected. For both samples, exposure times were increased in order to allow the weaker $B_{12}As_2$ diffraction spots to accumulate sufficient exposure to enable indexing. The diffraction spots from the $B_{12}As_2$ were generally more diffuse and appeared to form a 6-fold symmetric pattern rather than the 3-fold symmetric pattern expected for the rhombohedral crystal structure of $B_{12}As_2$. Detailed analysis confirms that this is because both films were twinned and, using the three index system, subscripts I and II are used to indicate matrix and twin diffraction spots. The size and shape of the matrix and twin diffraction spots indicate that the films appear to be fairly homogeneous solid solutions of matrix and twin.

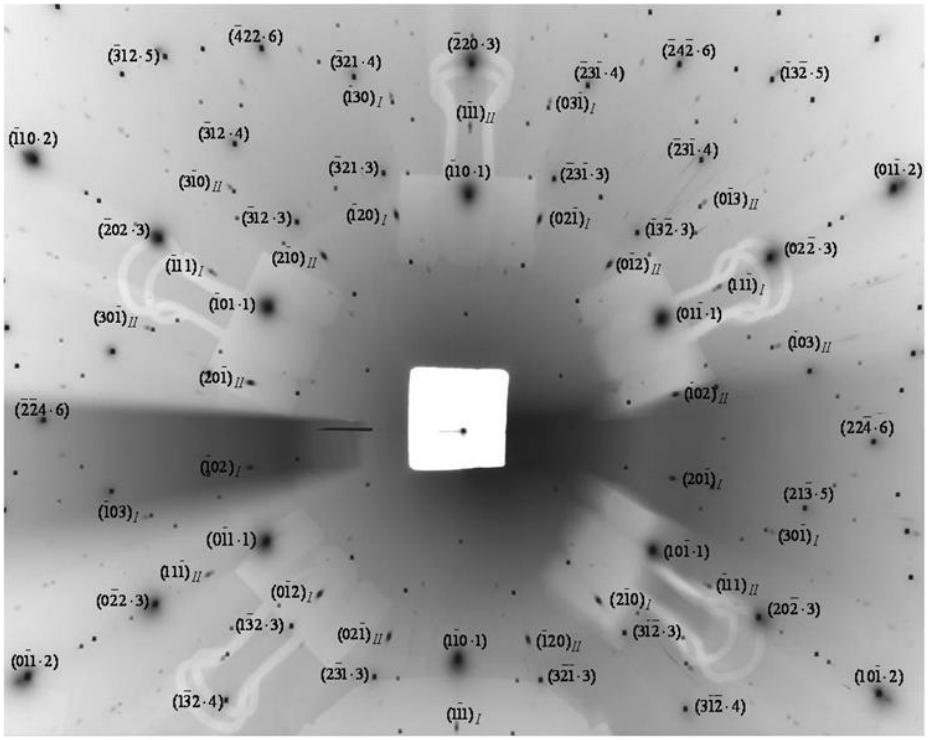

(a)

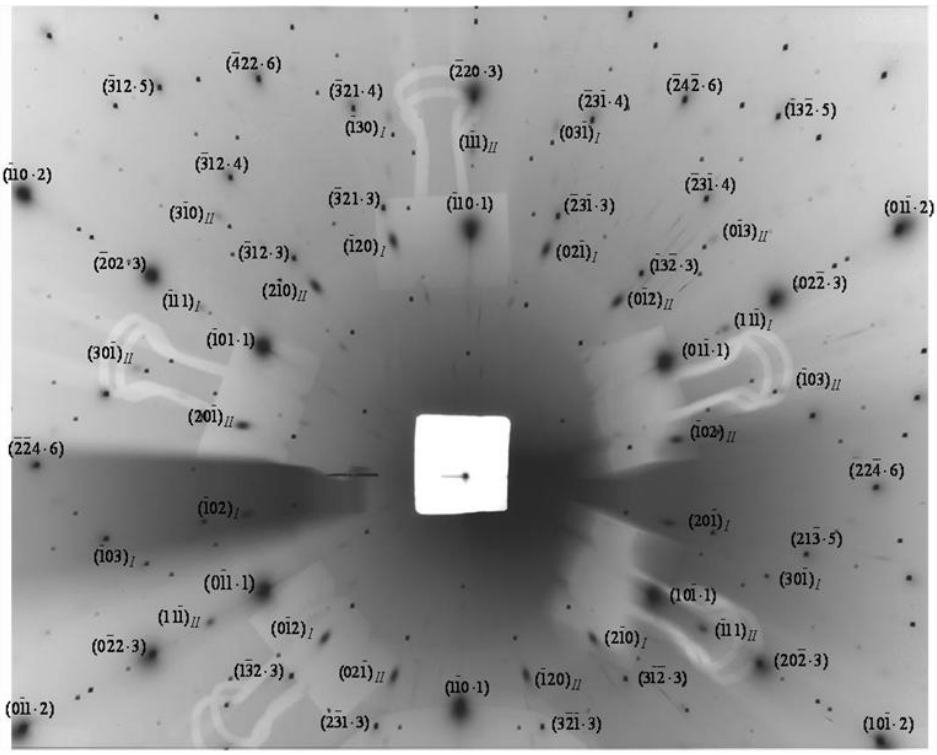

(b)

Figure 12 Indexed diffraction patterns of S1 and S2.

4.4.2. TEM results

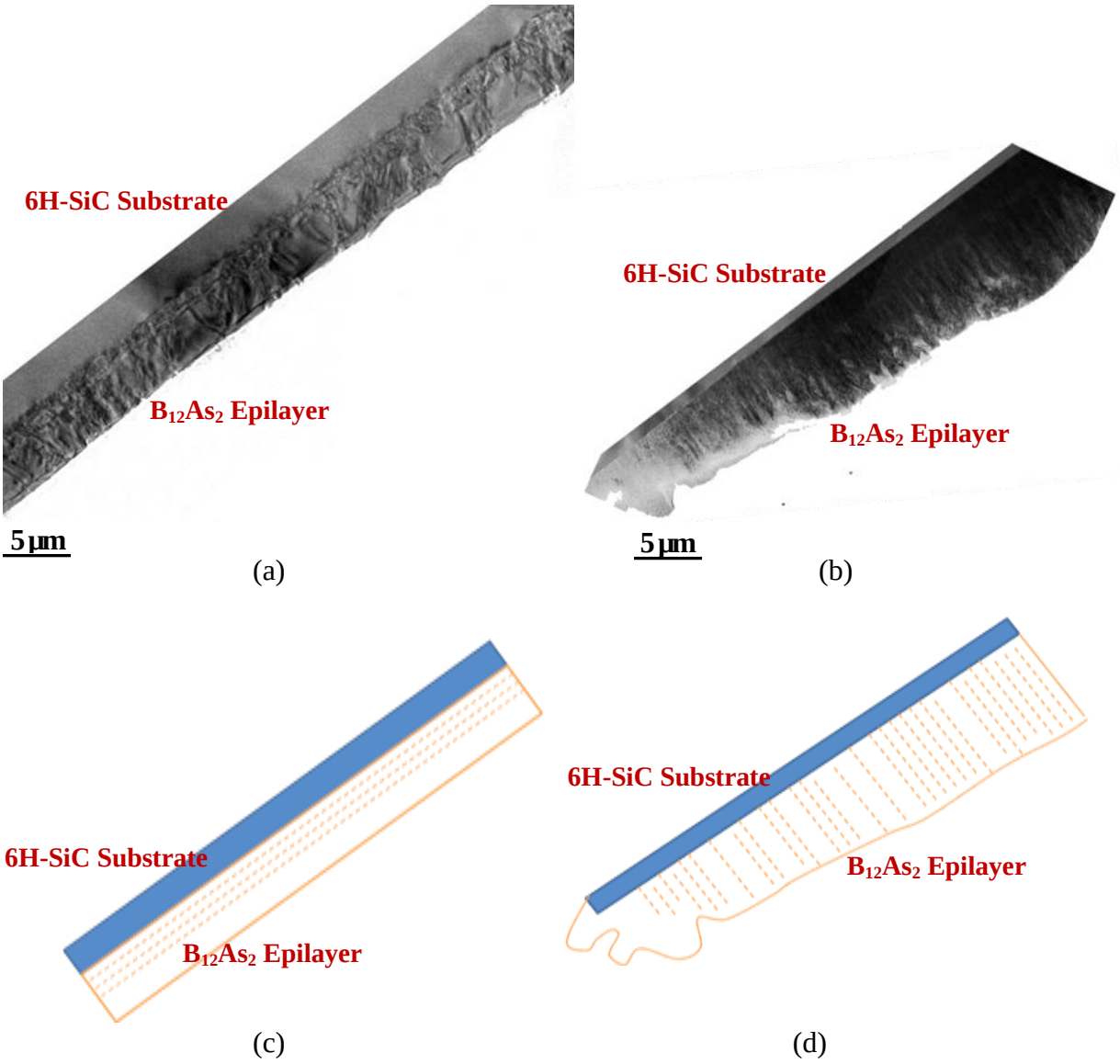

Figure 13 Low magnification TEM images of epilayers in S1 ((a)) and S2 ((b)). Note the boundaries between twinned domains approximately parallel to the interface in the interface region in (a) and penetrating the epilayer perpendicular to the interface in (b). Schematic diagram of epilyaers in S1((c)) and S2 ((d)). Dotted lines indicate twin boundaries.

The presence of rotational variants in the form of twins is expected in such degenerate epitaxy, as a lower symmetry film is epitaxially grown on a higher symmetry substrate, and the rotational variants are related by the symmetry element present in the substrate which is absent in the film. The details of the microstructure of the twin domains are, however, expected to vary

with growth temperature. In order to explore this variation in more detail, both samples were studied using TEM and conventional TEM. Images recorded from the samples are shown in Figures 13-15. In sample S1, sets of long, parallel (111) twin boundaries are confined to a region ~200nm thick comprising the volume from the substrate/epilayer interface to about one half of the thickness of the epilayer. The average thickness of the twin domains separated by the neighboring twin boundaries is around 60nm (see schematic diagram of the microstructure in Figure 13(c)). In sample S2, twin boundaries (lateral in this case) are mostly perpendicular to the epilayer interface, and the average distance between neighboring lateral twin boundaries (width of one domain) is around 140nm. (See schematic diagram of the microstructure in Figure 13(d))

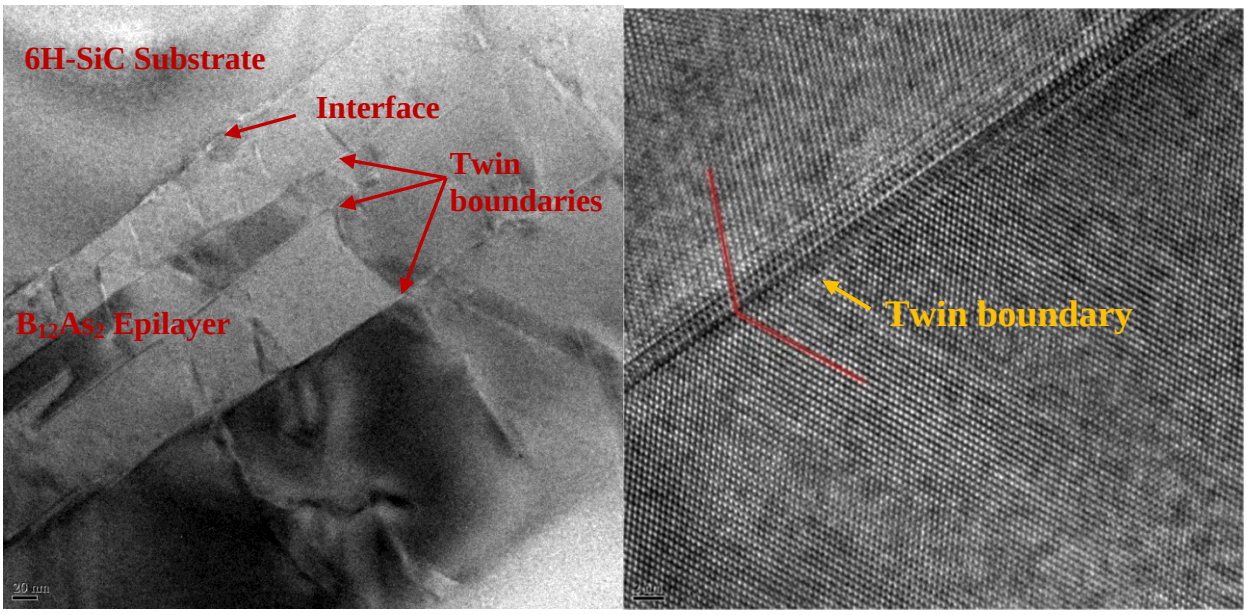

(a) (b)

Figure 14 Enlarged TEM image of the twin boundaries parallel to the interface in sample S1 ((a) and HRTEM image of one of the (111) boundaries ((b)).

Enlarged HRTEM images recorded from samples S1 and S2 are shown in Figures 14 and 15, respectively. Figure 14 shows a (111) twin boundary separating two twinned domains. This and other such boundaries have slightly increased complexity in their images since not only are they stepped parallel to the interface on these images but also into the plane of the page. Figure 15 shows a fairly complex microstructure comprising an almost columnar domain configuration suggesting that it may originate due to multiple nucleations. Note that the interface in both samples exhibits steps of opposite sign as expected for these "on-axis" substrates.

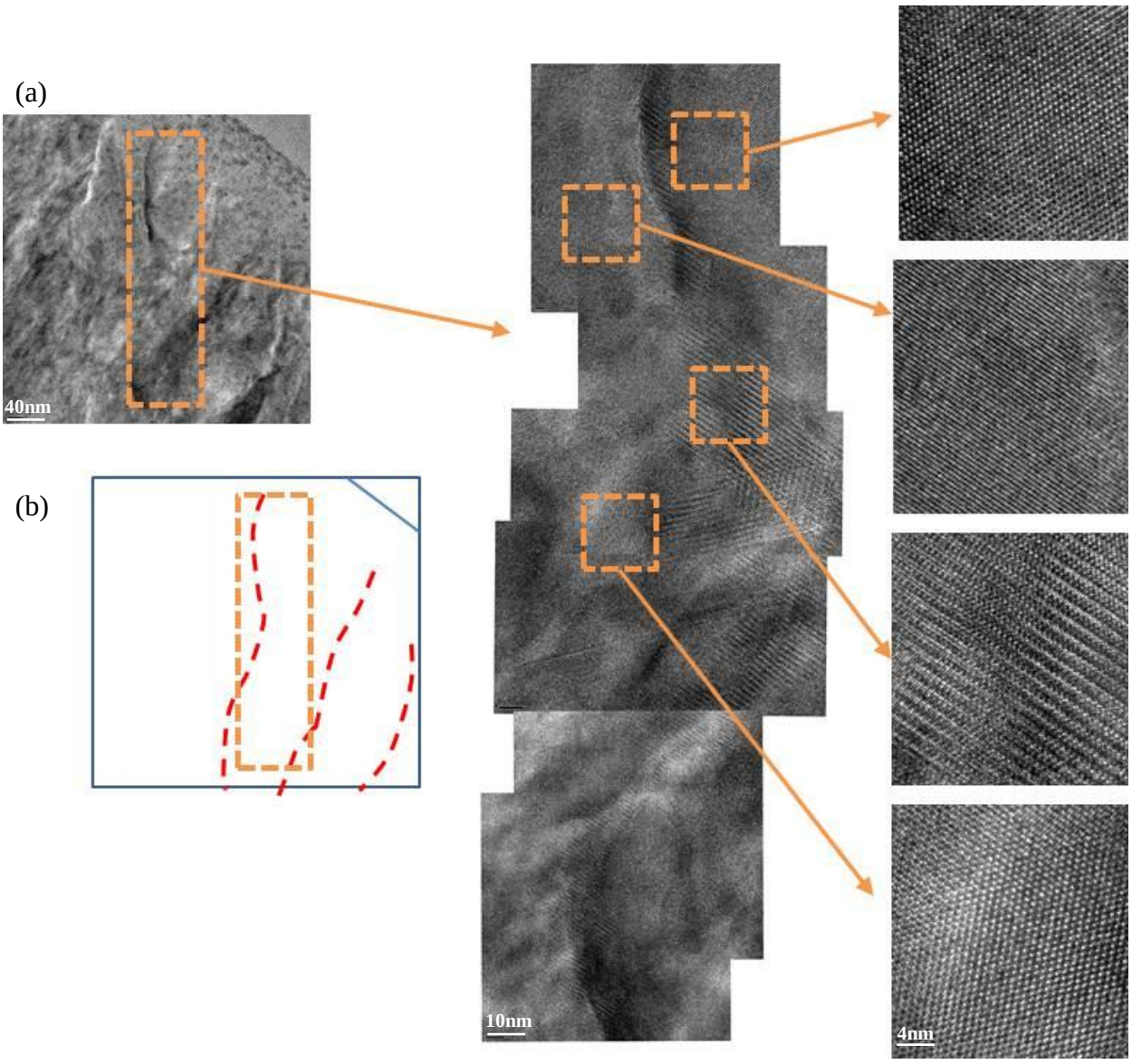

Figure 15 Enlarged TEM image of the lateral twin boundaries in sample S2 ((a) and (c)) and schematic diagram ((b)). HRTEM images of the indicated regions both matrix and twin domains ((d)).

Some understanding of the origin of these quite different microstructures can be obtained by consideration of the different nucleation under the two sets of growth conditions. Most growth parameters are similar except for the growth temperature which is 1275 °C for S1 and 1450 °C for S2. One might intuitively expect that the lower growth temperature would create a higher super saturation and thus a higher nucleation rate. However, contrary to expectation, the sample which appears to exhibit a microstructure resulting from multiple nucleation effects is

sample S2 which was grown at the higher temperature. Insight into this can be provided by consideration of the species likely involved in the CVD growth. For the 1% B_2H_6 and 2% AsH_3 in H_2 precursors utilized one might expect gas phase reaction at the growth temperature to involve species such as icosahedral $B_{12}H_{12}$ reacting with arsine to form small subsets of the $B_{12}As_2$ unit cell [34]. Given the relatively large size of these resultant species, it seems reasonable to assume that their surface diffusion will be complex and that they might be subject to the "lock-and-key" effect valid for the surface diffusion of large organic molecules on metal substrates [47]. For such systems only those molecules adsorbed onto the surface that are not oriented correctly to form bonds to the surface have the opportunity to become mobile and diffuse. If they are oriented and positioned to form bonds (multiple bonds) they are locked onto the surface and become immobile. Thus, in such systems, surface diffusion is a greater barrier to the nucleation process than thermodynamics. For the growth of $B_{12}As_2$ epilayers grown on on-axis (0001) 6H-SiC substrates, species can bond to the substrate in either "matrix" or "twin" orientation [19] and species are most effectively "locked-in" if they are able to bond simultaneously to a terrace and a step riser [19, 34].

For sample #S1, the lower growth temperature of 1275 ℃ leads to higher super-saturation but also more difficult surface diffusion compounded by the large size of the species. Thus, it is expected that more species will drop onto the surface but once there they will not undergo much surface diffusion. Only those that happen to drop in the right orientation close to a step riser will be locked in by bonding to both terrace and riser with all other being expected to desorb (Figure 16 (a)). Those that lock in will develop into nuclei and expand sideways until they impinge upon adjacent nuclei which may be in matrix or twin orientation (Figure 16 (b)). Since, the probability of such fortuitous adsorption is relatively low, this will lead to just a few nuclei being formed which will then coalesce and over grow each other to form a relatively small number of domains separated by twin boundaries roughly parallel to the interface consistent with the microstructure observed in sample S1 (Figure 16 (c)).

For sample #S2, the higher growth temperature of 1450 ℃ leads to lower super-saturation but easier surface diffusion which means that while fewer species will drop onto the surface but those that do are able to experience more surface diffusion. Some species, as at the lower temperature, may by chance be correctly positioned and oriented to immediately bond to terrace and riser while the majority will have the chance to diffuse around until they find a step, get

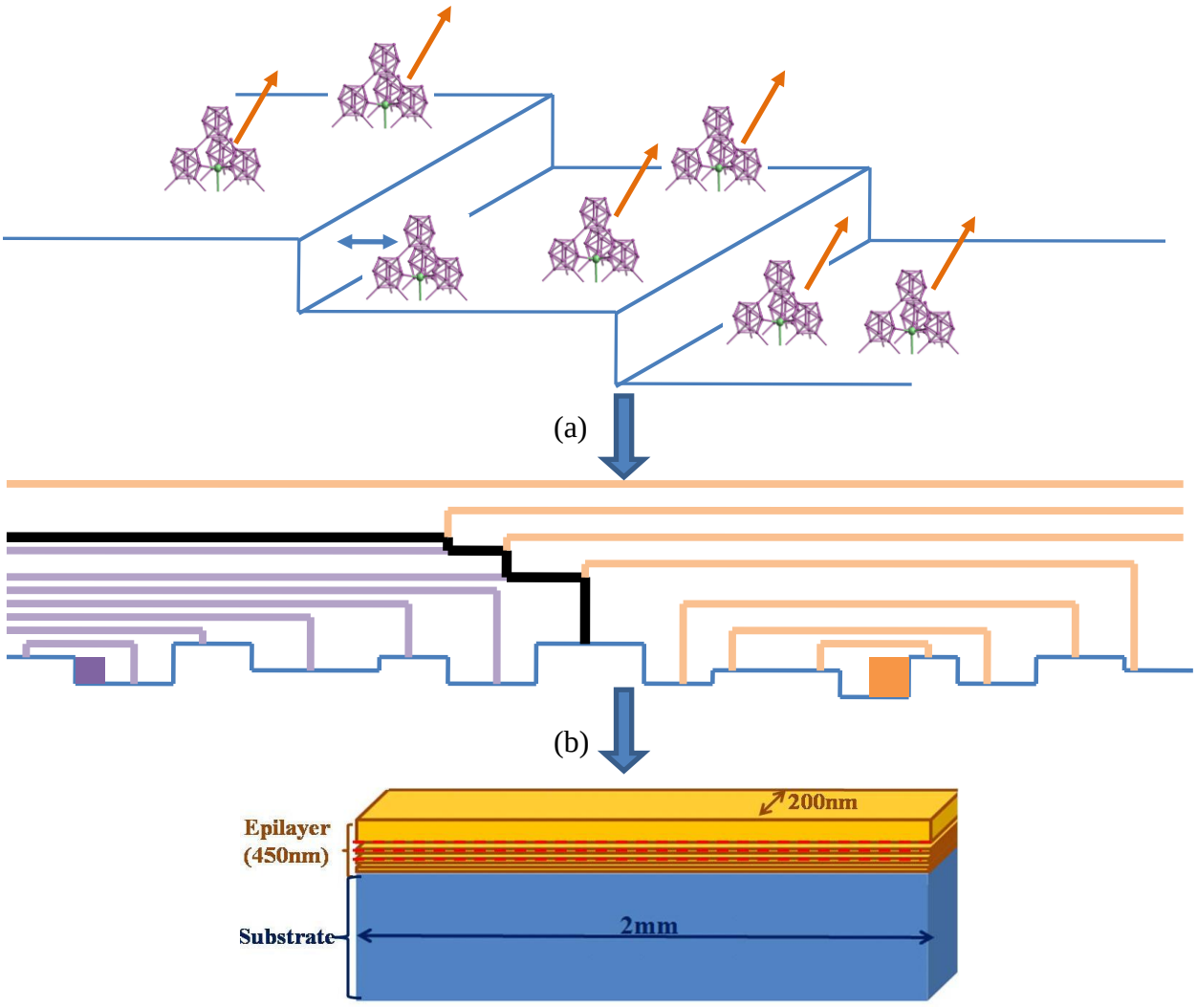

Figure 16 Schematic diagrams of nucleation process (a), coalescence of nuclei (b) and the final structure of twin boundaries on the SiC substrate surface in sample S1.

locked in and form a nucleus (still others who don't find a step will desorb) (Figure 17 (a)). Therefore, in this case, in contrast to the lower temperature case, it is more likely that we will have multiple nucleation and smaller domains leading to a larger number of nuclei which impinge upon each other at an earlier stage of growth which will be separated by many complex twin domain walls roughly perpendicular to the interface (Figure 17 (b)). This is consistent with the microstructure observed in sample S2 (Figure 17 (c)).

To illustrate the implication microstructures have on macroscopic physical properties of the $B_{12}As_2$, preliminary measurements of the thermal conductivity of the $B_{12}As_2$ along the $[111]_{B12As2}$ direction, i.e., perpendicular to the film surface, were performed using the 3-ω

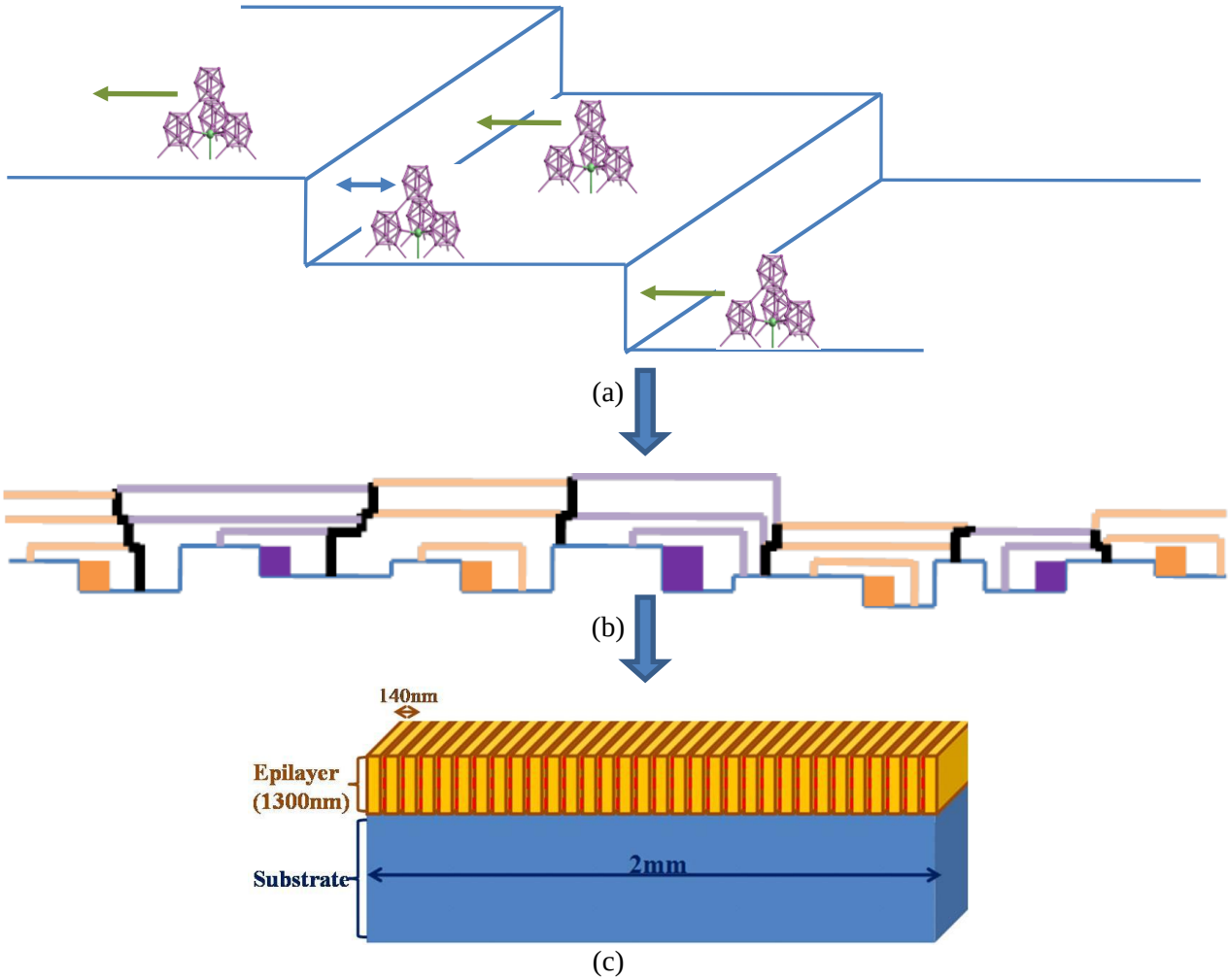

Figure 17 Schematic diagrams of nucleation process (a), coalescence of nuclei (b) and the final structure of twin boundaries on the SiC substrate surface in sample S2.

technique. To measure thermal conductivity of thin film, one-dimension heat conduction model and semi-infinite substrate are assumed. Qualitatively, it has been estimated that the errors related to these two factors are within 1% when the thermal penetration depth is at least 5 times greater than the width of the line heater and smaller than one-fifth of the sample thickness. Both conditions are fully satisfied in the frequency range used in our experiments [48]. We determined at room temperature a thermal conductivity of 0.148 $Wcm^{-1}K^{-1}$ for sample S1 and 0.256 $Wcm^{-1}K^{-1}$ for sample S2. This difference is in part due to the difference in microstructure for both samples, with S1 having a larger density of grain boundaries/domain walls than S2 parallel to the sample surface. Thermal conductivity is affected by phonon scattering occurring at these twin or grain boundaries and will diminish thermal conductivity more for sample S1 than S2. One of the

potential applications of $B_{12}As_2$ is for thermo electrics. The conversion efficiency from heat to electricity depends on the figure-of-merit, which is inverse proportional to thermal conductivity, and proportional to product of the square of thermal power and electrical conductivity. For this purpose, we want material with low thermal conductivity. The HRTEM results help to understand how to manipulate the thermal conductivity by varying growth condition. People have been working on develop complex material with low thermal conductivity and high thermal power. Further contributions to difference in thermal conductivity may arise from differences in the impurity concentration.

4.5. Conclusions

The defect structures in $B_{12}As_2$ epitaxial layers grown at two different temperatures on (0001) 6H-SiC by chemical vapor deposition (CVD) was studied using synchrotron white beam x-ray topography (SWBXT) and high resolution transmission electron microscopy (HRTEM). Differences in the observed microstructures were correlated with difference in nucleation at different growth temperature arising from the “lock-and-key” effect. We show that macroscopic physical properties of the $B_{12}As_2$ are affected by the microstructure, as illustrated by the example of thermal conductivity.

5. Nucleation Mechanism of 6H-SiC Polytype Inclusions inside 15R-SiC Crystals

5.1. Outline

A model is presented for the nucleation mechanism of 6H-SiC polytype inclusions inside 15R-SiC boules. Inhomogeneous densities of screw dislocations lead to uneven growth rates resulting in complex step overgrowth processes which can partially suppress the Burgers vector of a 15R 1c screw dislocation through the creation of Frank faults and Frank partial dislocations. Combined with stacking shifts induced by the passage of basal plane partial dislocations it is shown that the partial Burgers vector suppression can leave behind a residual 6H 1c dislocation which then acts as a nucleus for reproduction of 6H-SiC structure in 15R-SiC crystal.

5.2. Introduction

Silicon carbide possesses outstanding properties such as high breakdown field, wide band-gap, high thermal conductivity, good chemical and mechanical stability and high saturated electron drift velocity that constitute such a significant improvement over conventional semiconductor materials that many applications are envisaged. However, while some applications have already been realized, issues relating to crystalline defects and polytype inclusions remain a barrier to the successful realization of several others.

SiC is noted for its large number of polytypes. Up to now, more than 200 types of phases of SiC have been found. Due to the variety of polytypes and the limitation of growth conditions control, it is fairly common to have polytype inclusions embedded in SiC crystals which may lead to nucleation of device-killer----micropipes. Consequently, the nucleation mechanism of polytype inclusions in SiC crystals assumes great importance. The goals of our study in this paper are to understand nucleation mechanisms of 6H-SiC polytype inclusions inside 15R-SiC crystals, so as to design strategies to mitigate their negative effects on SiC devices by completely eliminating them.

First, it is necessary to understand the stacking rules in SiC. The structure of SiC can be considered as an assembly of corner-sharing tetrahedra. Every SiC tetrahedron arises from the

tetrahedral bonding between silicon and carbon atoms and the SiC tetrahedra are joined to each other at their corners. A tetrahedron in an close-packed assembly of corner-sharing tetrahedra can occupy one of the three sites on the c-plane as A, B and C, respectively. By rotating the tetrahedron by 180 °around c-axis, we can get a twinned tetrahedron with twinned variants A', B' or C'. The SiC polytypes constitute various stacking permutations of the six types of tetrahedra A, B and C as well as A', B' and C'.

Corner sharing places certain restrictions on the stacking of two tetrahedra on top of one another. Therefore, we are able to obtain the stacking rules in SiC as: A tetrahedron should be followed by another one of the same variant or twinned variant but with the preceding letter, e.g. ABCA and A'C'B'A', or AC', BA', CB', A'B, B'C and C'A. Based on the stacking rules in SiC, we can get the stacking sequences of all types of SiC polytypes.

Pirouz and Yang proposed a dislocation model for polytype transformation in SiC. The model is based on the asymmetry in the mobility of partial dislocations in SiC. According to the Frank-Read mechanism of dislocation multiplication, with one partial dislocation producing a fault as it moves and one partial dislocation almost immobile, a faulted loop is produced on the primary glide plane where the stacking sequence within the loop is changed. The dissociated screw dislocation cross-slips from the primary glide plane onto the next allowed slip plane according to stacking rules. On every faulted glide plane, the tetrahedra on it transform to a twinned variant. Then, the dissociated screw dislocation double-cross-slips back onto the next allowed primary glide plane due to the compressive stress between the partial dislocations. The repetition of glide by the leading partial dislocation followed by cross-slip of the screw dislocation thus leads to phase transformation in SiC. Based on this model, we are able to obtain the similar mechanism of polytype transformation from 4H-, 6H- and 15R- to 3C-SiC.

However, in this model, polytype transformation in SiC requires significant difference in the mobility of Si- and C-core basal plane partial dislocations which is only the case at much lower temperature than the growth temperature and the operation of classic two-ended Frank-Read source. In fact, X-ray topography studies have shown that close to the growth temperature, basal plane dislocations (BPDs) dissociated into partial dislocations which have similar mobility and move together in pairs. In addition, slip of dislocations in non-cubic polytypes of SiC is confined to basal plane and there is no cross-slip. Regarding the operation of two-ended Frank Read sources, the general absence of cross-slip makes it difficult to isolate a segment of BPD

pinned at two points. Threading edge dislocations (TEDs) can act as pinning points but they are ineffective at pinning moving BPDs. Threading screw dislocations (TSDs) can also pin BPDs but lock them in position which prevents Frank-Read source activation. In this case, we need a new model to explain the nucleation mechanism for polytype transformation in SiC.

5.3. Experimental

On axis, a-plane 15R-SiC crystals with 6H-SiC polytype inclusions were studied using non-destructive Synchrotron White Beam X-ray Topography (SWBXT) at the Stony Brook Topography station at the National Synchrotron Light Source, Brookhaven National Laboratory and monochromatic XRT at APS, Argon National Laboratory. Global views of the quality and structure of the crystals were initially obtained by recording transmission Laue patterns from the whole crystal volume. This was achieved by scanning the crystal and the film in the path of a slit-collimated beam. This enabled the polytype distribution to be determined as well as the distribution of defects and overall crystal quality. Based on the results of these global studies, areas of interest were identified which were then investigated in detail in various diffraction geometries. Following this, in-plane Transmission Electron Microscope (TEM) specimens from the transition regions between 15R- and 6H-SiC were prepared parallel to (11-20)15R-SiC. High resolution TEM observation was performed using a JEOL 2100 transmission electron microscope with an electron accelerating voltage of 200KeV.

5.4. Results and discussion

5.4.1. Optical Microscopy, SWBXT and monochromatic XRT results

Figure 18 shows the representative optical image of 15R-SiC sample with visible 6H-SiC inclusion embedded in the top-right region which appears as darker green color compared to the rest of the sample which is 15R polytype. Global studies carried out for both crystals using scanning transmission SWBXT confirmed that, for each case, most of the crystal volume was 15R polytype (see Figures 19). This is evident from the large area diffraction spots on, for example, Figure 19(a) which can be indexed using the 15R structure. Examples of the larger 15R

diffraction spots are indicated by A, B, C and D. However, in addition, both samples contained small lenticular inclusions of 6H-SiC. In Figure 19 (a), diffraction spots corresponding to the 6H inclusion can be found at, for example, a, b, c, and d. Similar lettering is used on Figure 19(b) to indicate the diffraction spots corresponding main 15R regions and the 6H inclusions.

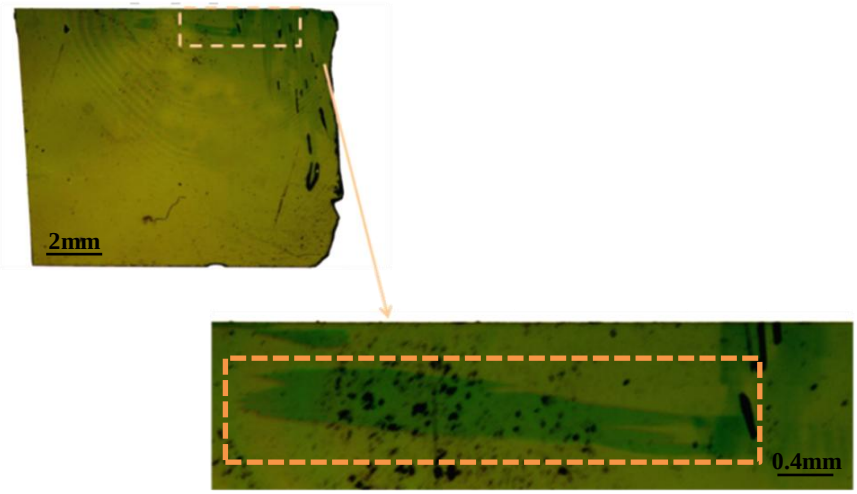

Figure 18 Optical images showing the existence of 6H-SiC polytype inclusion inside 15R-SiC sample.

The detailed strategy for further study was then dictated by the results of these global studies. First, based on the observation that the crystals comprised large volumes of 15R, Laue patterns were recorded using a small-area beam from one of the uniform 15R regions in each crystal in order to confirm their orientations. Comparison of experimental and simulated X-ray Laue patterns shows that both samples were of a-plane surface orientation. Second, detailed topographic studies were carried out in various diffraction geometries to elucidate the details of the microstructure in the crystals, with particular emphasis on those regions shown to be most interesting from the global studies.

Based on the information provided by the global studies, detailed diffraction patterns were recorded from the 6H polytype and surrounding region of the samples using a slit-collimated incident beam.

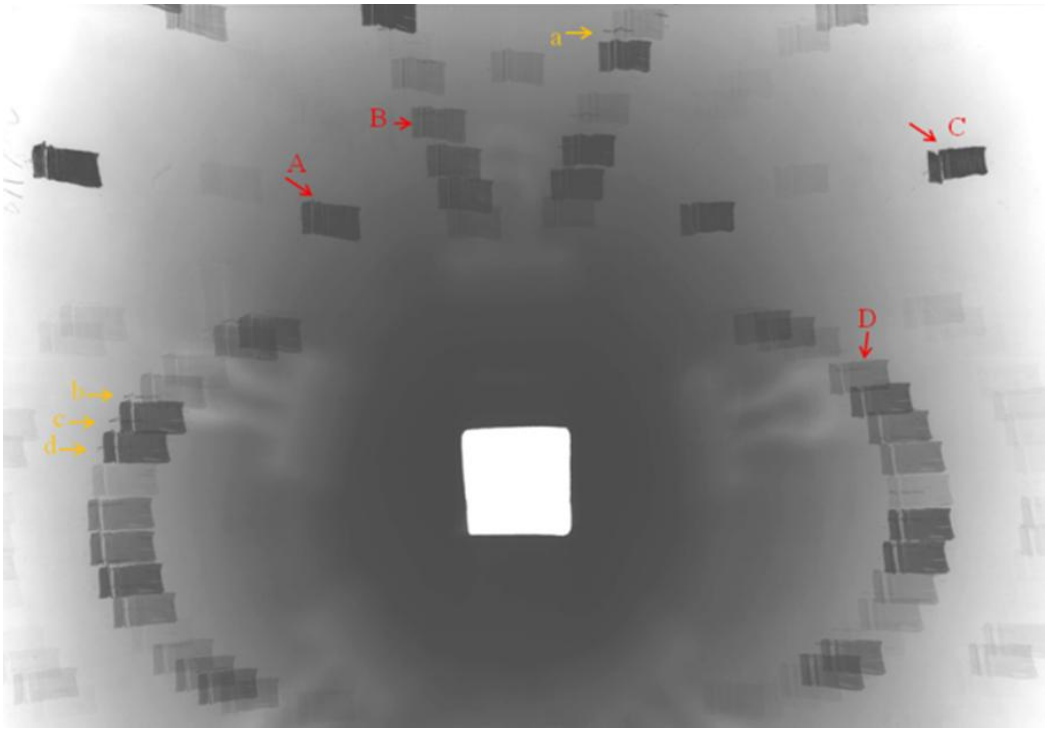

(a)

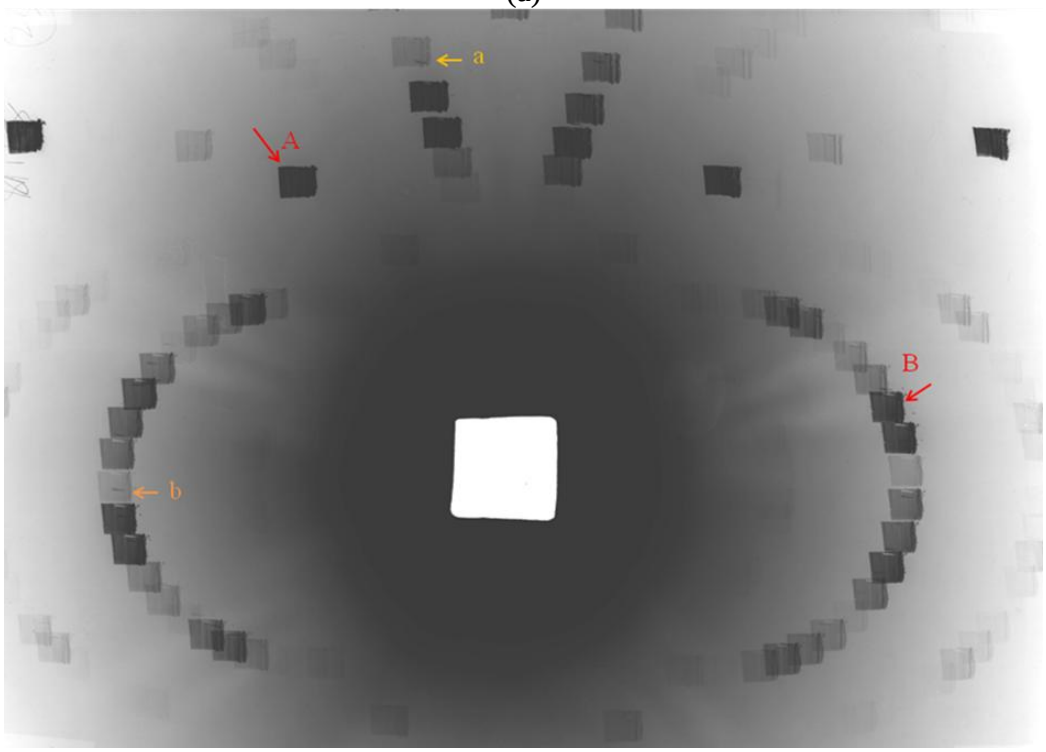

(b)

Figure 19 Scanning transmission SWBXT results of 15R-SiC samples with 6H-SiC inclusions. Diffraction patterns from both 6H and 15R-SiC are distinguishable as the large area diffraction spots indicating by red capital letters can be indexed using the 15R structure and diffraction spots indicated by orange lowercase letters correspond to 6H structure.

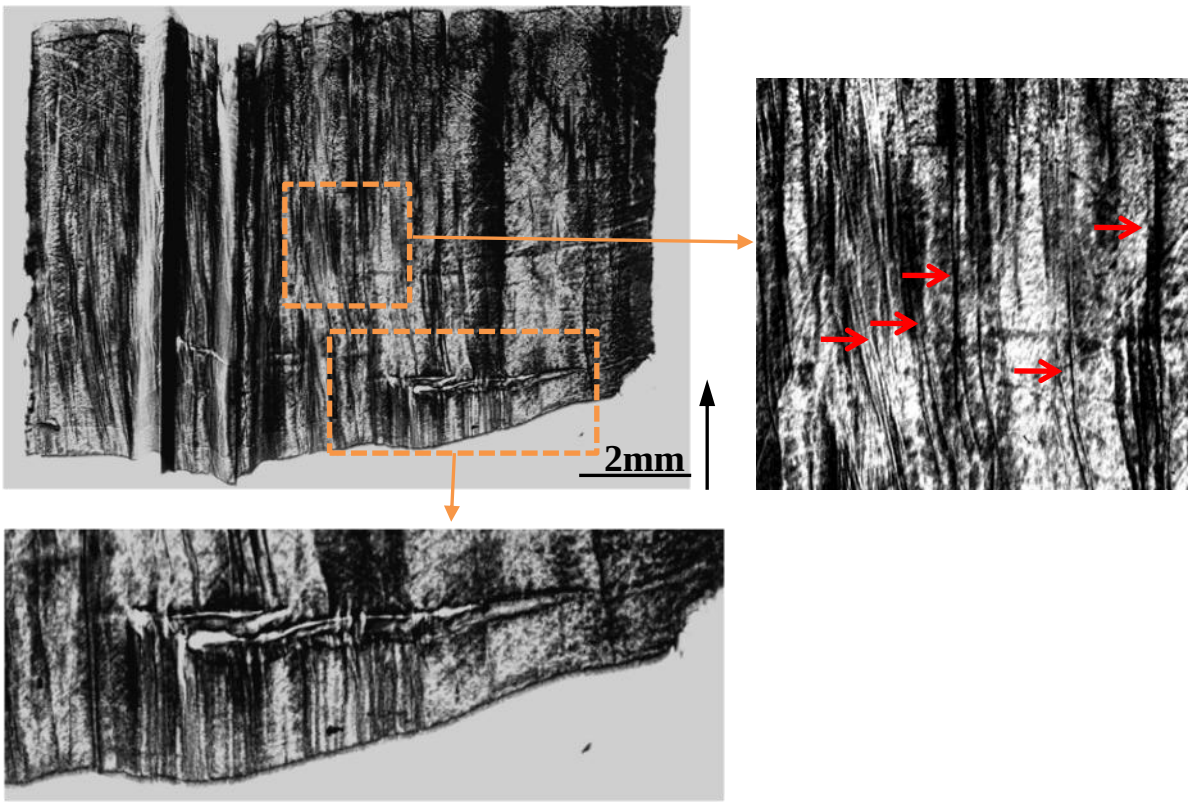

(a)

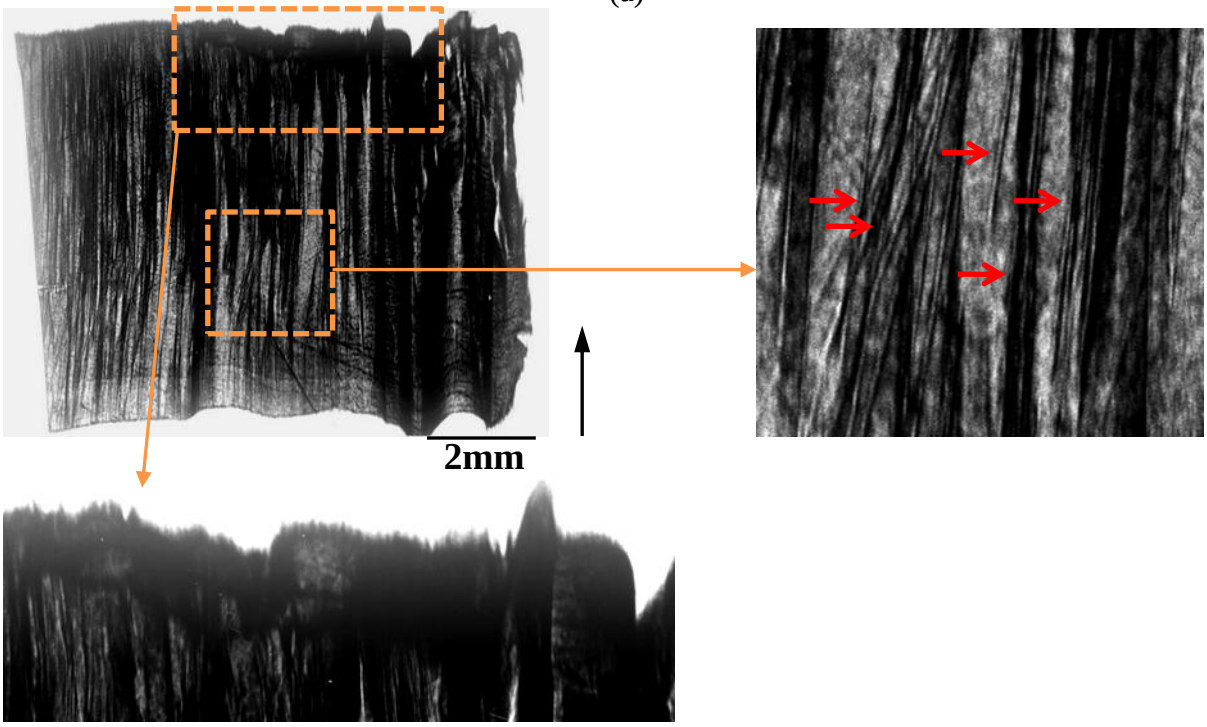

(b)

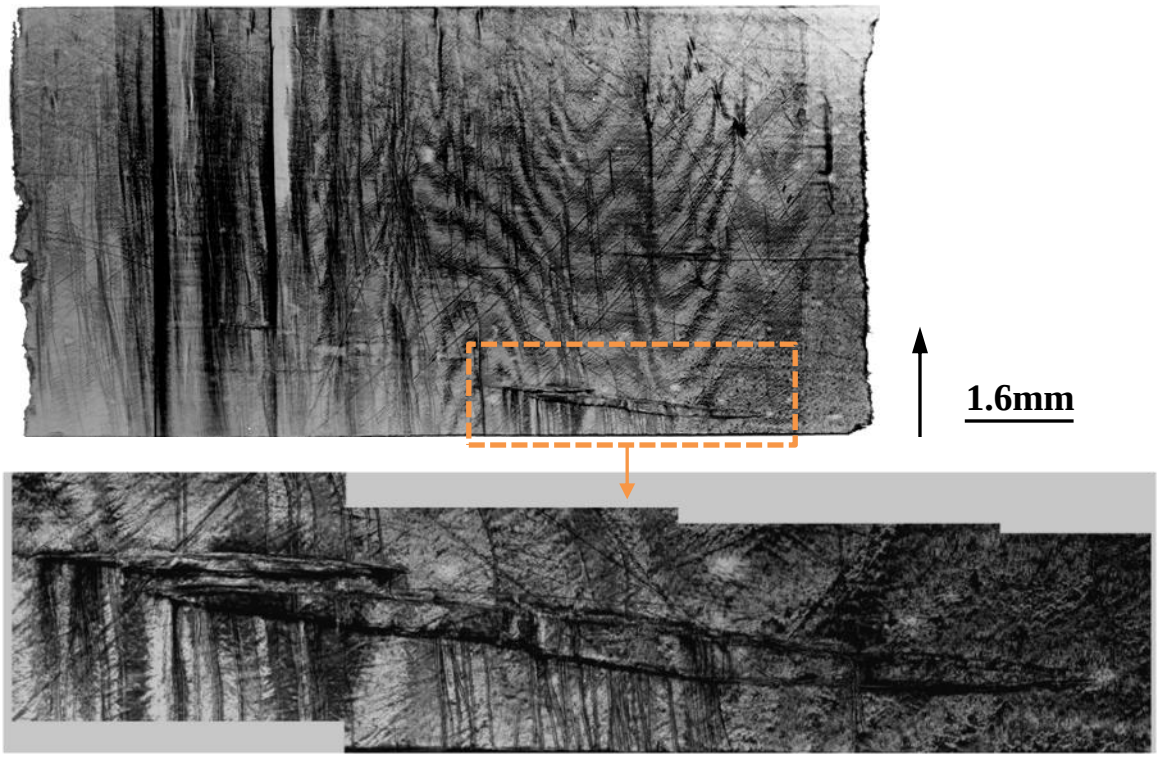

(c)

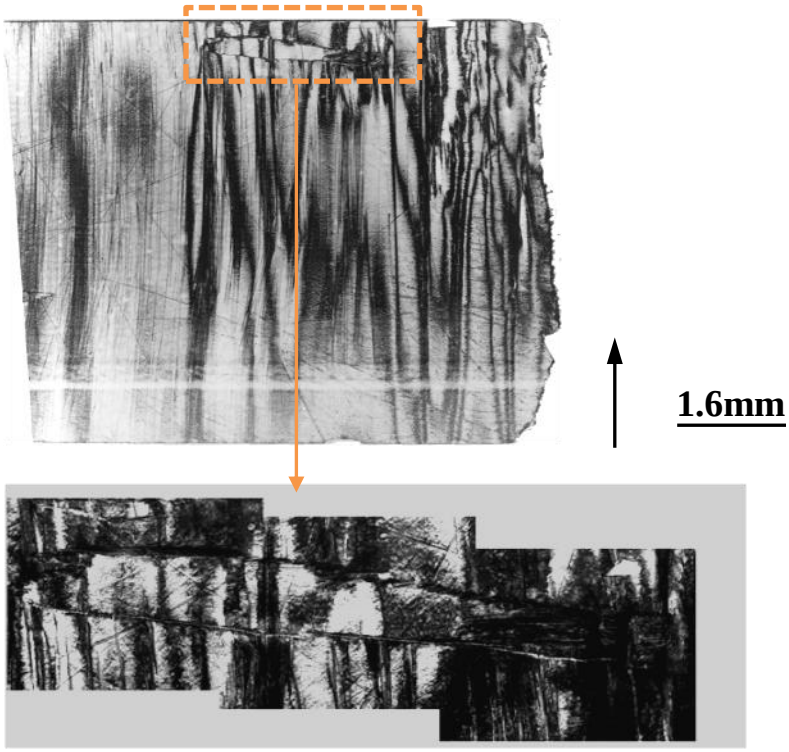

(d)

Figure 20 SWBXT (a) and (b) and monochromatic (c) and (d) (000 ·15) transmission X-ray topogragh of two samples showing the detailed information around polytype inclusion region.

Figure 20 (a)-(d) show details of 00015 transmission x-ray topographs recorded by white beam and monochromatic beam from both samples respectively. Since the basal planes of both the 15R and 6H regions are parallel, no orientation contrast is visible on this reflection. i.e., the 15R and 6H regions appear side by side. However, due to slight differences in bilayer spacing between the 15R and 6H polytypes, strain contrast, appearing as a dark line, is visible at the interface between the two regions. Also visible are long linear features running approximately parallel to the [0001] growth axis. From the contrast, they appear to be threading screw dislocations (see the enlargements in Figure 20) and from their morphology, they appear to be growth dislocations similar to those observed in 6H and 4H-PVT grown crystals. The wide gaps on the left hand-side of the topograph in Figure 20 (a) appear to be grain boundaries comprising planar arrays of threading edge dislocations (**l**=[0001] and **b**=<11-20>) lining up parallel to one of the 11-20 planes (similar to those observed in 6H and 4H-SiC). The wavy line on the bottom edge of the same topograph appears to be the seed interface. This line is wavy because of the lattice rotation associated with built in stress. One can see that all of the screw dislocations in the seed crystal have propagated into the newly grown crystal. Just beyond the seed interface, a lenticular shaped 6H-SiC inclusion can be observed. This inclusion appears to terminate some of the threading screw dislocations propagating from the seed. Close examination of the enlarged image shows that the number of dislocations terminating on the lower side of the inclusion is not the same as the number emanating from the top side of the inclusion into the 15R region (Figure 21 (a)). However, Burgers vector must be conserved so that the net Burgers vector of dislocations terminating on the lower side of the inclusion must be exactly the same as that originating on the upper side of the inclusion. The unequal numbers must therefore be compensated by combining of Burgers vectors of some dislocations into a multiple of the *c*-lattice parameter (again similar to what can happen in 6H and 4H-SiC). Actually, close examination of the images recorded from the 6H inclusions themselves show that they also contain a low density of screw dislocations. For screw dislocations to be admitted into the 6H inclusion from the 15R region below, the Burgers vectors have to be compatible. For example, a 1c dislocation in 15R is not admissible but a 2c could be accepted as a 5c (or 5 1c's). Similar compatibility rules will apply in going from 6H to 15R.

The 00015 transmission topograph shown in Figure 20 (b) and (d) show that the second sample has a similar defect structure to the first sample. This sample also contains a 6H inclusion

region which appears dark green on the optical micrograph. Figure 20 (b) and (d) reveal that the detailed defect structure in this crystal is similar to that of the first sample.

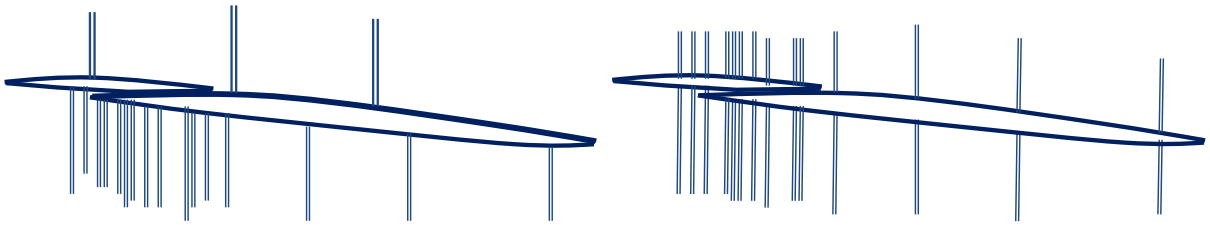

(a) (b)

Figure 21 Schematic diagram of 6H-SiC inclusions with screw dislocations generated during(a) and after (b) the growth of 15R-SiC crystals.

5.4.2. Nucleation Mechanisms

Based on the growth dislocation nature of TSDs present in the samples and the uneven number of TSDs at both sides of the polytype inclusion, we can draw the conclusion that the 6H-SiC polytype inclusions are generated during the growth process of 15R-SiC. Compared to this case, if polytype inclusions are generated after growth with the applications of external stress, densities of screw dislocations on each side of the 6H-SiC polytype inclusion should be the same as dictated by the conservation of Burgers Vector (Figure 21 (b)). We can also conclude that in the case of inclusion generating during growth, screw dislocation are replicated from the seed and phase transformation happens at the growth front.

According to the fact that 6H-SiC polytype inclusions are generated during growth, we need to consider the step flow growth process in SiC. In this type of growth, the spiral steps on the surface of SiC act as growth nucleation sites with active dangling bonds facing outwards on the step riser and thus will react with molecules that drop onto the surface during the growth process and start to wind up around the dislocation core into growth spirals. Therefore the growth front will reproduce the structure of spiral steps and the crystal continues to grow. All steps which contain more than one bilayer in different SiC polytypes can split into several energy-favorable smaller step risers and reproduce the structure of spiral steps simultaneously in the mechanism as single bilayer (Figure 22).

Comparing the stacking sequence of 6H- and 15R-SiC, we can establish a model for polytype transformation from 6H to 15R with the passage of a Shockley partial dislocation through the 15R-SiC structure (see Figure 23) on the bold slip plane creating a small volume of

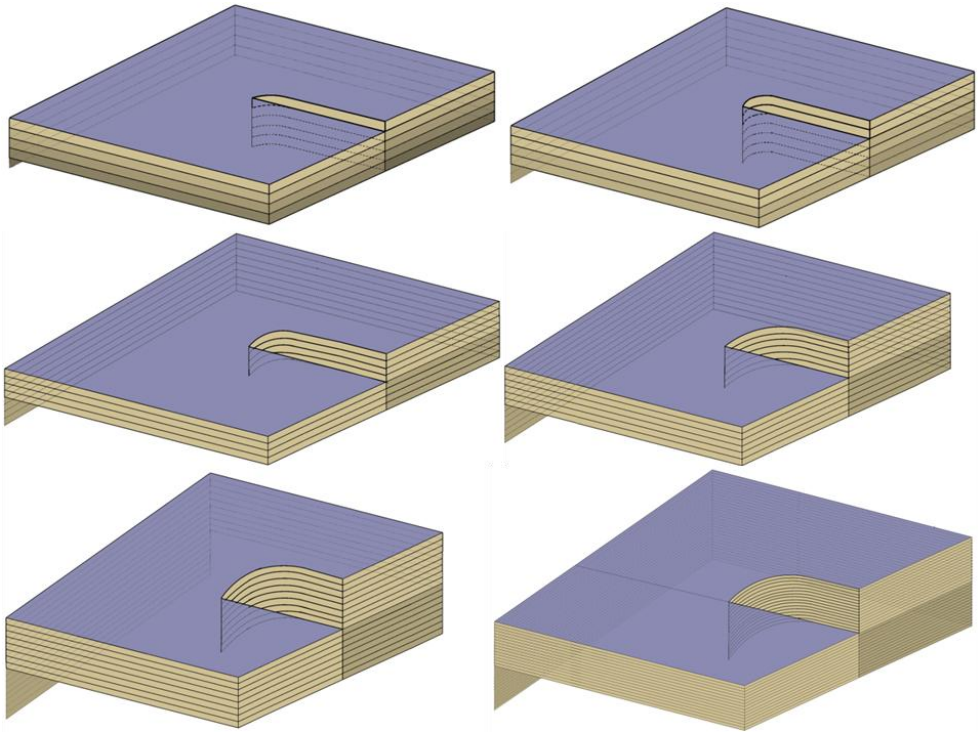

Figure 22 Schematic diagrams of 1c screw dislocation spiral steps (SSs) in 1 bilayer, 2H-, 4H-, 6H-, 8H- and 15R-SiC crystals separately.

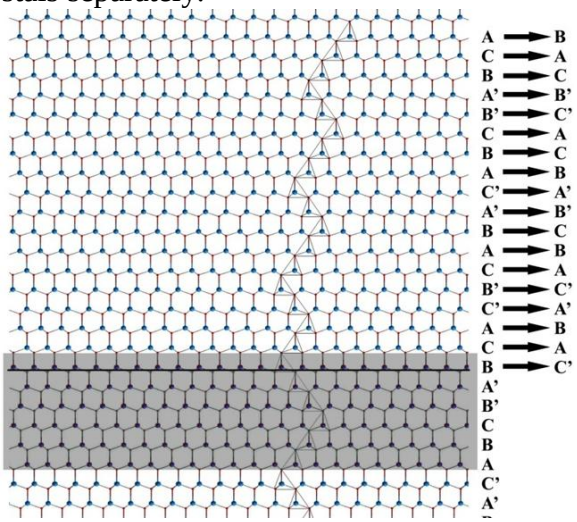

Figure 23 Stacking sequences of the model of polytype transformation from 6H- to 15R-SiC.

6H-SiC structure (shaded region) by changing the stacking sequence of the sixth layer from B to C'. This small volume gets isolated and emerges as a nucleus of 6H-SiC structure during the step flow growth process around a 1c screw dislocation in 15R-SiC. It is also necessary to consider how the screw dislocations interfere with basal plane partial dislocations during growth (Figure 24). The faulted region (lighter blue) gets pinned by the screw dislocation core. More and more

faults pass the dislocation core during growth, pile up and finally form a larger faulted region around the screw dislocation core.

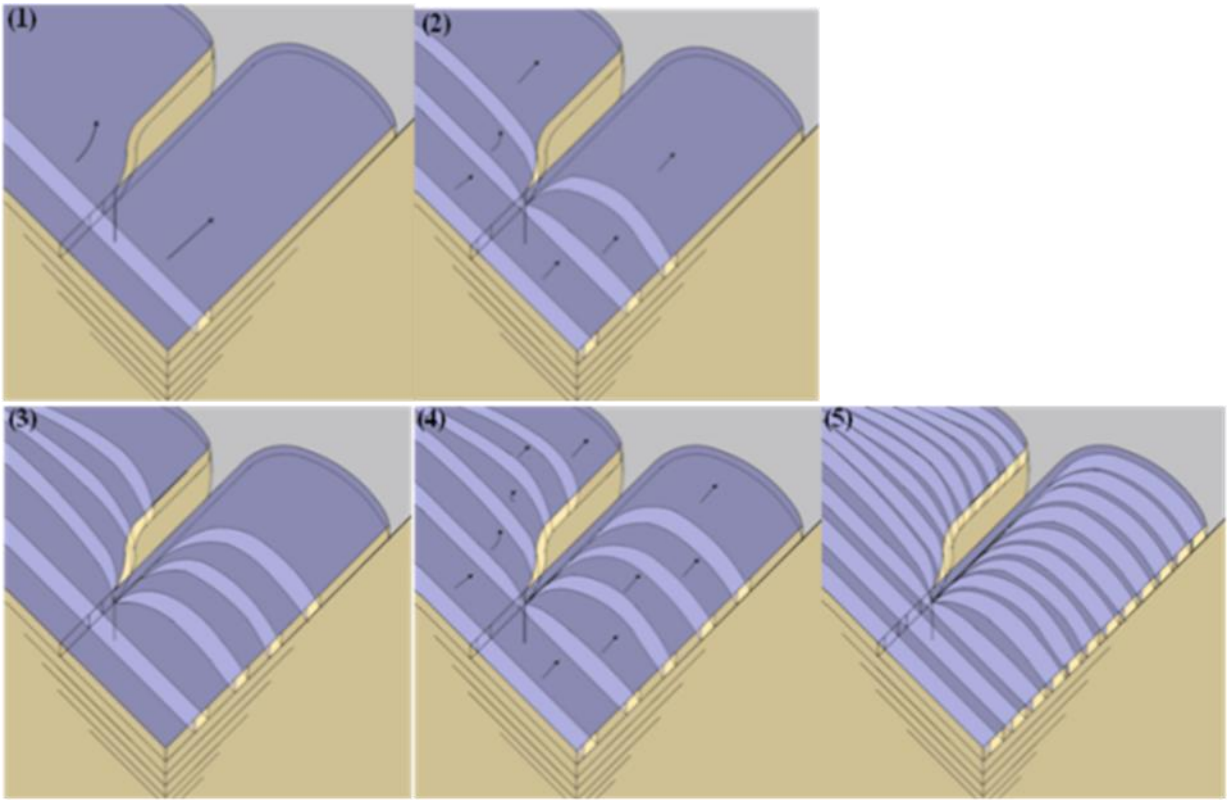

Figure 24 Schematic diagrams of the interference between screw dislocation and basal plane partial dislocations.

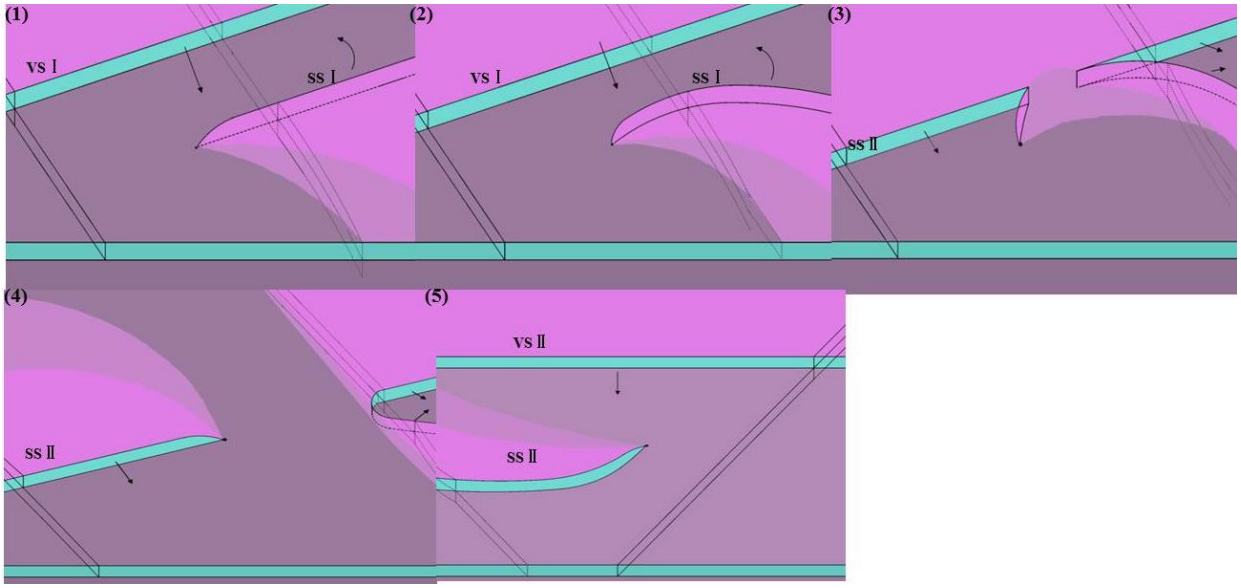

Figure 25 Schematic diagrams of interference between single advancing vicinal step (VS) and spiral step (SS) and the reproduction of spiral step.

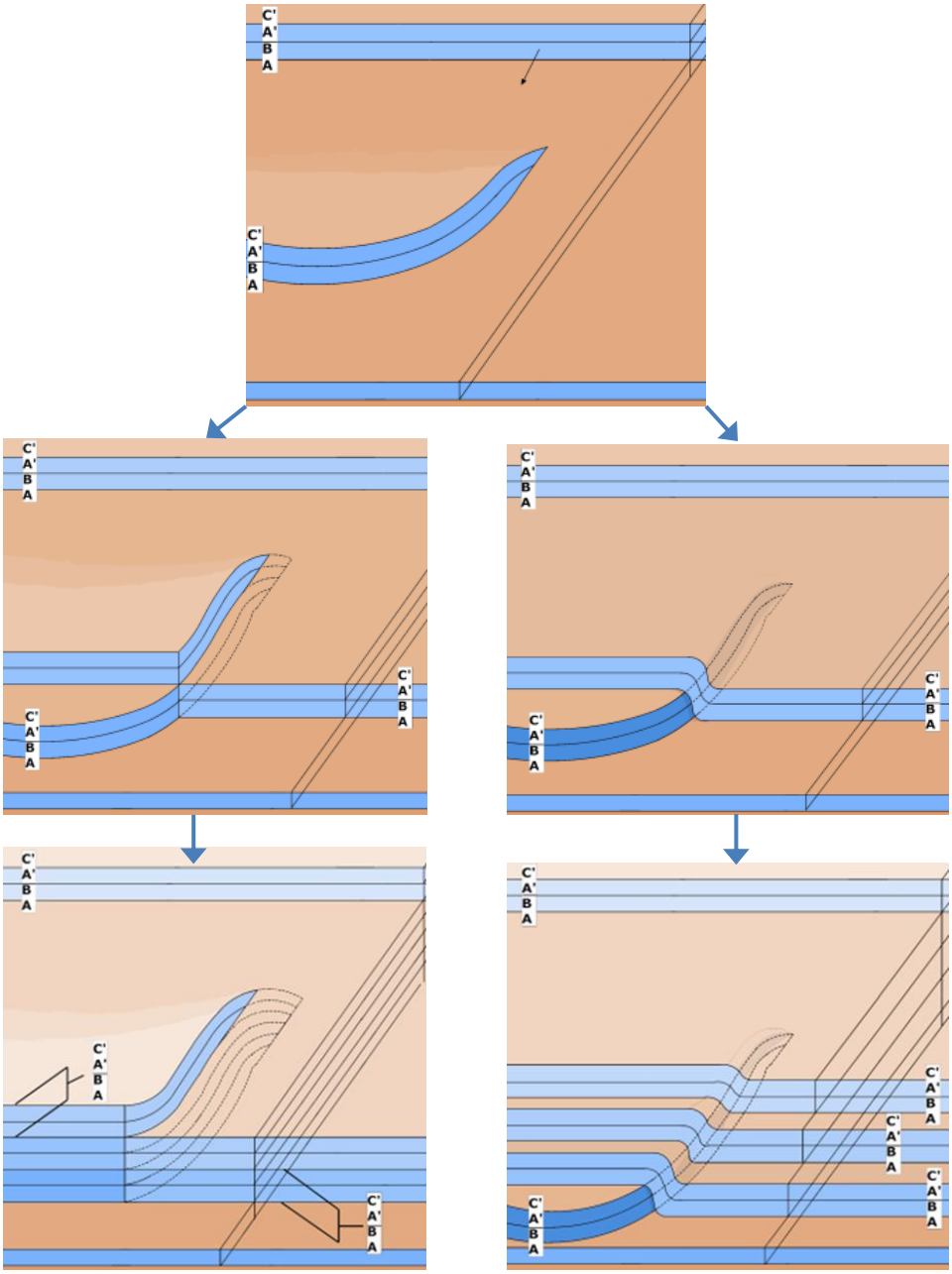

Figure 26 Schematic diagrams showing the interference between advancing vicinal steps (VSs) and SSs with one unit cell height in 4H-SiC. VS can either split causing the reproduction of screw dislocation (left hand-side) or collapse creating Frank partial dislocation (right hand-side).

Figure 25 shows the interference between one bilayer single advancing vicinal step and spiral step. During the step flow growth process, VS I, as the growth front, has the tendency to advance and overgrow toward SS I which is parallel to it. In the meantime, SS I, with active dangling bonds facing outwards, has the tendency to advance toward VS I at the same rate (Figure 25 (1) and (2)). A new SS with changed orientation is generated after SS I and VS I

coalesce. The left portion of VS I becomes connected to the dislocation core and forms SS II which is perpendicular to VS while the right portion remains VS together with the rest portion of SS I (Figure 25 (3) and (4)). SS II continues to advance toward the next VS and this whole process gets repeated during the entire growth process (Figure 25 (5)).

Take 1c 4H screw dislocation spiral step (SS) with stacking sequences ABA'C' as an example. Figures 26 show the interference between advancing vicinal steps (VSs) and SSs which are perpendicular to each other with one unit cell height in step flow growth of 4H-SiC. When the advancing VS meet the dislocation core, VS can either split into different layer heights causing the reproduction of screw dislocation (see the diagrams on the left hand-side of Figure 26) or, it can overgrow the distorted dislocation region and collapse at the dislocation spiral creating Frank partial dislocation (see the diagrams on the left hand-side of Figure 26).

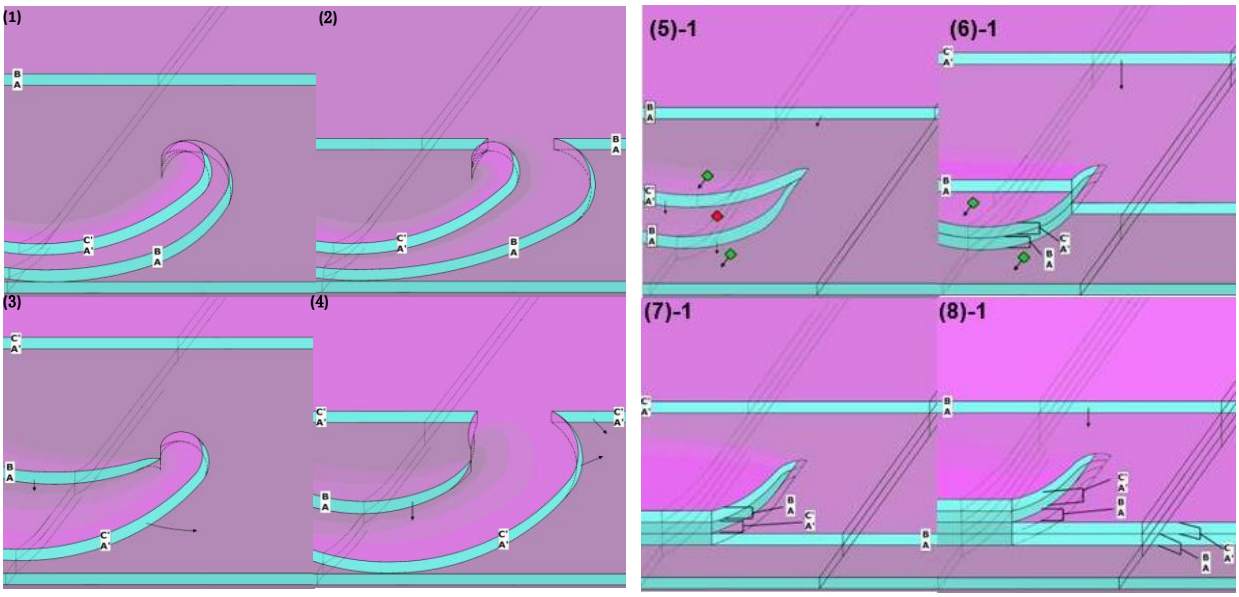

Figure 27 Schematic diagrams showing the interference between advancing vicinal steps (VSs) and SSs with fractional unit cell height in 4H-SiC. Note that in this case, terraces labeled red cannot be overgrown and thus causes step bunching.

Figure 27 show the interference between VS and SS with half unit cell height in 4H-SiC. Two SSs wind up toward the VS terraces with the active front parallel to the VS (Figure 27 (1)). After they coalesce, two newly formed dislocation spirals are produced sequentially with the growth front perpendicular to the next VS (Figure 27 (2)-(4)). In this case, terrace which is labeled red cannot be overgrown (Figure 27 (5)-1) by the next VS according to the stacking roles, i.e., layer B cannot accommodate layer A. This prevents VS with stacking sequences AB to overgrow SS with stacking sequence AB, which causes steps to pile up and leads to step

bunching (Figure 27 (6)-(8)-1). In another case which is shown in Figure 28, all the terraces can be overgrown due to stacking sequence change by the passage of basal plane dislocation. VS can

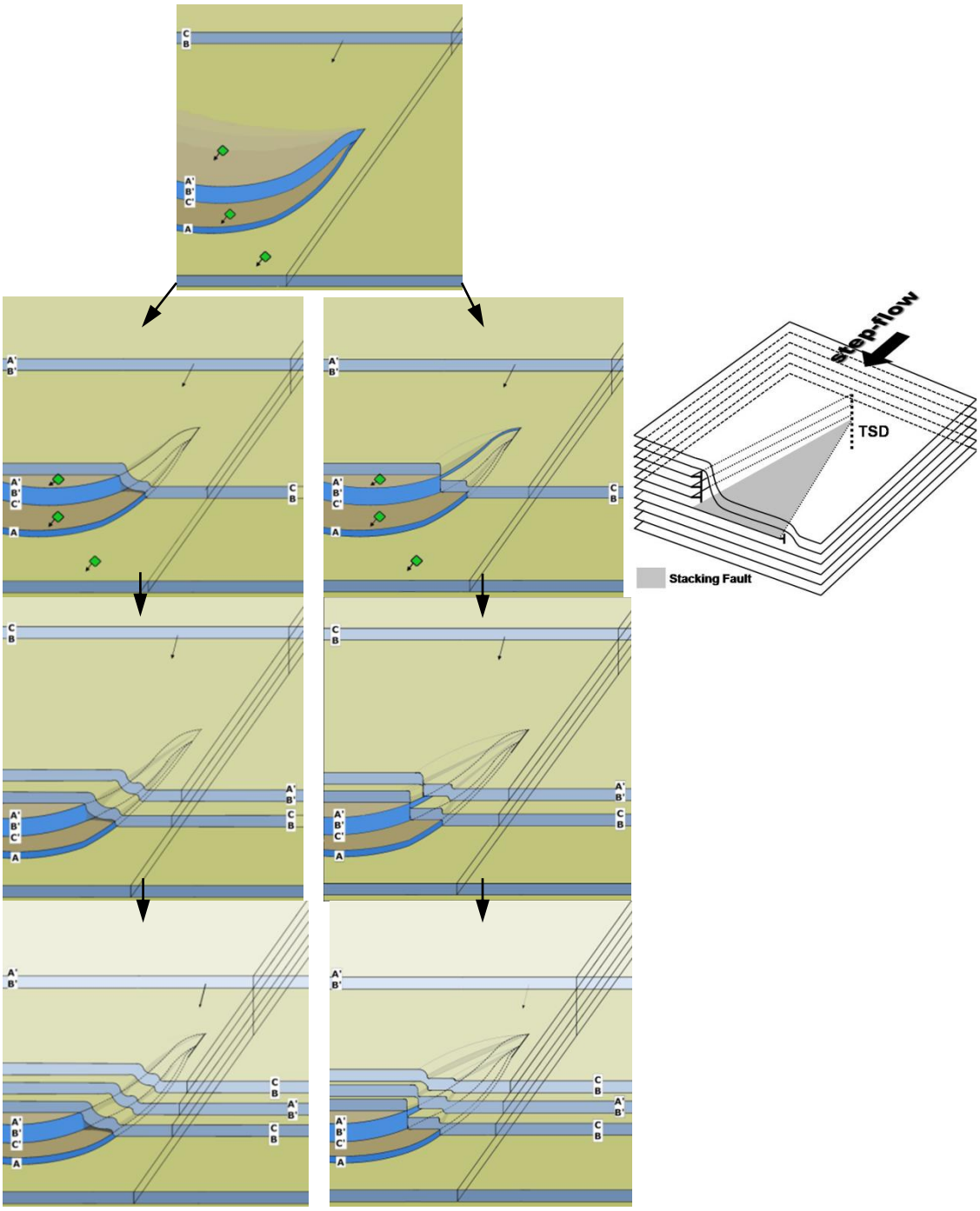

Figure 28 Schematic diagrams showing the interference between advancing vicinal steps (VSs) and SSs with fractional unit cell height in 4H-SiC. Note that in this case, terraces labeled red can be overgrown by the next VS.

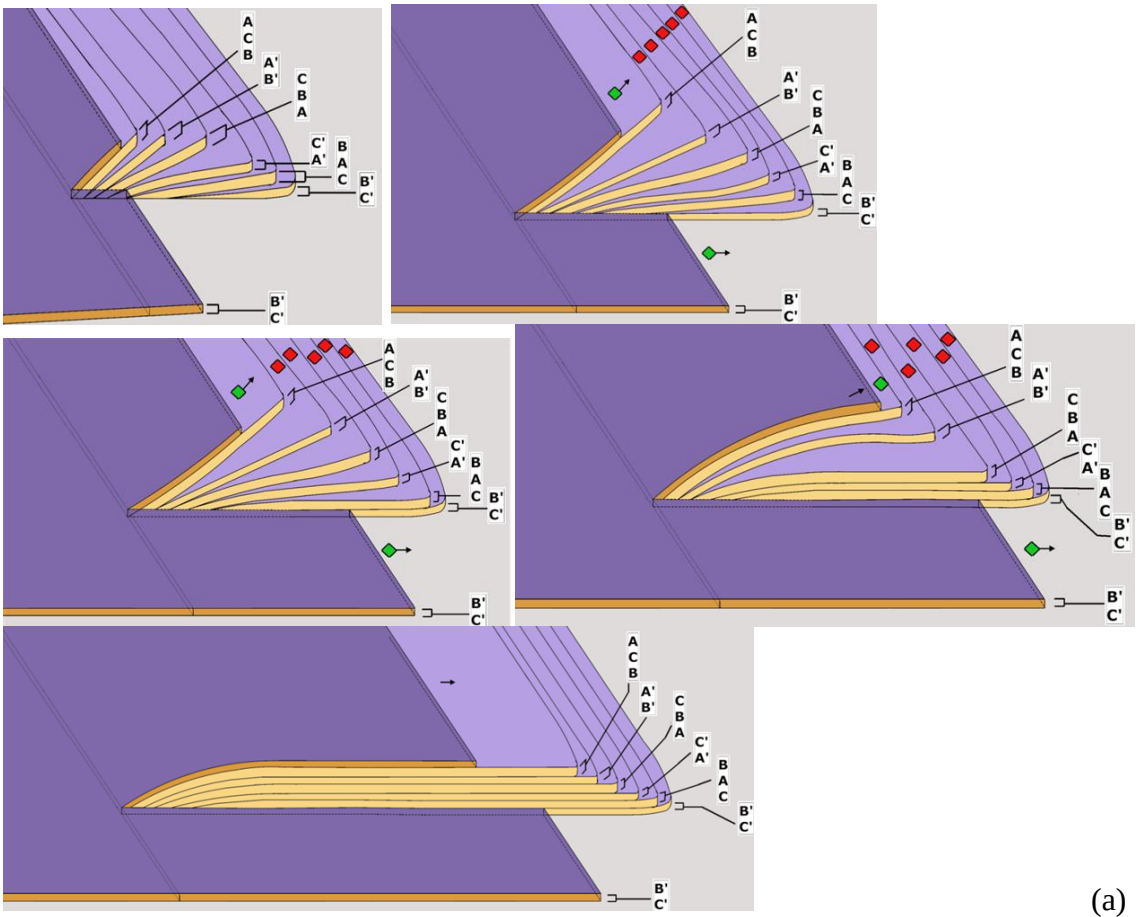

(a)

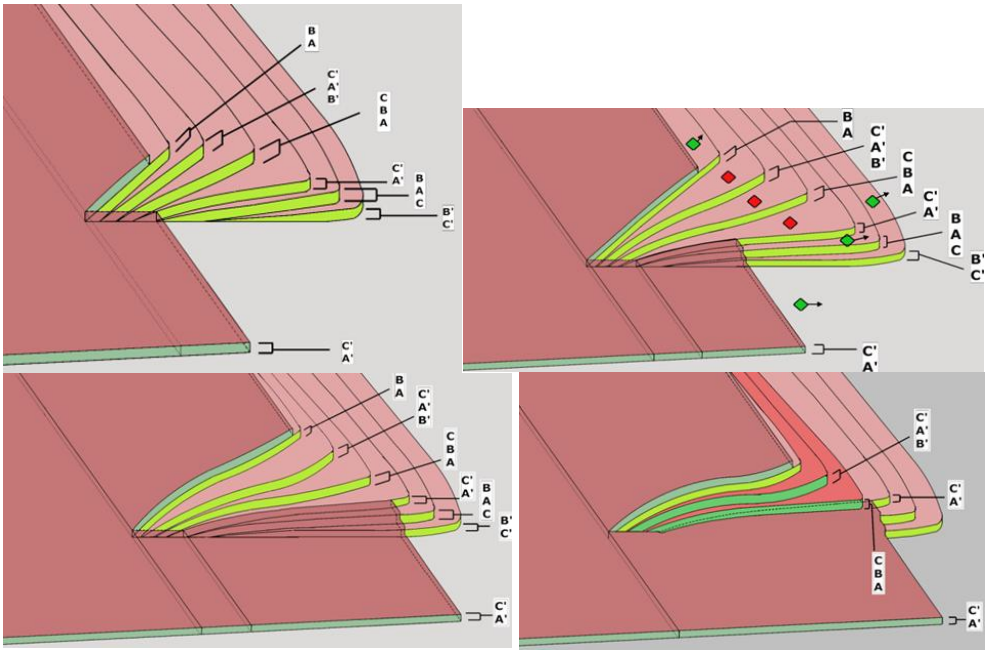

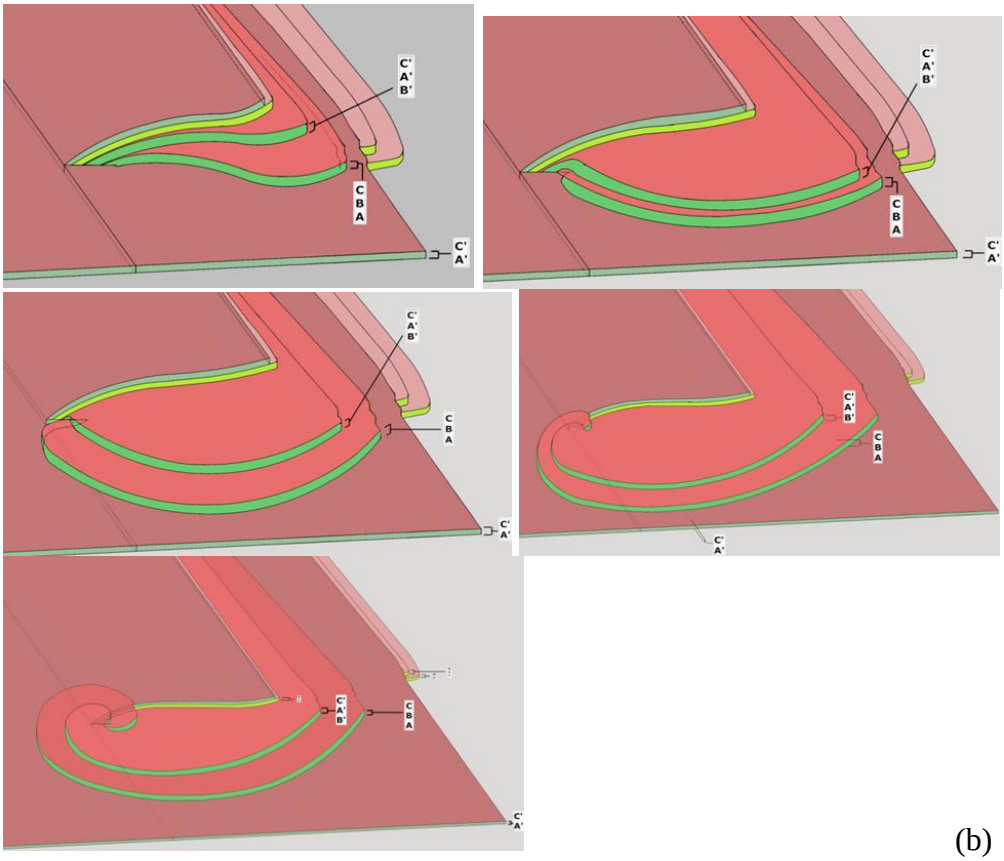

(b)

Figure 29 (a) Schematic diagrams of step flow growth in 15R-SiC without the passage of partial dislocation; (b) Schematic diagrams of step flow growth in 15R-SiC with the passage of partial dislocation.

either overgrow the distorted dislocation region and collapse at the dislocation spiral creating Frank partial dislocations and Frank Faults (see the diagrams on the left hand-side of Figure 28) or, it could split into different layer heights causing the reproduction of screw dislocation and the formation of prismatic faults (see the diagrams on the right hand-side of Figure 28).

In step flow growth of 15R-SiC, with the absence of basal plane partial dislocation, terraces labeled green (Figure 29 (a)) can continue to be overgrown by the vicinal step while the other ones cannot according to the stacking rules. This process will lead to the split of vicinal steps at the dislocation core, step bunching and reproduction of the 1C 15R screw dislocation around the dislocation core.

Figure 29 (b) shows the step flow growth in 15R-SiC with the passage of partial dislocation resulting in the change of stacking sequences. More terraces with green labels can now continue to be overgrown by the vicinal step according to the stacking rules. 9/15 of 1c 15R

screw dislocation Burgers Vector gets suppressed by overgrowth of the advancing vicinal step converting parts of the TSD Burgers vector into Frank partial dislocations with associated Frank faults in between and leave behind a small nucleus of 6H-SiC structure. The 6H-SiC structure then is reproduced and form the 6H-SiC inclusion.

5.4.3. HRTEM results

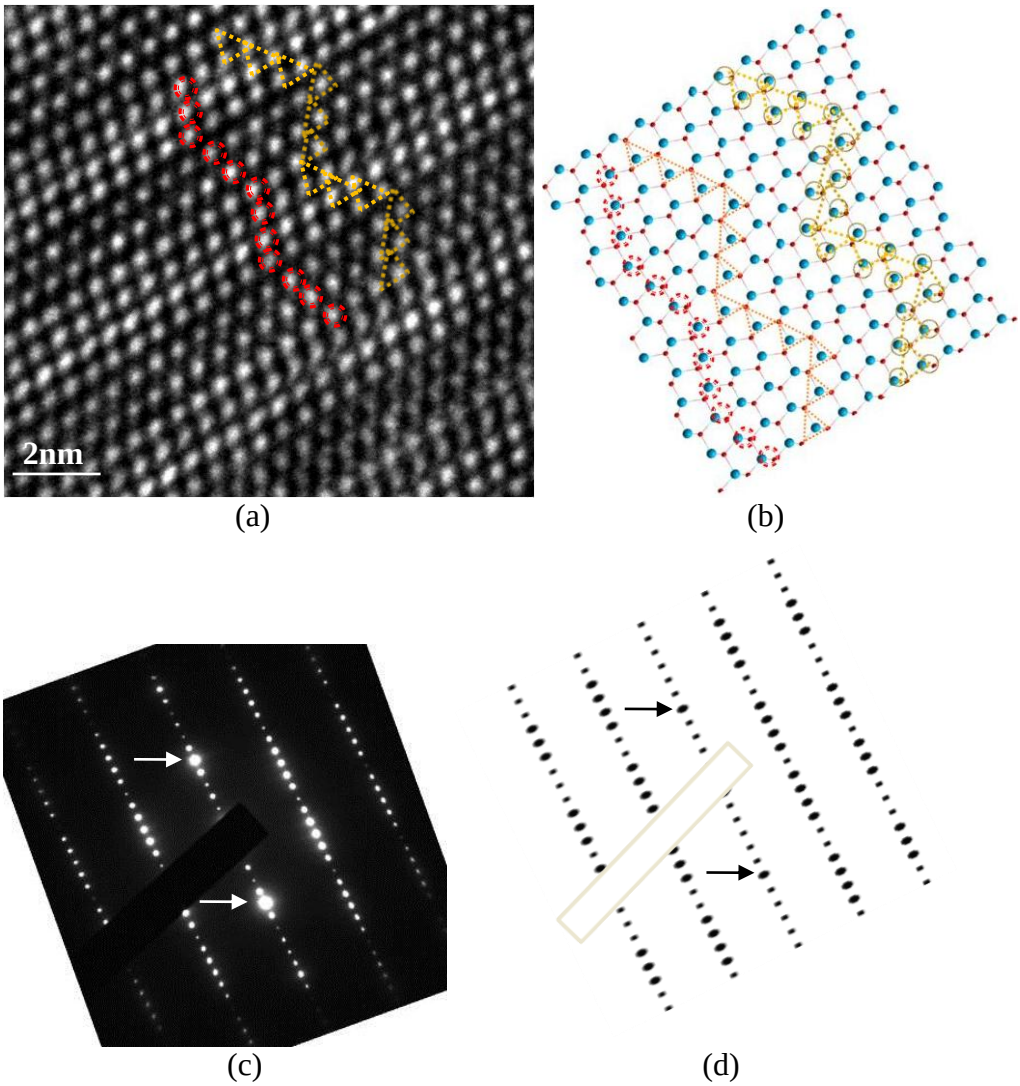

Figure 30 (a) HRTEM image (M=1m) of pure 6H-SiC region; (b) Simulated atomic model of 6H-SiC structure; (c) SAD pattern from the pure 6H-SiC region; (d) Simulated diffraction pattern of 6H-SiC;

(a) (b)

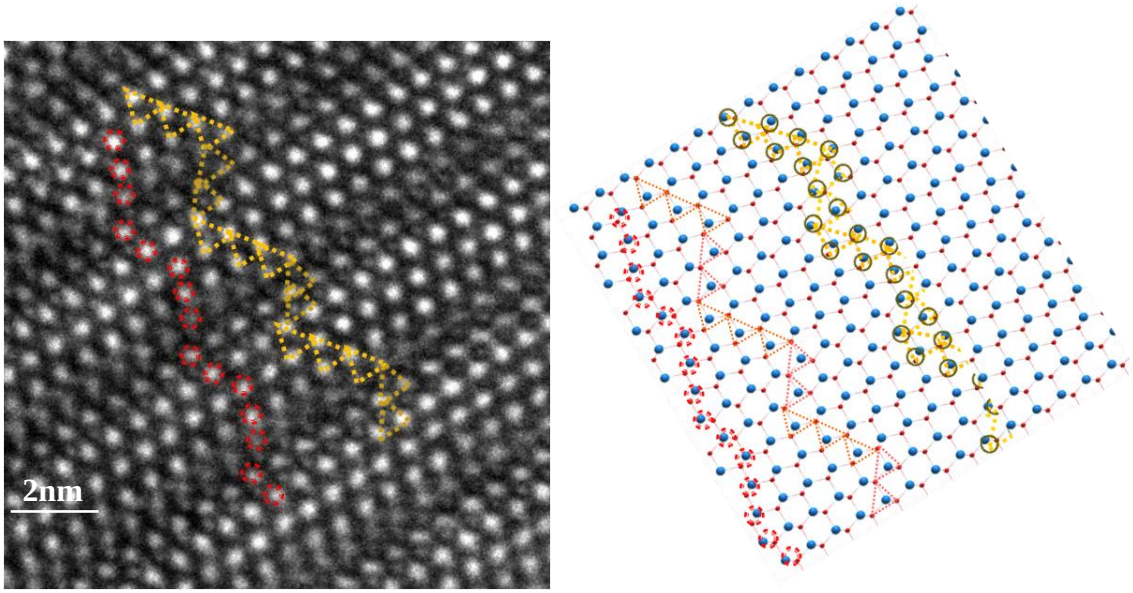

(c) (d)

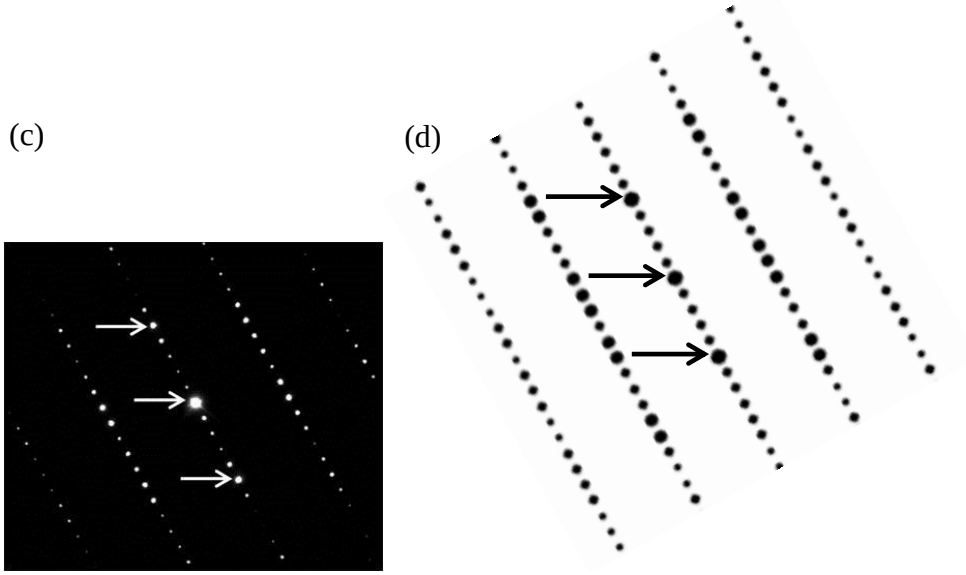

Figure 31 (a) HRTEM image (M=1m) of pure 15H-SiC region; (b) Simulated atomic model of 15H-SiC structure; (c) SAD pattern from the pure 15H-SiC region; (d) Simulated diffraction pattern of 15H-SiC;

The sample was then studied using HRTEM. Figure 30 (a) shows the HRTEM image obtained from a pure 6H-SiC region with (11-20) viewing direction in the specimen. Compared with the simulated atomic model with the same viewing direction (Figure 30 (b)), it can be seen that pairs of Si-C atoms diffract as units appearing as one bright spot in the image. Three neighboring bright spots comprise one tetrahedron with untwinned or twinned orientation. Three

untwined and three twinned tetrahedron form the structure of 6H-SiC and the stacking sequence of ABCB'A'C'. Selective area diffraction (SAD) pattern of 6H-SiC was also obtained from the same region (Figure 30 (c)) which perfectly matches with the simulated diffraction pattern (Figure 30 (d)).

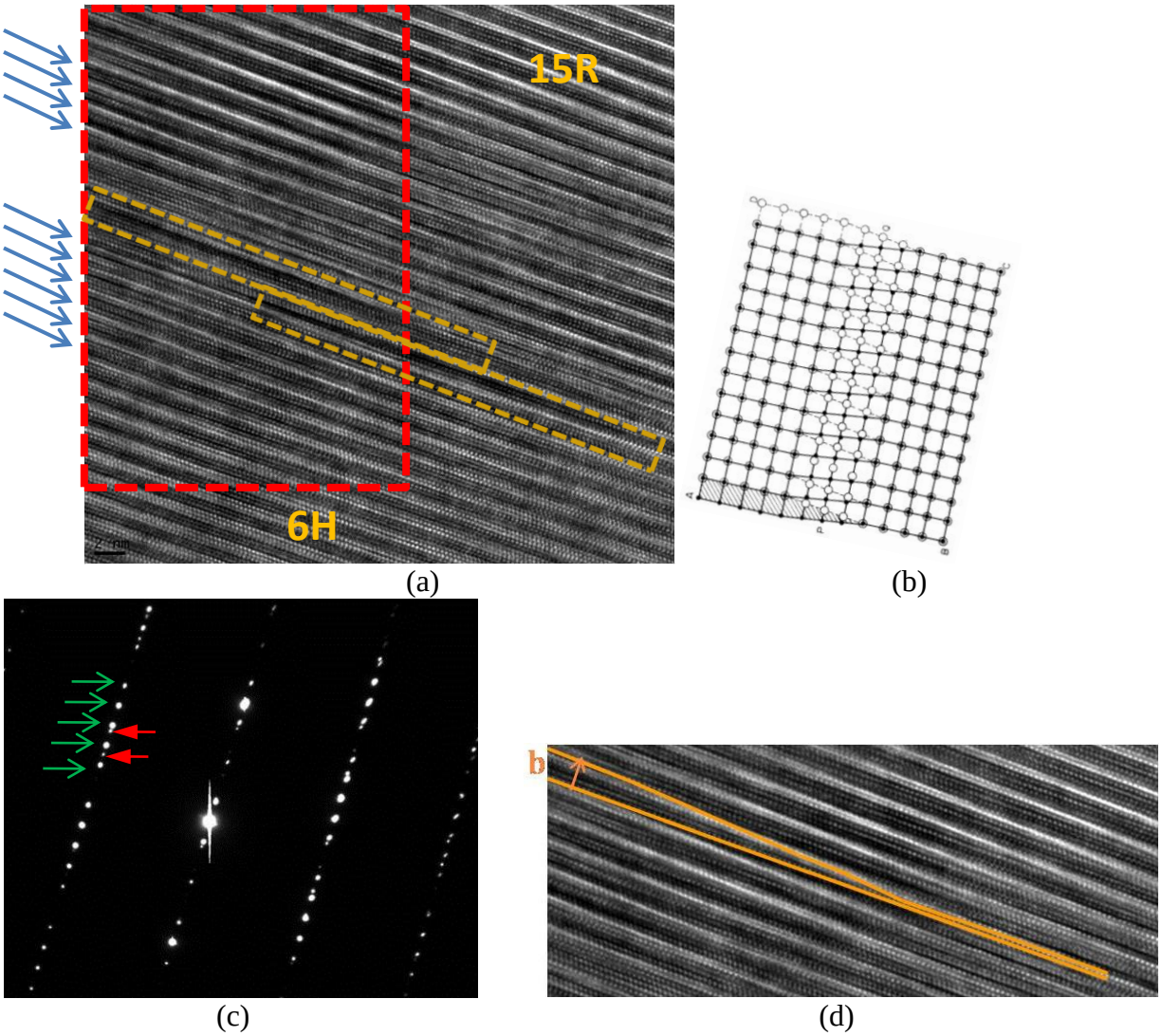

(a) (b)

(c) (d)

Figure 32 (a)HRTEM image (M=600K) recorded from the transitional layer between 15R- and 6H-SiC; (b) schematic diagram of screw dislocation; (c) SAD pattern from the mixed region; (d)Enlarged HRTEM image showing 1c 6H screw dislocation.

HRTEM image was also obtained from pure 15R-SiC region with (11-20) viewing direction (Figure 31 (a)). The bright contrast comes from electron diffraction of Si-C clusters (Figure 31 (b)). Two untwined tetrahedral are followed by three twinned which forms 15R-SiC structure and the stacking sequence of B'A'BCAC'B'CABA'C'ABC. SAD pattern from pure

15R-SiC region (Figure 31 (c)) perfectly matches with the simulated diffraction pattern (Figure 31 (d)).

Then we were able to locate the transition region between 15R- and 6H-SiC in the specimen based on the change in SAD pattern. Figure 32 (a) shows the HRTEM image taken from the mixed region. There is screw dislocation in between which appears to be 1c 6H screw dislocation (Figure 32 (d)) corresponding to the schematic diagram of screw dislocation (Figure 32(b)). Furthermore, the evidence of Frank Fault and Frank partial dislocations is present in the center region of the image appearing as extra atomic planes. SAD pattern was also obtained from the same region (Figure 32 (c)) indicating diffraction patterns from both 6H- and 15R-SiC. Regular green arrows point to the five diffraction spots from 6H-SiC and red bold ones point to two spots from 15R-SiC. The remaining two spots overlap with those from 6H-SiC.

5.5. Conclusions

A new model is presented for the nucleation mechanism of 6H-SiC polytype inclusions in Physical Vapor Transport (PVT) grown 15R-SiC boules. Inhomogeneous densities of screw dislocations replicated from the seed lead to uneven growth rates in the boule resulting in a quasi-vicinal growth surface. Subsequent interference between advancing vicinal growth steps and screw dislocation spiral growth steps lead to complex step overgrowth processes which can suppress all or part of the 15R 1c screw dislocation Burgers vector through the creation of Frank faults and Frank partial dislocations on the basal plane. Combined with stacking shifts induced by the passage of basal plane partial dislocations it is shown that suppression of 9/15 of the 15R 1c dislocation Burgers vector by such step overgrowth can leave behind a residual Burgers vector corresponding to a 1c dislocation in 6H-SiC. The residual dislocation then acts as a nucleus for reproduction of the 6H SiC structure at the surface of the 15R crystal.

6. $B_{12}As_2$ grown on on-axis c-plane (0001) 4H-SiC

6.1. Outline

A detailed analysis of the microstructure in $B_{12}As_2$ epitaxial layers grown by CVD on on-axis (0001) 4H-SiC substrates is presented. Synchrotron white beam x-ray topography (SWBXT) enabled macroscopic characterization of the substrate/epilayer ensembles and revealed the presence of a quite homogenous solid solution of twin and matrix epilayer domains forming a submicron mosaic structure. The basic epitaxial relationship was found to be $(0001)_{B12As2}$<1-100>$_{B12As2}$||$(0001)_{4H\text{-}SiC}$<1-100>$_{4H\text{-}SiC}$ and the twin relationship comprised a 180° (or equivalently 60°) rotation about $[0001]_{B12As2}$ in agreement with previous reports. Cross-sectional high resolution transmission electron microscopy (HRTEM) and scanning transmission electron microscopy (STEM) both revealed the presence of an ~20nm thick, disordered transition layer which is shown to be created by the coalescence of a mosaic of translational and rotational variant domains nucleated at the various types of nucleation site available on the (0001) 4H-SiC surface. In this transition layer, competition between the growth of the various domains is mediated in part by the energy of the boundaries created between them as they coalesce. Boundaries between translational variant domains are shown to have unfavorable bonding configurations and hence high energy. These high energy boundaries can be eliminated during mutual overgrowth by the generation of a $1/3[0001]_{B12As2}$ Frank partial dislocation which effectively eliminates the translational variants. This leads to an overall improvement in film quality beyond thicknesses of ~20nm as the translational variants grow out leaving only the twin variants. (0003) twin boundaries in the regions beyond 20nm are shown to possess fault vectors such as $1/3[1\text{-}100]_{B12As2}$ which are shown to originate from the mutual shift between the nucleation sites of the respective domains.

6.2. Introduction

Previous effort on CVD growth of $B_{12}As_2$ on c-plane (0001) 4H-SiC has observed rotational and translational variants in the epilayers. However, the formation mechanism of these

structural variants, which could be vital to guide better crystal growth, has remained unclear. In addition, there has been no systematic analysis of the defect structures in the films grown on c-plane 4H-SiC substrates at an atomic scale. In order to better understand the defect structure and growth mechanism which are helpful to find possible solutions to improving film quality, $B_{12}As_2$ films grown on c-plane (0001) 4H-SiC substrates are investigated.

6.3. Experimental

(0001) 4H-SiC substrates were used for the CVD growth of $B_{12}As_2$. The $B_{12}As_2$ films were synthesized with gaseous precursors of 1% B_2H_6 in H_2 and 2% AsH_3 in H_2. The films were deposited at 1450 ℃ and 100 Torr of reactor pressure for 30 minutes. The rhombohedral epitaxial films of $B_{12}As_2$ had a nominal thickness of 4 μm. The cross-sectional TEM samples were made parallel to $(11\text{-}20)_{4H\text{-}SiC}$, which is parallel to $(11\text{-}20)_{B12As2}$, since this orientation clearly reveals the $B_{12}As_2$ twin boundaries. Note that indices referenced to the four index hexagonal system are utilized. These can easily be related to the three index rhombohedral system using the standard relationship such that $[11\text{-}20]_{B12As2}$ is parallel to $[10\text{-}1]_{B12As2}$, $[0001]_{B12As2}$ is parallel to $[111]_{B12As2}$, and $(0003)_{B12As2}$ is equivalent to $(111)_{B12As2}$. The sample was mechanically thinned and polished using the standard T-tool technique employing 30 μm, 15 μm, 6 μm, 3 μm, 1 μm, 0.5 μm and 0.1 μm diamond lapping films and then ion milled to electron transparency. High resolution TEM was carried out using a JEOL 2100 system with an electron voltage of 200keV and STEM using a Hitachi HD 2700C system at Brookhaven National Laboratory. SWBXT was performed on as-grown films at the Stony Brook synchrotron topography facility at the National Synchrotron Light Source. The white beam x-ray had wavelength spectrum ranging from 0.01Å to 2.00Å, in which the beam peak had a wavelength of 0.8 Å. The transmission Laue patterns were recorded on Agfa x-ray film at a sample to film distance of 11cm. Structural projections were produced using the commercial software package CrystalMaker.

6.4. Results and discussion

6.4.1. SWBXT and SEM results

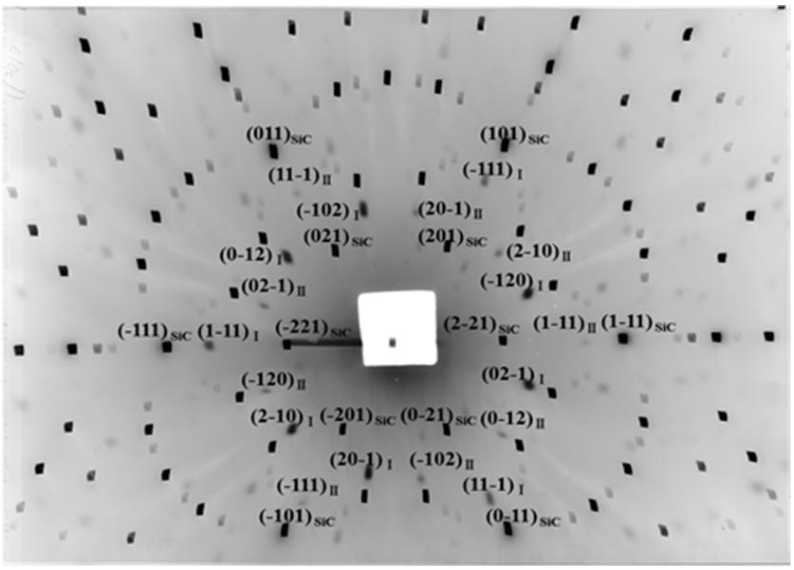

Figure 33 Laue pattern of IBA on on-axis c-plane 4H-SiC with subscripts I and II showing diffraction spots from IBA matrix and twin.

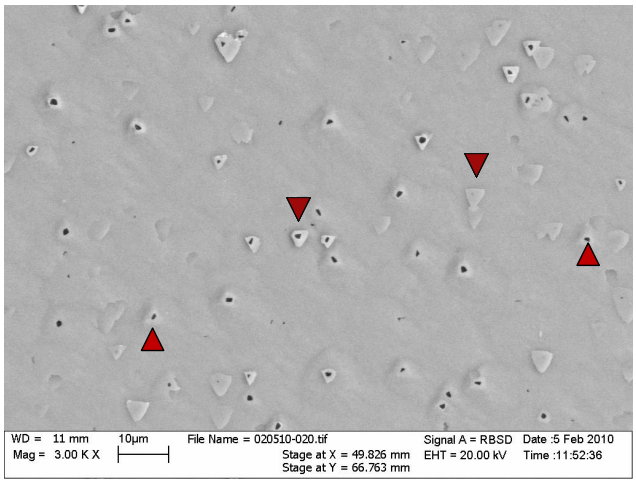

Figure 34 SEM image of $B_{12}As_2$ film on on-axis c-plane 4H-SiC indicating $B_{12}As_2$ matrix and twin orientations.

Figure 33 shows a transmission synchrotron x-ray Laue pattern from a $B_{12}As_2$ epitaxial layer grown on an on-axis c-plane 4H-SiC substrate recorded with the epilayer as the beam exiting surface. The $B_{12}As_2$ produced only weak and diffuse diffraction spots that exhibited the type of streaking that is indicative of mosaicity. Detailed indexing analysis not only confirms the expected $(0001)_{B12As2}\langle 1\text{-}100\rangle_{B12As2}\|(0001)_{4H\text{-}SiC}\langle 1\text{-}100\rangle_{4H\text{-}SiC}$ in epitaxial relationship, but also shows that the $B_{12}As_2$ is present in two distinct orientations related by a 180^o twin (or equivalently 60^o) rotation about the $(0001)_{B12As2}$ plane normal. The strong, well-defined 4H-SiC diffraction spots are labeled with indices with subscripts "SiC" while the more diffuse $B_{12}As_2$ spots are labeled with indices with subscripts of roman numerals I or II indicating matrix or twin

orientation (in some cases the matrix and twin reflections coincide). The overall appearance of the $B_{12}As_2$ matrix and twin diffraction spots is consistent with a mosaic and quite homogenous solid solution of twin and matrix domains which are of a size that is below the spatial resolution of X-ray topography (a few microns). This was corroborated with SEM observations (Figure 34) which reveals a composite structure comprising two types of equilateral triangular feature, each with dimensions of several μm, which are mutually rotated by 180^o about the surface normal in agreement with previous observations. These triangular grains correspond to twin related $B_{12}As_2$ domains. The morphology of the triangular features was determined using orientation information provided by SWBXT and found to consist of a flat $(0001)_{B12As2}$ facet bounded by three equivalent $(1\text{-}100)_{B12As2}$ facets. Further microstructural information, in particular concerning the boundaries between the various domains, was provided by HRTEM and STEM studies carried out on cross-sectional samples.

6.4.2. TEM and STEM results

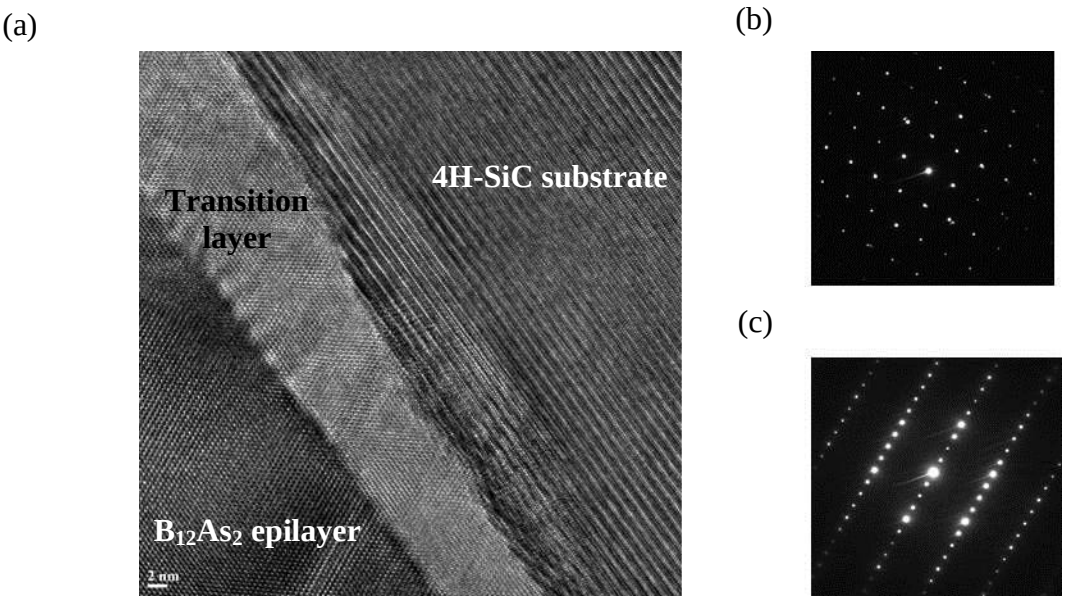

Figure 35 Cross-sectional TEM image recorded along [11-20] revealing a transition layer located between the $B_{12}As_2$ layer and the 4H-SiC substrate. (b) SAD pattern of the $B_{12}As_2$ epilayer recorded along the [11-20] zone axis. (c) SAD pattern of the 4H-SiC substrate recorded along the [11-20] zone axis.

High resolution cross-sectional TEM observation along the [11-20] zone axis (Figure 35 (a)) reveals a transition layer located between the film and the substrate. Figure 35 (b) and (c) show selective area diffraction (SAD) patterns recorded from a local area in the $B_{12}As_2$ film and

the 4H-SiC substrate respectively, confirming the epitaxial relationship determined from SWBXT**.** Detailed simulation reveals that the epilayer consists of an overlap of twinned $B_{12}As_2$ domains.

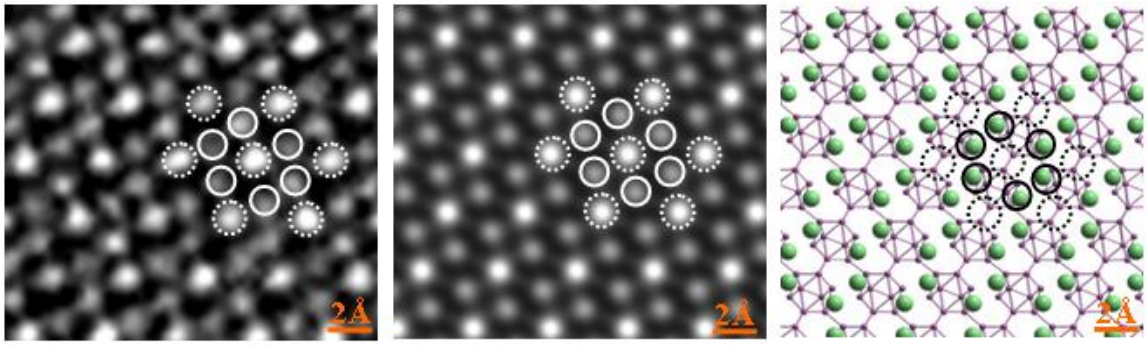

(a) (b) (c)

Figure 36 (a) Experimental HRTEM image recorded from a defect-free region of the $B_{12}As_2$ film viewed along [11-20]; (b) Simulated HRTEM image of the $B_{12}As_2$ film corresponding to (a) with defocus=3nm and sample thickness=8.6nm; (c) Atomic configuration of the $B_{12}As_2$ structure with the same projection direction as (a).[19]

HRTEM was employed to provide information on the atomic configurations present in the various domains and the boundaries between them. However, HRTEM images do not always correspond to intuitive projections of the crystal lattice. The contrast and the shape of the features shown in HRTEM images often vary as the defocus condition and the change of sample thickness. As a consequence, it's necessary to bridge the gap between the recorded HRTEM images and the crystal itself. Multislice simulation [49] is an effective method to interpret and accurately assign the atomic origins to the various features observed on HRTEM images. Chen et al [19] proposed the interpretation of HRTEM images of $B_{12}As_2$ epilayers grown on SiC substrates by comparing the results of multislice simulation and the projections of the crystal structure carried out using CaRine 4.0 (Figure 36). Detailed comparison between the observed and simulated images and the CaRine projections indicates that the bright spots marked by the dotted circles in both experimental and simulated images as well as in the structural projection arise from neighboring B columns, while those marked by the solid circles arise from columns comprising As atoms and the B atoms which project closest to them. Using a similar approach, HRTEM of the twinned region of $B_{12}As_2$ epilayer was used to investigate the detailed atomic configurations present in the various domains and at the various interfaces between them. In addition, comparison of the HRTEM images with models of the potential bonding configurations

available at the various nucleation sites on the (0001) 4H-SiC surface sheds considerable light on the nucleation and growth mechanisms of the $B_{12}As_2$ film.

While rotational variants are readily observable on HRTEM images, detailed observation of the atomic configurations across (0003) twin boundaries can provide verification of the twin nucleation sites on the SiC surface. Figure 37 (a) shows a STEM image recorded from a region of the $B_{12}As_2$ film close to the interface containing an (0003) twin boundary. Figure 37 (b) is the magnified image of the interface region in Figure 37 (a). If this boundary originated from the overgrowth of a twinned island across an untwinned island, the shifts between the twin and matrix nucleation sites should be manifested in the (0003) twin boundary. The twin boundary shown in Figure 37 (a) exhibits a shift of around 3.56Å, corresponding to $1/3[1\text{-}100]_{B12As2}$, thus confirming the formation mechanism. Such shifts were commonly observed in twin boundaries throughout the film. This type of twin boundary can be referred to as a "faulted twin boundary".

In addition to providing information on the nucleation sites, STEM of the twin boundaries in comparison with CrystalMaker structural projections enables the possible bonding configurations across the observed (0003) twin boundaries to be assessed. For the faulted twin boundary exhibiting the $1/3[1\text{-}100]_{B12As2}$ shift, the structure proposed in Figure 37 (c) maintains reasonable bonding and agrees well with the STEM observations.

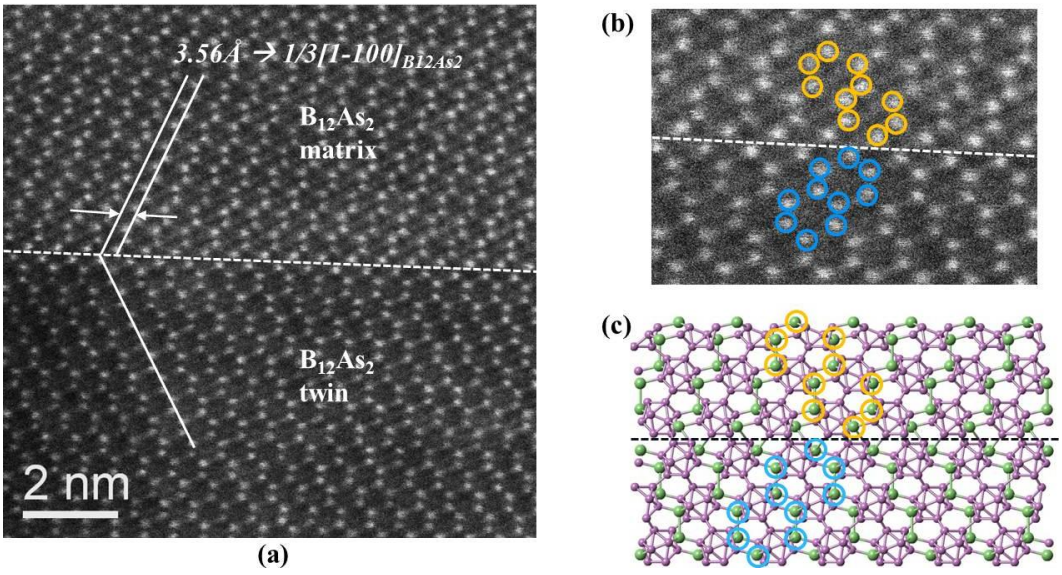

Figure 37 High resolution STEM image of the film ((a) and (b)) taken along [11-20] on on-axis c-plane 4H-SiC and corresponding crystal visualization showing the postulated atomic configuration across a $\{0003\}_{B12As2}$ twin boundary with $1/3 <1\text{-}100>_{B12As2}$ shift. The solid circles stand for the projection of columns comprising arsenic atoms.

6.5. Conclusions

The microstructure in $B_{12}As_2$ epitaxial layers grown by CVD on on-axis (0001) 4H-SiC substrates has been analyzed in detail. SWBXT enabled macroscopic characterization of the substrate/epilayer ensembles and revealed the presence of a quite homogenous solid solution of twin and matrix epilayer domains forming a submicron mosaic structure. The growth orientation of the epilayer with respect to the substrate was determined to be $(0001)_{B12As2}$<1-100>$_{B12As2}$||$(0001)_{4H\text{-}SiC}$<1-100>$_{4H\text{-}SiC}$. $B_{12}As_2$ twinned domains were found in the epilayer and the twinning relationship consisted of a 180° (or equivalently 60°) rotation about $[0001]_{B12As2}$ in agreement with previous reports. HRTEM observation revealed an evolution of the film microstructure from an ~20nm thick disordered mosaic transition layer to a more ordered structure. The transition layer was suggested to arise from the coalescence of translational and rotational variant domains nucleated at the various nucleation sites on the (0001) 4H-SiC surface. In the transition layer, competition between the growth of the various domains is mediated in part by the energy of the boundaries created between them as they coalesce. Boundaries between translational variant domains are shown to have unfavorable high-energy bonding configurations while the formation of a $1/3[0001]_{B12As2}$ Frank partial dislocation enabled elimination of these high energy boundaries during mutual overgrowth. Consequently the film quality beyond thicknesses of ~20nm can be improved as the translational variants grow out leaving only the twin variants. (0003) twin boundaries in the regions beyond 20nm are shown to possess fault vectors such as $1/3[1\text{-}100]_{B12As2}$ which are shown to originate from the mutual shift between the nucleation sites of the respective domains.

7. $B_{12}As_2$ grown on off-axis c-plane 4H-SiC and elimination of degenerate epitaxy

7.1. Outline

Epitaxial growth of $B_{12}As_2$ on 4H-SiC substrates intentionally misoriented from (0001) towards [1-100] is shown to eliminate rotational twinning. Studies on $B_{12}As_2$ epilayers grown on off-axis c-plane 4H-SiC by SWBXT and HRTEM confirm the single crystalline nature and the absence of twinned domains. Furthermore, no intermediate layer between the epilayer and substrate was observed for $B_{12}As_2$ on off-axis 4H-SiC. The absence of twin variants which dominantly constitute the effects of degenerate epitaxy indicates that the elimination of degenerate epitaxy in the growth of $B_{12}As_2$ was achieved as well on this specific type of substrates. Additionally, low asterism in the $B_{12}As_2$ diffraction spots compared to those grown on other SiC substrates indicates a superior film quality. It is shown that the vicinal steps formed by hydrogen etching on the off-axis 4H-SiC substrate surface before deposition cause the film to adopt a single orientation, a process that is not seen on substrates with either no misorientation, or those tilted toward the [11-20] direction. The ease of nucleation on the ordered step structures present on these unique substrates overrides symmetry considerations that drive degenerate epitaxy and dominates the nucleation process of the $B_{12}As_2$. This work demonstrates that c-plane 4H-SiC with 7° offcut toward [1-100] is potentially a good substrate choice for the growth of high-quality, untwinned $B_{12}As_2$ epilayers for future device applications.

7.2. Introduction

In the absence of native substrates, foreign substrates with compatible structural parameters are necessary for the growth of $B_{12}As_2$ epitaxial films. Hexagonal phases of SiC (a=3.08Å), such as 4H and 6H, have been the substrates of choice since they have approximately half of the basal plane lattice constant of $B_{12}As_2$ (a=6.14Å). To date, this has been attempted on substrates with higher symmetry than $B_{12}As_2$ such as on Si and on-axis 6H-SiC. However, growth of a lower symmetry epilayer on a higher symmetry substrate often produces structural variants (rotational and translational) in the film that are related to each other by a symmetry

operation that is present in the substrate but absent in the epilayer. A theoretical treatment of this phenomenon, which has been referred to as degenerate epitaxy, was carried out by Flynn and Eades. Therefore, degenerate epitaxy, manifested by the presence of high densities of twin boundaries, was observed in all the cases of $B_{12}As_2$ grown on Si with (100), (110) and (111) orientation and c-plane 6H-SiC. The detrimental influence of the results of degenerate epitaxy on $B_{12}As_2$ device performance has made its elimination a primary goal of the $B_{12}As_2$ crystal growth community. Twinning behavior can be diminished by surface roughness or vicinality since the presence of the risers and terraces that comprise the step structures exerts an influence on the nucleation of variants. It has been proposed that m-plane 15R-SiC is potentially a good substrate choice for the growth of untwined $B_{12}As_2$ epilayers. However, due to the limited resource of pure 15R-SiC substrates, it is very important to discover other good substrates which are commercial-available. Therefore, we have explored the use of commercially available SiC substrates with particular offcut direction to explore this ability to manipulate the relative populations of the multiple variants. C-plane 4H-SiC substrate with 7 ° offcut toward [1-100] potentially fulfills this requirement. In this chapter, growth of $B_{12}As_2$ on (0001) 4H-SiC substrates with 7 ° offcut toward [1-100] direction is reported. It is shown that $B_{12}As_2$ grown on (0001) 4H-SiC substrates with 7 ° offcut toward [1-100] is free from structural variants and is of much higher single crystalline quality, in contrast to results from c-plane on-axis 4H-SiC substrate which produced twinned orientations as discussed in Chapter 5. It is shown that the unusual step structures exposed by hydrogen etching of both of these types of substrates promotes nucleation processes that lead to the elimination of the effects of degenerate epitaxy as manifested by the presence of twins.

7.3. Experimental

$B_{12}As_2$ was deposited using chemical vapor deposition (CVD) onto hydrogen-etched c-plane 4H-SiC with 7 ° offcut toward [1-100] direction at 1350 ℃ and 100 Torr of reactor pressure for 2 hours, using 1% B_2H_6 in H_2 and 1% AsH_3 in H_2 as sources. The epitaxial $B_{12}As_2$ film had a nominal thickness of around 4 μm. The film/substrate orientations were determined by synchrotron white beam x-ray topography (SWBXT). Atomic structure of the interface was examined by high resolution transmission electron microscopy (HRTEM) using a JEOL 2100

system and scanning transmission electron microscopy (STEM) using a Hitachi HD 2700C system at Brookhaven National Laboratory.

7.4. Results and discussion

Figure 38 shows a transmission synchrotron x-ray Laue pattern from a $B_{12}As_2$ epitaxial layer grown on an off-axis c-plane 4H-SiC substrate with 7 ° offcut from (0001) toward [1-100] direction recorded with the epilayer as the beam exiting surface. The strong, well-defined 4H-SiC diffraction spots are labeled with indices with subscripts "SiC" while the $B_{12}As_2$ spots are labeled with indices with subscripts "$B_{12}As_2$". The $B_{12}As_2$ produced much stronger and better-defined diffraction spots compared to previous results from $B_{12}As_2$ grown on other SiC substrates. Lower streaking indicated improved mosaicity and decreased strain level. The Laue pattern also lacked any evidence for the existence of twins, indicating the single crystalline nature of the $B_{12}As_2$. The absence of twinning and the lower observed mosaicity in films grown on the off-axis 4H-SiC clearly indicates their much higher quality compared to those grown on on-axis 4H-SiC. Detailed indexing analysis confirms the expected $(0001)_{B12As2}<1\text{-}100>_{B12As2}||(0001)_{4H\text{-}SiC}<1\text{-}100>_{4H\text{-}SiC}$ in epitaxial relationship.

The single crystalline nature and good epilayer quality observed via SWBXT was corroborated with SEM observations (Figure 39) which reveals a relatively smooth and flat surface morphology when even lower voltage and higher magnification was employed in SEM. The absence of the composite structure comprising two types of equilateral triangular feature which correspond to twin related $B_{12}As_2$ domains indicates the lack of rotational variants and the elimination of degenerate epitaxy in the epilayer.

For the $B_{12}As_2$ grown on the off-axis 4H-SiC, excellent crystal quality and the elimination of degenerate epitaxy is also apparent in the HRTEM micrograph shown in Figure 40 (a), which shows a strikingly abrupt, clean interface to the 4H-SiC substrate. SAD patterns from both 4H-SiC and $B_{12}As_2$ were also obtained in which the pattern from $B_{12}As_2$ shows clean diffractions from single orientation. The superior quality of the epilayer and the sharp interface without any transitional layer in between is observed using STEM at the film/substrate interface area (see Figure 41 (a)). According to STEM observation, atomic modeling is generated showing only Si and As atoms which are the only heavy atoms visible under STEM (Figure 41(b)) and the

complete atomic structure is shown in Figure 41 (c). Further microstructural information and investigation, in particular concerning the epilayer/substrate interface and the nucleation mechanisms, was provided by STEM and TEM studies and CrystalMaker simulation carried out on cross-sectional samples.

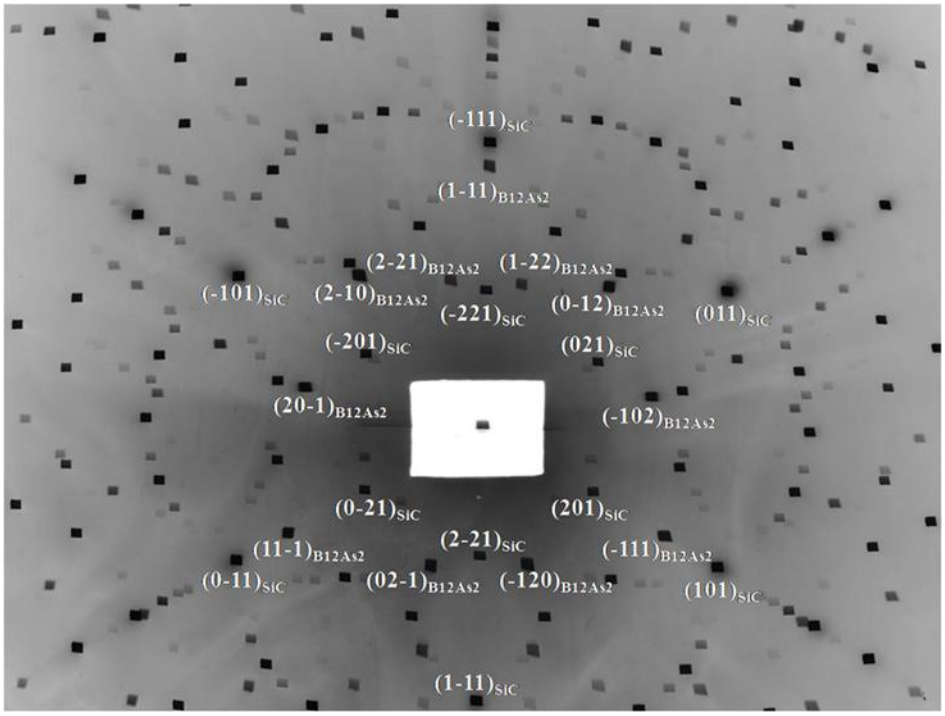

Figure 38 SWBXT Laue pattern of single crystalline $B_{12}As_2$ on off-axis 4H-SiC, with the diffraction peaks marked with rhombohedral (hkl) indices.

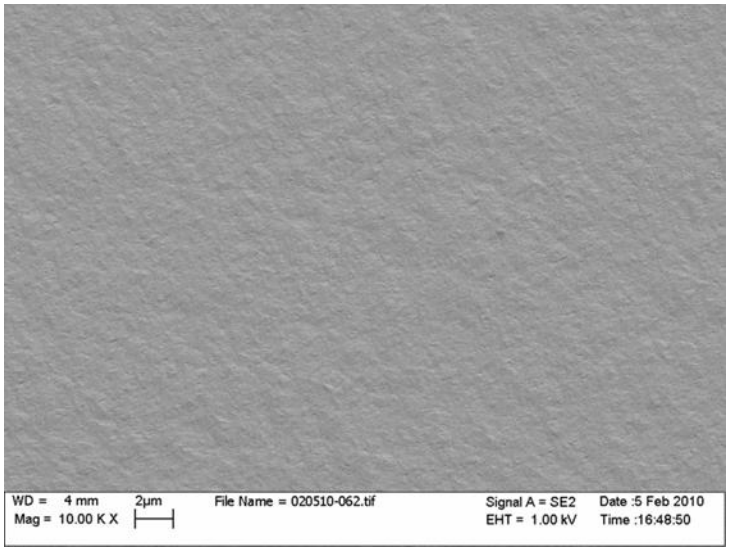

Figure 39 SEM observation of $B_{12}As_2$ epilayer grown on off-axis 4H-SiC under lower voltage and higher magnification.

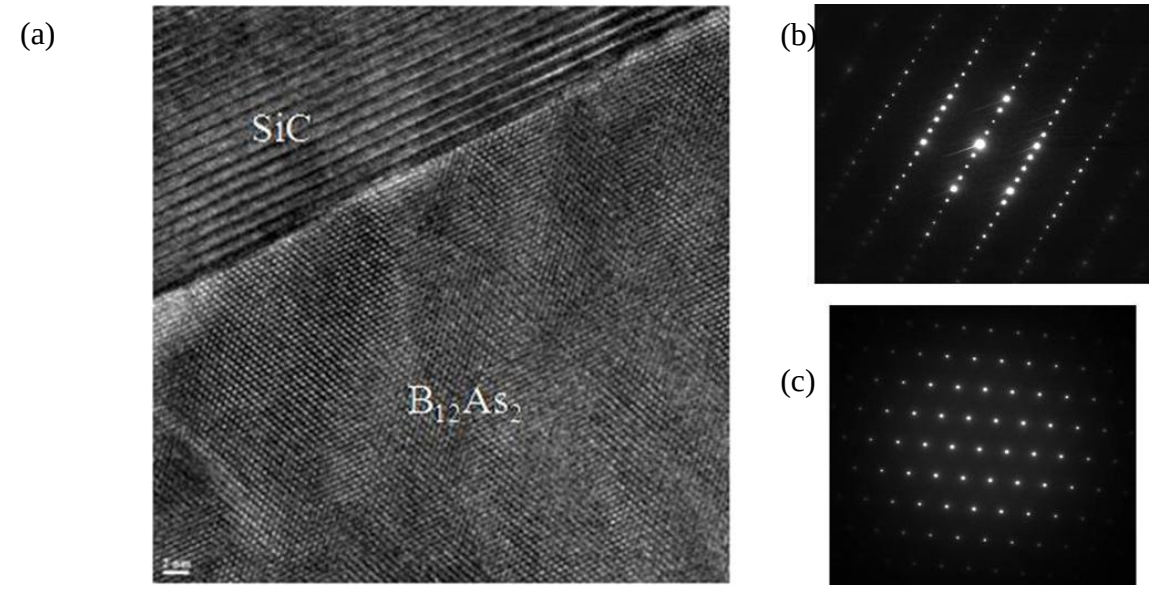

Figure 40 (a) HRTEM image taken along the [10-1] zone axis (equivalent to [11-20] in the hexagonal system) showing a sharp $B_{12}As_2$/off-axis 4H-SiC interface and perfect IBA single crystal; (b) SAD pattern of 4H-SiC substrate; (c) SAD pattern of $B_{12}As_2$ epilayer.

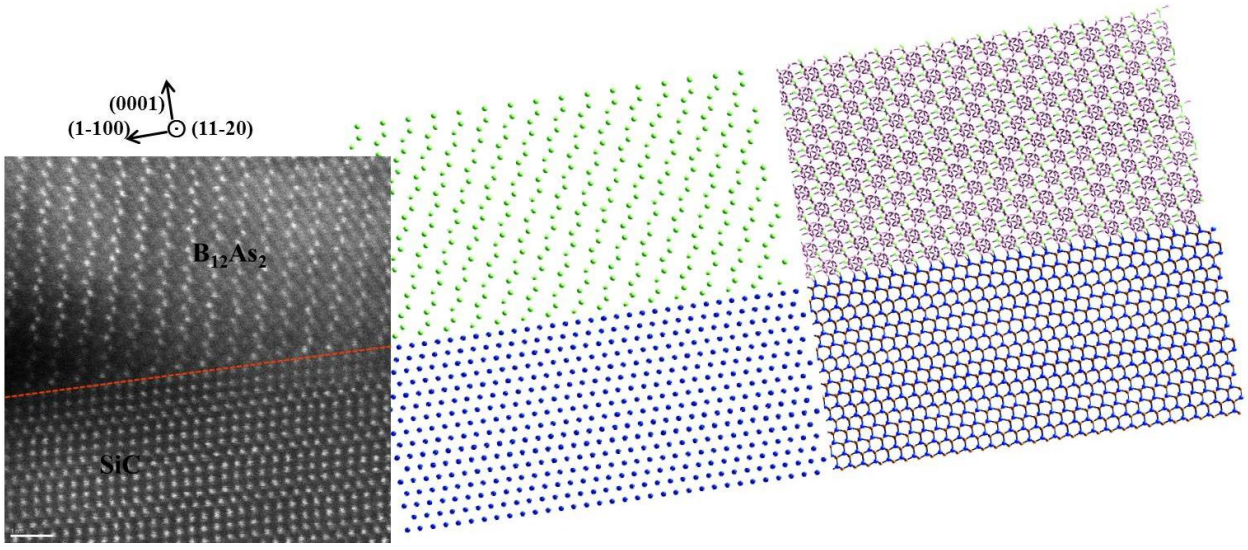

Figure 41 (a) STEM results along film/epilayer interface with [11-20] viewing direction on off-axis 4H-SiC showing the sharp and clear interface and no transitional layer in between. According to STEM observation, atomic modeling is generated showing only Si and As atoms which are the only atoms visible under STEM (b) and the complete atomic structure (c).

The significant improvement in microstructural quality achieved when using off-axis (0001) 4H-SiC substrates with specific [1-100] offcut direction can be understood by considering the step configurations expected to be exhibited on such substrates with 7 °offcut toward [1-100] following hydrogen etching. These step configurations are known to comprise (0001) terraces

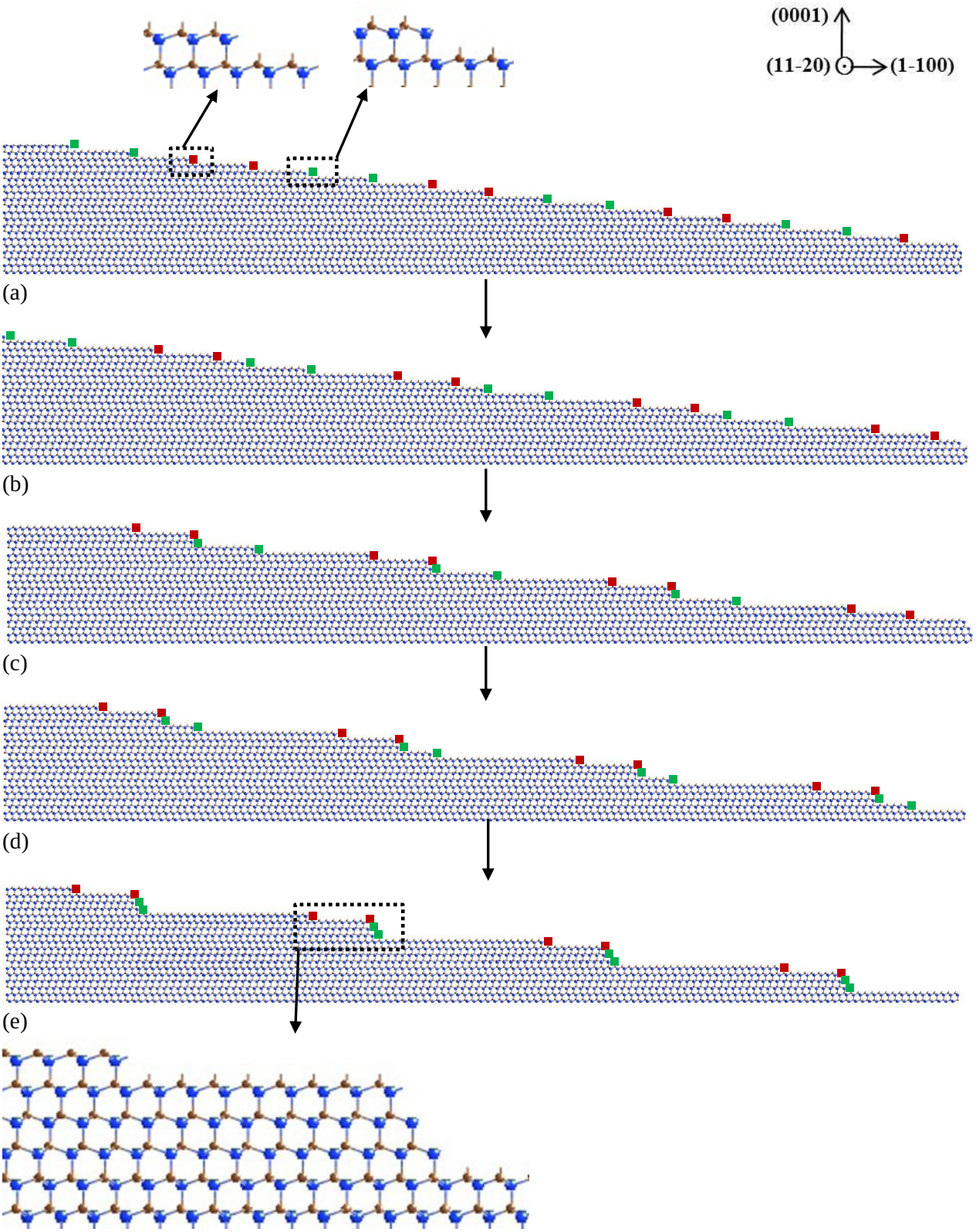

Figure 42 Sequential diagrams showing the evolution of the step configurations created by hydrogen etching of the c-plane 4H-SiC substrate with 7 °offcut toward [1-100] direction.

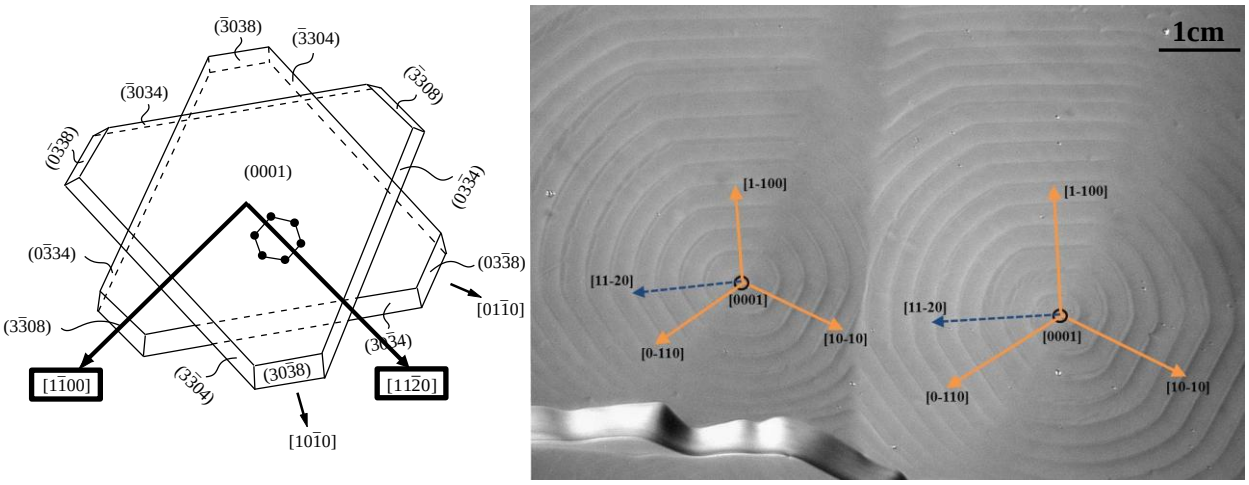

(a) (b)

Figure 43 (a) Surface morphology of half unit cell height steps in 4H-SiC showing the orientations of the various step risers which have (0001) surface projections parallel to <11-20> (perpendicular to <1-100>); (b) Optical image of 4H-SiC boule showing surface morphology consisting of (1-100) type ordered step risers and (11-20) type disordered ones.

and two kinds of single bilayer high (quarter-unit-cell-height) step risers; (-3304) which are close-packed and exhibit single dangling bonds and (-3308) which exhibit double dangling bonds. These are shown schematically in Figure 42 (a) (step risers labeled red and green respectively) which shows that both types of step risers have (0001) surface projections along <11-20> leading to relatively ordered step structures on samples offcut towards [1-100]. This can be contrasted with samples offcut towards [11-20] which will exhibit a much more disordered, zig-zag like step configuration (Figure 43 (a)).

The evidence of surface morphology is shown in Figure 43 (b) which an optical image is taken from the surface of a 4H-SiC boule. The spiral steps shown on the surface consist of two different types: (1-100) type which are ordered steps with straight step risers facing outward (labeled with orange arrows); (11-20) type which are disordered steps with irregular curved step risers facing outward (labeled with dotted blue arrows).

Figure 42 (a) - (e) shows the evolution of the step structure of the substrate with 7 ° offcut towards [1-100] during hydrogen etching. The step risers with double dangling bonds will react with hydrogen and recede simultaneously at twice the velocity of those with single dangling bond. Step risers which are advancing backwards faster will eventually meet the next step riser which is advancing slower and will not be able to recede underneath the next step. Instead, they will slow down to the same receding speed as the next step riser which leads to the step

bunching depicted in Figure 42(e). This results in the isolation of intersections between close packed (-3304) step risers and close packed (0001) terraces.

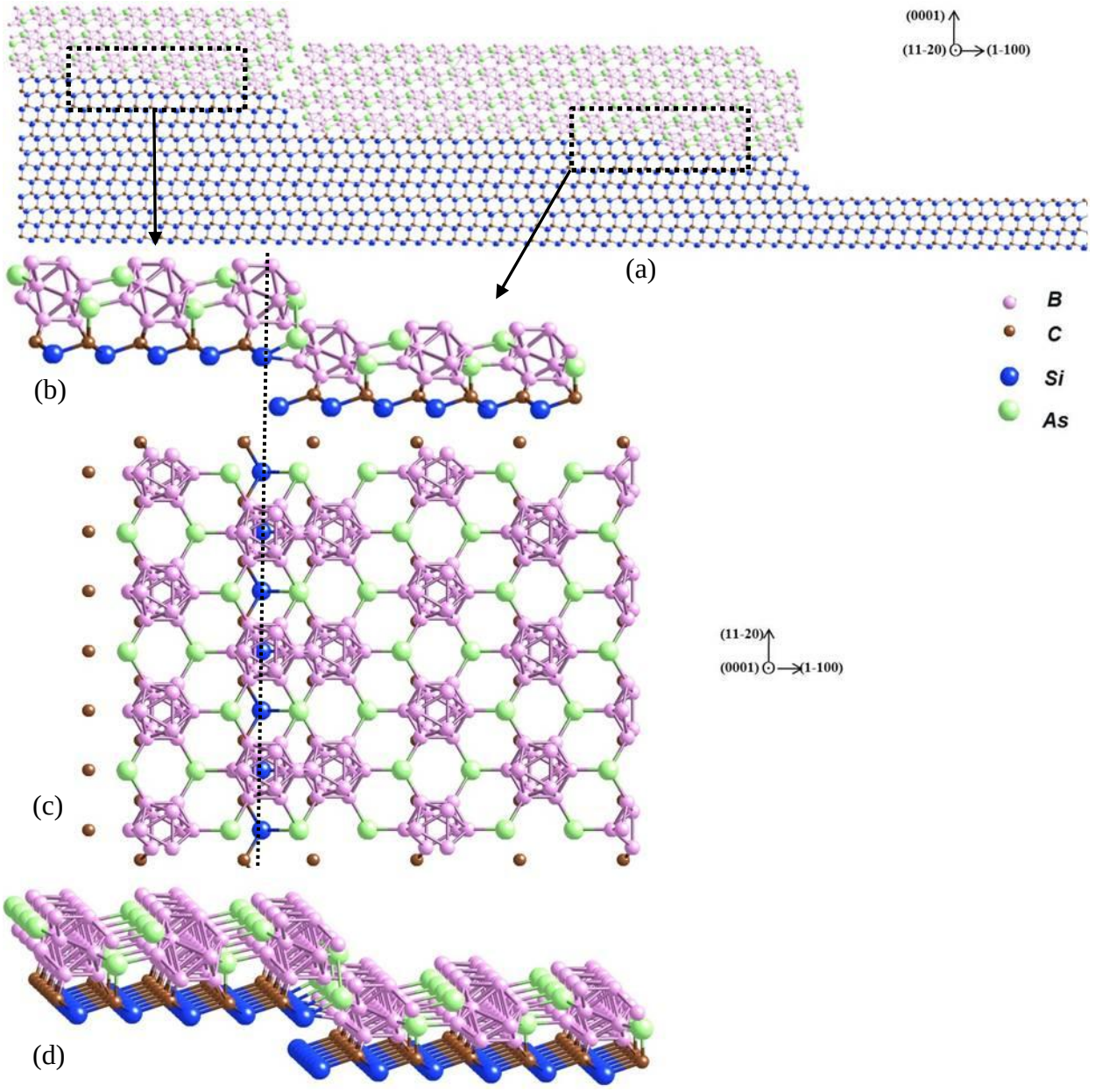

Figure 44 (a) Atomic model of the $B_{12}As_2$/SiC interface showing the nucleation sites; (b) magnified image demonstrating the detailed bonding configurations; (c) and (d) plan view and perspective view of $B_{12}As_2$ nucleated on the surface facets.

During the step flow growth process where $B_{12}As_2$ growth is subsequently carried out, $B_{12}As_2$ molecules that adsorb away from the step risers will generally only be able to weakly

bond to the (0001) terraces from where they will most likely desorb. Considering the dangling bond configurations exhibited at the isolated intersections between the 1/4c height (-3304) risers and the (0001) terraces on the substrate surface and the lattice geometry, $B_{12}As_2$ icosahedra are able to bond to both terrace and the adjacent step riser simultaneously and nucleate the growth process (Figure 44 (a) and (b)). Figure 44 (c) shows in plan-view that the triangular configuration of B atoms at the bottoms of B icosahedra bond to the similarly oriented triangular configurations of C atoms exposed on the (0001) 4H-SiC terrace. This can only happen for one orientation of the $B_{12}As_2$, which precludes the possibility of rotational domain formation or twins and eliminates the effect of degenerate epitaxy. Nuclei are expected to spread in both directions from such locations and eventually coalesce.

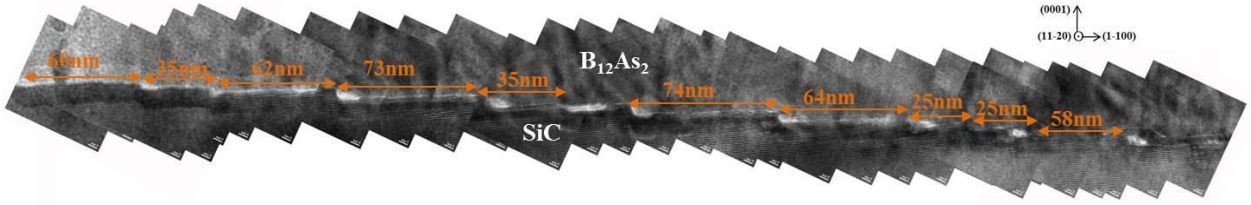

(a)

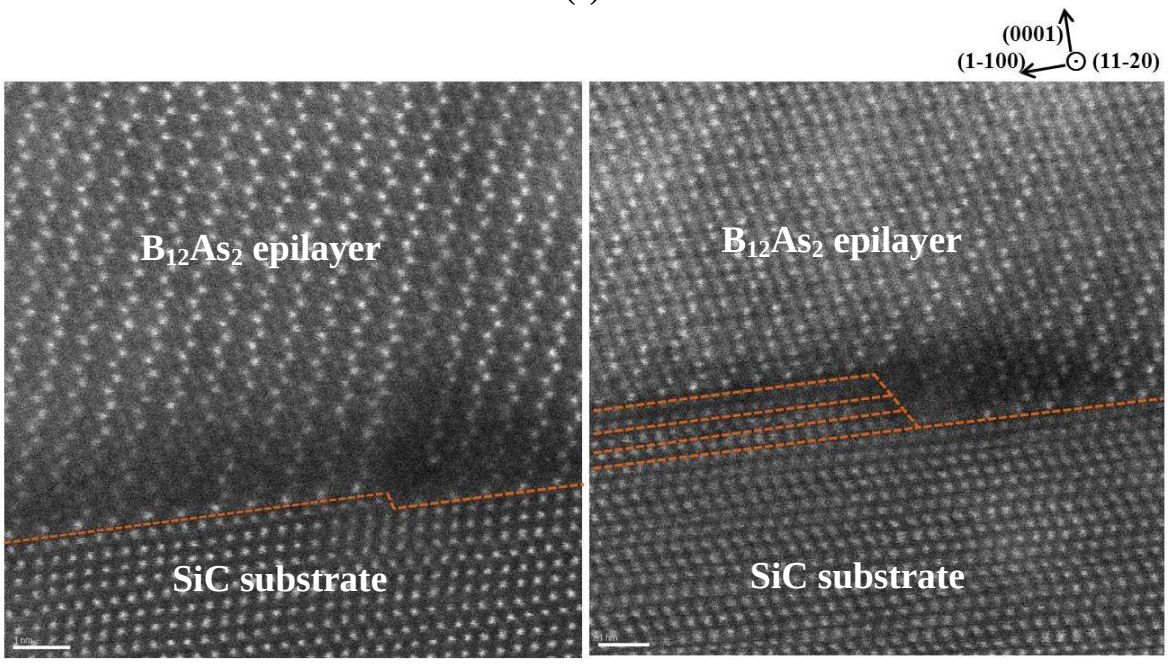

(b) (c)

Figure 45 (a) HRTEM images along the $B_{12}As_2$/SiC interface showing the step structure of the substrate. (b) STEM image taking from the interface showing 1/4c unit cell height step riser. (c) STEM image taking from the interface showing 3/4c unit cell height step riser.

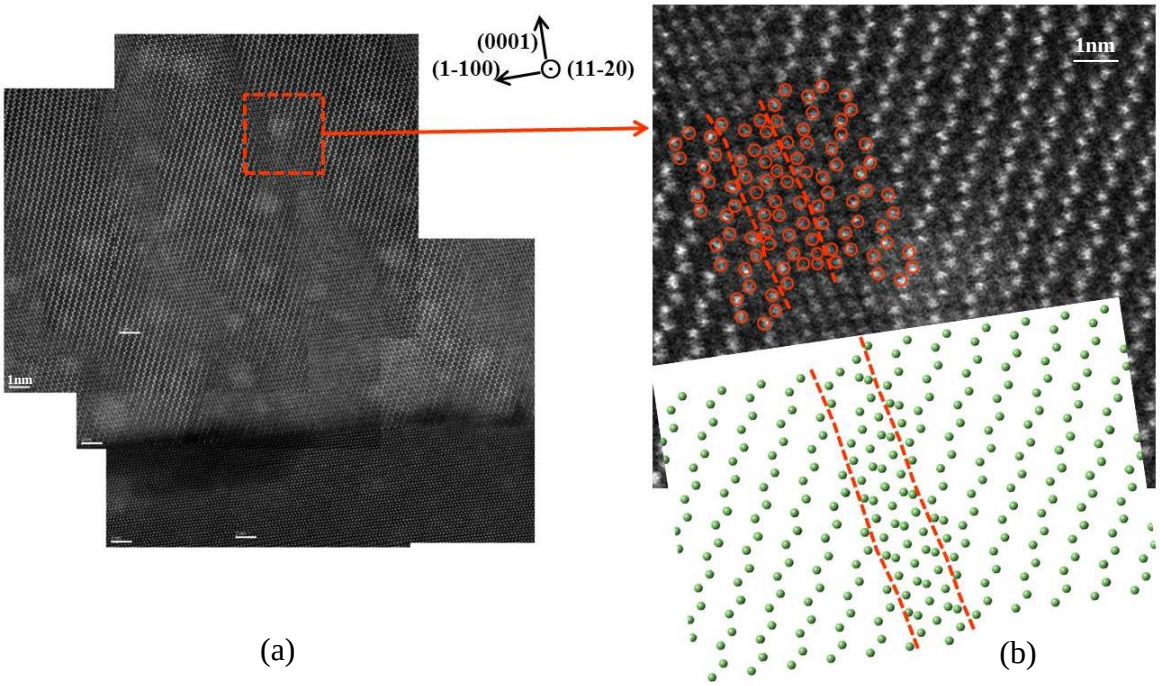

(a) (b)

Figure 46 (a) high magnification STEM image and enlarged image with CrystalMaker simulation (b) showing a translational domain boundary in the $B_{12}As_2$ epilayer.

It is shown that the offcut direction of [1-100] in practice interrupts the six-fold symmetry of the c-plane SiC and consequently creates surface morphology with periodic appearance of terraces and adjacent step risers leading to the elimination of degenerate epitaxy.

Evidence for the presence of these step structures was obtained using HRTEM and STEM (Figure 45). A series of HRTEM images were recorded along the film/substrate interface and then pieced together (Figure 45(a)). The clean interface and ordered step structures which consist of large step risers with 3/4 unit cell height and small step risers with 1/4 unit cell height are observed. The average terrace width between adjacent risers is around 60nm which corresponds to 3/4c unit cell high step risers and is in good agreement with the step flow theory. Figure 45 (b) shows an STEM image taking from the interface where a 1/4c step riser is observed while in Figure 45 (c), a 3/4 unit cell high step riser is observed. Note that only Si and As atoms can be distinguished under STEM.

The slight diregistry between domains which expand and coalesce from such nucleation sites can lead to the formation of translational domain boundaries (see Figure 46) while the in-plane mismatch between substrate and the film (~3.7%) can be accommodated by networks of interfacial dislocations.

7.5. Conclusion

In conclusion, epitaxial growth of $B_{12}As_2$ on c-plane (0001) 4H-SiC substrate with 7 ° offcut toward [1-100] has been discussed. SWBXT, cross-sectional HRTEM and STEM revealed single crystal, untwinned (111) oriented $B_{12}As_2$ and the elimination of degenerate epitaxy. It is proposed that the single crystalline, untwinned nature of the $B_{12}As_2$ film resulted from the tendency to nucleate on the isolated junctions between close-packed (-3304) step risers and (0001) terraces present on the hydrogen etched offcut 4H-SiC surface and the absence of degenerate epitaxy is attributed to the introduced vicinality of c-plane 4H-SiC substrate with 7 ° offcut toward [1-100] direction. It is also proposed that the absence of degenerate epitaxy is attributed to the introduced vicinality of c-plane 4H-SiC substrate with 7 ° offcut toward [1-100] direction.

8. Conclusions

Defect structures and growth mechanisms of $B_{12}As_2$ epilayers grown on on-axis c-plane 6H-SiC, on-axis c-plane 4H-SiC and off-axis c-plane 4H-SiC with 7 ° offcut toward [1-100] have been studied using SWBXT, SEM, HRTEM, STEM and CrystalMaker software.

I) For the growth on on-axis c-plane 6H-SiC, the epitaxial relation between film and substrate is identified as $(0001)_{B12As2}<11\text{-}20>_{B12As2}||(0001)_{6H\text{-}SiC}<11\text{-}20>_{6H\text{-}SiC}$. The $B_{12}As_2$ epilayer is twinned and the twin relationship consisted of a 180° (or equivalently 60°) rotation about $[0001]_{B12As2}$. The observed differences in microstructures were correlated with the differences in nucleation at the two growth temperatures. The effect of the difference in microstructure on macroscopic properties of the $B_{12}As_2$ was illustrated using the example of thermal conductivity which was measured using the 3-ω technique.

II) A new model is presented for the nucleation mechanism of 6H-SiC polytype inclusions in Physical Vapor Transport (PVT) grown 15R-SiC boules. Inhomogeneous densities of screw dislocations replicated from the seed lead to uneven growth rates in the boule resulting in a quasi-vicinal growth surface. Subsequent interference between advancing vicinal growth steps and screw dislocation spiral growth steps lead to complex step overgrowth processes which can suppress all or part of the 15R 1c screw dislocation Burgers vector through the creation of Frank faults and Frank partial dislocations on the basal plane. Combined with stacking shifts induced by the passage of basal plane partial dislocations it is shown that suppression of 9/15 of the 15R 1c dislocation Burgers vector by such step overgrowth can leave behind a residual Burgers vector corresponding to a 1c dislocation in 6H-SiC. The residual dislocation then acts as a nucleus for reproduction of the 6H SiC structure at the surface of the 15R crystal.

III) A detailed analysis of the microstructure in $B_{12}As_2$ epitaxial layers grown by CVD on on-axis (0001) 4H-SiC substrates is presented. Synchrotron white beam x-ray topography (SWBXT) enabled macroscopic characterization of the substrate/epilayer ensembles and revealed the presence of a quite homogenous solid solution of twin and matrix epilayer domains forming a submicron mosaic structure. The basic epitaxial relationship was found to be

$(0001)_{B12As2}$<1-100>$_{B12As2}$||$(0001)_{4H\text{-}SiC}$<1-100>$_{4H\text{-}SiC}$ and the twin relationship comprised a 180° (or equivalently 60°) rotation about $[0001]_{B12As2}$ in agreement with previous reports. Cross-sectional high resolution transmission electron microscopy (HRTEM) and scanning transmission electron microscopy both revealed the presence of an ~20nm thick, disordered transition layer which is shown to be created by the coalescence of a mosaic of translational and rotational variant domains nucleated at the various types of nucleation site available on the (0001) 4H-SiC surface. In this transition layer, competition between the growth of the various domains is mediated in part by the energy of the boundaries created between them as they coalesce. Boundaries between translational variant domains are shown to have unfavorable bonding configurations and hence high energy. These high energy boundaries can be eliminated during mutual overgrowth by the generation of a $1/3[0001]_{B12As2}$ Frank partial dislocation which effectively eliminates the translational variants. This leads to an overall improvement in film quality beyond thicknesses of ~20nm as the translational variants grow out leaving only the twin variants. (0003) twin boundaries in the regions beyond 20nm are shown to possess fault vectors such as $1/3[1\text{-}100]_{B12As2}$ which are shown to originate from the mutual shift between the nucleation sites of the respective domains.

IV) Epitaxial growth of $B_{12}As_2$ on 4H-SiC substrates intentionally misoriented from (0001) towards [1-100] is shown to eliminate rotational twinning. Studies on $B_{12}As_2$ epilayers grown on off-axis c-plane 4H-SiC by SWBXT and HRTEM confirm the single crystalline nature and the absence of twinned domains. Furthermore, no intermediate layer between the epilayer and substrate was observed for $B_{12}As_2$ on off-axis 4H-SiC. The absence of twin variants which dominantly constitute the effects of degenerate epitaxy indicates that the elimination of degenerate epitaxy in the growth of $B_{12}As_2$ was achieved as well on this specific type of substrates. Additionally, low asterism in the $B_{12}As_2$ diffraction spots compared to those grown on other SiC substrates indicates a superior film quality. It is shown that the vicinal steps formed by hydrogen etching on the off-axis 4H-SiC substrate surface before deposition cause the film to adopt a single orientation, a process that is not seen on substrates with either no misorientation, or those tilted toward the [11-20] direction. The ease of nucleation on the ordered step structures present on these unique substrates overrides symmetry considerations that drive degenerate epitaxy and dominates the nucleation process of the $B_{12}As_2$. This work demonstrates that c-plane

4H-SiC with 7° offcut toward [1-100] is potentially a good substrate choice for the growth of high-quality, untwinned $B_{12}As_2$ epilayers for future device applications.

9. Future work

In Chapter 5, a new model was proposed for the nucleation mechanism of 6H-SiC polytype inclusions during the step flow growth of SiC crystal. This model is possible to be extended to polytype transformations in SiC crystals of different polytypes and even different crystals with similar structures. It is promising to study more crystals and build a comprehensive theory for polytype transformation in semiconductor materials in order to produce high quality single crystals for device fabrications.

In Chapter 7, high quality single crystal growth of $B_{12}As_2$ has been shown to be achieved on c-plane 4H-SiC substrates with 7 °offcut from (0001) toward (1-100). However, the thickness of the film is only about 4 μm, it remains uncertain that if the excellent quality of single crystal $B_{12}As_2$ can be extended to a thicker epilayer for device fabrication.

It has been shown that 7 ° offcut angle on the c-plane 4H-SiC substrate surface have significant effect in reducing the number of possible structural variants in the film and the width of each single step on the substrate surface is just enough to accommodate four B icosahedra. Unfortunately, this type of offcut angle is not commonly used in the SiC growth industry. A smaller offcut angle, i.e., 4 °, is used more widely. This offcut angle can provide wider terrace of each step on the substrate surface, which may also contribute to alleviating the problem of structural variants due to the specific offcut direction or, may accommodate more than one orientation of $B_{12}As_2$. In consequence, it is of great importance to study the effect of a smaller offcut angle on the epitaxial growth of $B_{12}As_2$ and to find the optimized offcut angle.

$B_{12}As_2$ has been proposed to be potentially useful for the application of high temperature semiconductor devices and electronics operating in radiation environments. It will be instructive to fabricate $B_{12}As_2$ devices so as to study the device performance and their behavior under electron irradiation.

References

1. W. J. Choyke, H. Matsunami and G. Pensl editors, *Silicon Carbide* (Springer, 2004)

2. O. Ambacher, *J. Phy. D. Appl. Phys.*, **31**, 2653 (1998)

3. D. C. Look, *Mater. Sci. Eng.* **B 80**, 383 (2001)

4. D. Emin, *Physics Today*, **55**, January (1987)

5. D. Emin, *J. Sol. Sta. Chem.*, **177**, 1619 (2004)

6. S. Bakalova, Y. Gong, C. Cobet, N. Esser, Y. Zhang, J. H. Edgar, Y. Zhang, M. Dudley, and M. Kuball, *Phys. Rev. B*, **81**, 075114 (2010)

7. G.A. Slack, T.M. McNelly, and E.A. Taft, *J. Phys. Chem. Solids*, **44**, 1009 (1983).

8. Ordered Boron Arsenide, P. D. Ownby, *Journal of the American Ceramic Society*, **58**, 7-8, 359 (1975)

9. Y. Gong, M. Tapajna, S, bakalova, Y. Zhang, J. H. Edgar, Y. Zhang, M. Dudley, M. Hopkins and M. Kuball, *Appl. Phys. Lett.* **96**, 223506 (2010).

10. M. Carrard, D. Emin and L. Zuppiroli, *Phys. Rev. B*, **51**(17), 11270 (1995).

11. D. Emin and T. L. Aselage, *J. App. Phys.*, **97**, 013529 (2005)

12. J.R. Michael, T. L. Aselage, D. Emin and P.G. Kotula, *J. Mater. Res.*, **20** (11), 3004 (2005).

13. D. Emin, *J. Sol. Sta. Chem.*, **179**, 2791 (2006)

14. R.H. Wang, D. Zubia, T. O'Neil, D. Emin, T. Aselage, W. Zhang and S.D. Hersee, *J. Electronic Materials*, **29** (11), 1304 (2000)

15. W.M. Vetter, R. Nagarajan, J. H. Edgar and M. Dudley, *Mater. Lett.*, **58**, 1331 (2004)

16. P. Rappaort, J. J. Loferski and E. G. Linder, *RCA Rev.*, **17**, 100 (1956)

17. V. F. Sears, *Neutron News* **3**, 26 (1992).

18. Z. Xu, J. H. Edgar and S. Speakman, *J. Crystal Growth.*, **293**, 162 (2006)

19. H. Chen, G. Wang, M. Dudley, L. Zhang, L. Wu, Y. Zhu, Z. Xu, J.H. Edgar and M. Kuball, *J. Appl. Phys.*, **103** (12), 123508 (2008)

20. S.W. Chan, *J. Phys. Chem. Solids*, **55**, 1137 (1994)

21. C. P. Flynn and J. A. Eades, *Thin Soild Films*, **389**, 116 (2001)

22. R. Nagarajan, Z. Xu, J. H. Edgar, F. Baig, J. Chaudhuri, Z. Rek, E. A. Payzant, H. M. Meyer, J. Pomeroy and M. Kuball, *J. Crystal Growth.*, **273**, 431 (2005)

23. H. Baumhauer, Z. Krist. 50 (1912) 33.

24. W. Shockley, *Introductory Remarks, in: Silicon Carbide: A high Temperature Semiconductor*, Eds. J.R. O'Connor and J. Smiltens (Pergamon, Oxford, 1960).

25. See the various papers in: P. Krishna, Ed., *Progress in Crystal Growth and Characterization*, Vol. **7** (Pergamon, Oxford, 1983)

26. L. S. Ramsdell, *American Mineralogist,* **32**, 64 (1947)

27. A. Verma and P. Krishna, *Polymorphism and Polytypism in Crystals* (Wiley, New York, 1966)

28. N. W. Jepps and T. Page, *in: Progress in Crystal Growth and Characterization*, Vol. **7**, Ed. P. Krishna (Pergamon, Oxford, 1983) pp. 259-306

29. J.A. Powell, P. Pirouz and W.J. Choyke, *in: Semiconductor Interfaces, Microstructure and Devices: Properties and Applications*, Ed. Z. C. Feng (Hilger, Bristol, 1992)

30. M. Dudley, X.R. Huang, W. Huang, A. Powell, S. Wang, P. Neudeck, M. Skowronski, *Appl. Phys. Lett.*, **75**, 784-786 (1999)

31. P. Pirouz and J.W. Yang, *Ultramicroscopy*, **51**, 189-214 (1993)

32. P. Pirouz, M. Zhang, J.L. Dement and H.M. Hobgood, *J. Appl. Phys.***, 93**, 3279 (2003)

33. Y. Chen, G. Dhanaraj, W. Vetter, R. Ma, M. Dudley, *Mater. Sci. Forum*, Vols.**556-557**, 231-234 (2007)

34. H. Chen, G. Wang, M. Dudley, Z. Xu, J. H. Edgar, T. Batten, M. Kuball, L. Zhang, and Y. Zhu, *Appl. Phys. Lett.*, **92** (23), 231917 (2008)

35. A. Authier, in "*Dynamical Theory of X-ray Diffraction*", Oxford University Press, 2001 pp. 46

36. D. K. Bowen and B. K. Tanner, in "*High Resolution X-Ray Diffractometry and Topography*", Taylor & Francis, 1998 pp. 74

37. A. Authier, in "*Dynamical Theory of X-ray Diffraction*", Oxford University Press, 2001 pp. 104-106

38. B. D. Cullity, in "*Elements of X-ray Diffraction*", Addison-Wesley Publishing Company, Inc., 1977 pp. 120

39. D. K. Bowen and B. K. Tanner, in "*High Resolution X-Ray Diffractometry and Topography*", Taylor & Francis, 1998 pp. 225

40. D. K. Bowen and B. K. Tanner, in "*High Resolution X-Ray Diffractometry and Topography*", Taylor & Francis, 1998 pp. 173

41. M. Dudley and X. Huang, *Materials Science Forum* 338, 431, 1998.

42. X. R. Huang, M. Dudley, W. M. Vetter, et al., *J. App. Crys.*, **32**, 516 (1999)

43. M. Dudley, X. R. Huang and W. Huang, *J. Phys. D: App. Phys.*, **32**, A139 (1999)

44. X. R. Huang, M. Dudley, J. Y. Zhao, *Philosophical Transactions of the Royal Society of London. A*, **357**, 2659, (1999)

45. Cahill and Pohl, *Phys. Rev.*, B **35**, 4067 (1987)

46. Cahill et al., *Rhys. Rev.*, B **50**, 6077 (1994)

47. Roberto Otero, Frauke Hümmelink, Fernando Sato, Sergio B. Legoas, Peter Thostrup, Erik Lægsgaard, Ivan Stensgaard, Douglas S. Galvão and Flemming Besenbacher, *Nature Materials*, **3**, 779 - 782 (2004)

48. T. Borca-Tasciuc et al., *Review of Scientific Instruments*, **72**, 2139 (2001)

49. J. M. Cowley and A. F. Moodie, *Acta Cryst.*, **10**, 609 (1957)

Appendix I. Conversion between the stereoprojections of rhombohedral system and hexagonal system

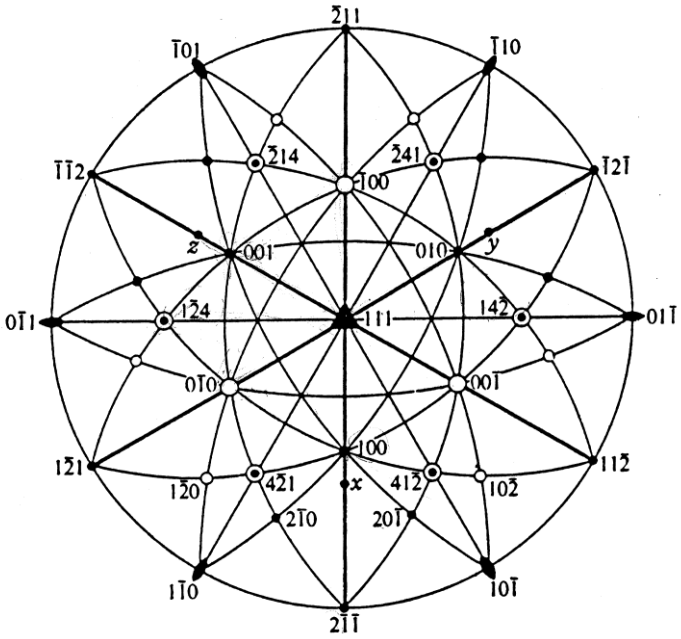

Stereo projection of rhombohedral system

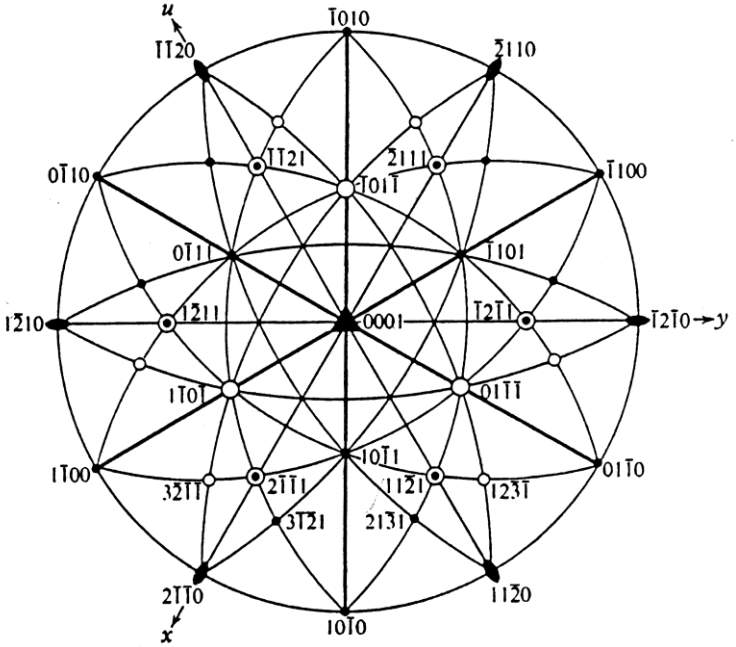

Stereo projection of hexagonal system

Appendix II. Unit cells of $B_{12}As_2$, 6H-SiC and 15R-SiC generated by CaRine4.0

1. $B_{12}As_2$

a	b	c	
5.3370	5.3370	5.3370	(Å)

α	β	γ	
70.216	70.216	70.216	(°)

Atom	X	Y	Z	Occupation
As	0.39999	0.39999	0.39999	1
As	0.60001	0.60001	0.60001	1
B	0.8208	0.8208	0.2755	1
B	0.2755	0.8208	0.8208	1
B	0.8208	0.2755	0.8208	1
B	0.1792	0.1792	0.7245	1
B	0.7245	0.1792	0.1792	1
B	0.1792	0.7245	0.1792	1
B	0.9826	0.9826	0.6755	1
B	0.6755	0.9826	0.9826	1
B	0.9826	0.6755	0.9826	1
B	0.0174	0.0174	0.3245	1

B	0.3245	0.0174	0.0174	1
B	0.0174	0.3245	0.0174	1

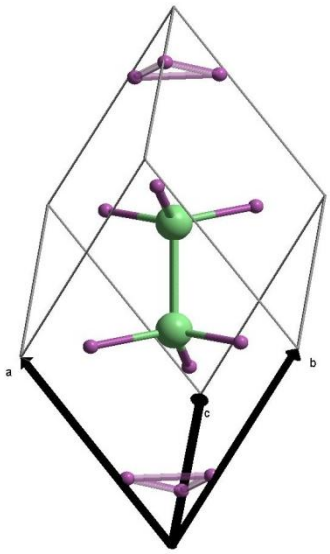

2. 6H-SiC

a	b	c	
3.0806	3.0806	15.1173	(Å)

α	β	γ	
90	90	120	(°)

Atom	X	Y	Z	Occupation
C	0	0	0.125	1

C	0	0	0.625	1
C	0.333333	0.666667	0.458333	1
C	0.333333	0.666667	0.791667	1
C	0.666667	0.333333	0.958333	1
C	0.666667	0.333333	0.219667	1
Si	0	0	0	1
Si	0	0	0.5	1
Si	0.333333	0.666667	0.333333	1
Si	0.333333	0.666667	0.666667	1
Si	0.666667	0.333333	0.166667	1
Si	0.666667	0.333333	0.833333	1

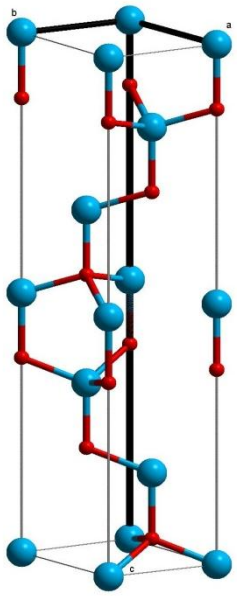

3. 15R-SiC

a	b	c	
12.69	12.69	12.69	(Å)

α	β	γ	
13.917	13.917	13.917	(°)

Atom	X	Y	Z	Occupation
Si	0.00000	0.00000	0.00000	1
Si	0.13333	0.13333	0.13333	1
Si	0.40000	0.40000	0.40000	1
Si	0.60000	0.60000	0.60000	1
Si	0.86667	0.86667	0.86667	1
C	0.05000	0.05000	0.05000	1
C	0.18333	0.18333	0.18333	1
C	0.45000	0.45000	0.45000	1
C	0.65000	0.65000	0.65000	1
C	0.91667	0.91667	0.91667	1

Appendix III. Simulated selective area diffraction (SAD) patterns of $B_{12}As_2$ along various zone axes

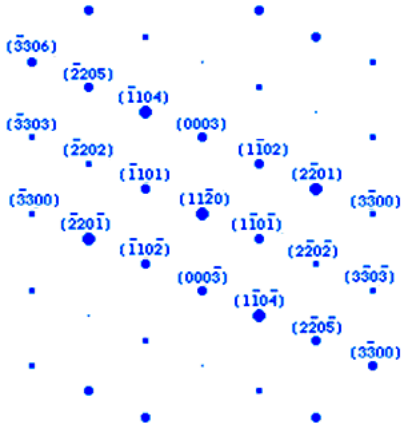

(11-20) SAD pattern

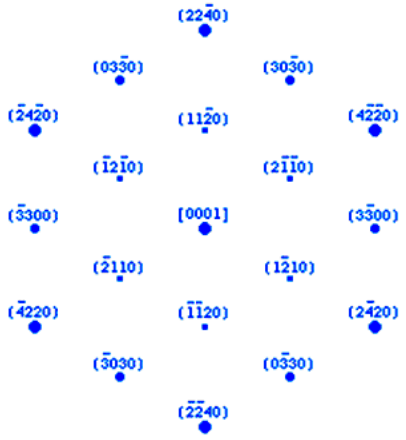

(0001) SAD pattern

(1-100) SAD pattern

Appendix IV. Stereoprojections of $B_{12}As_2$

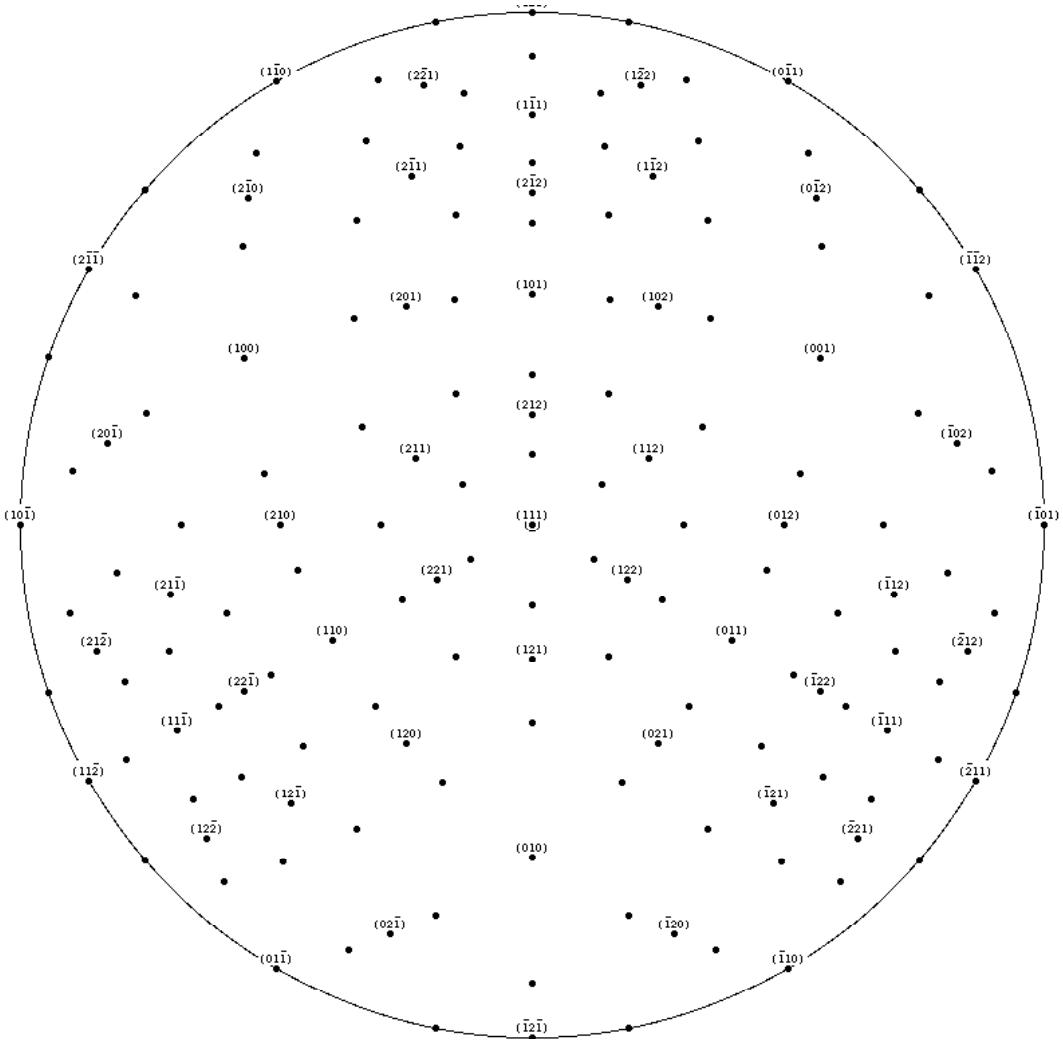

(111) stereo projection

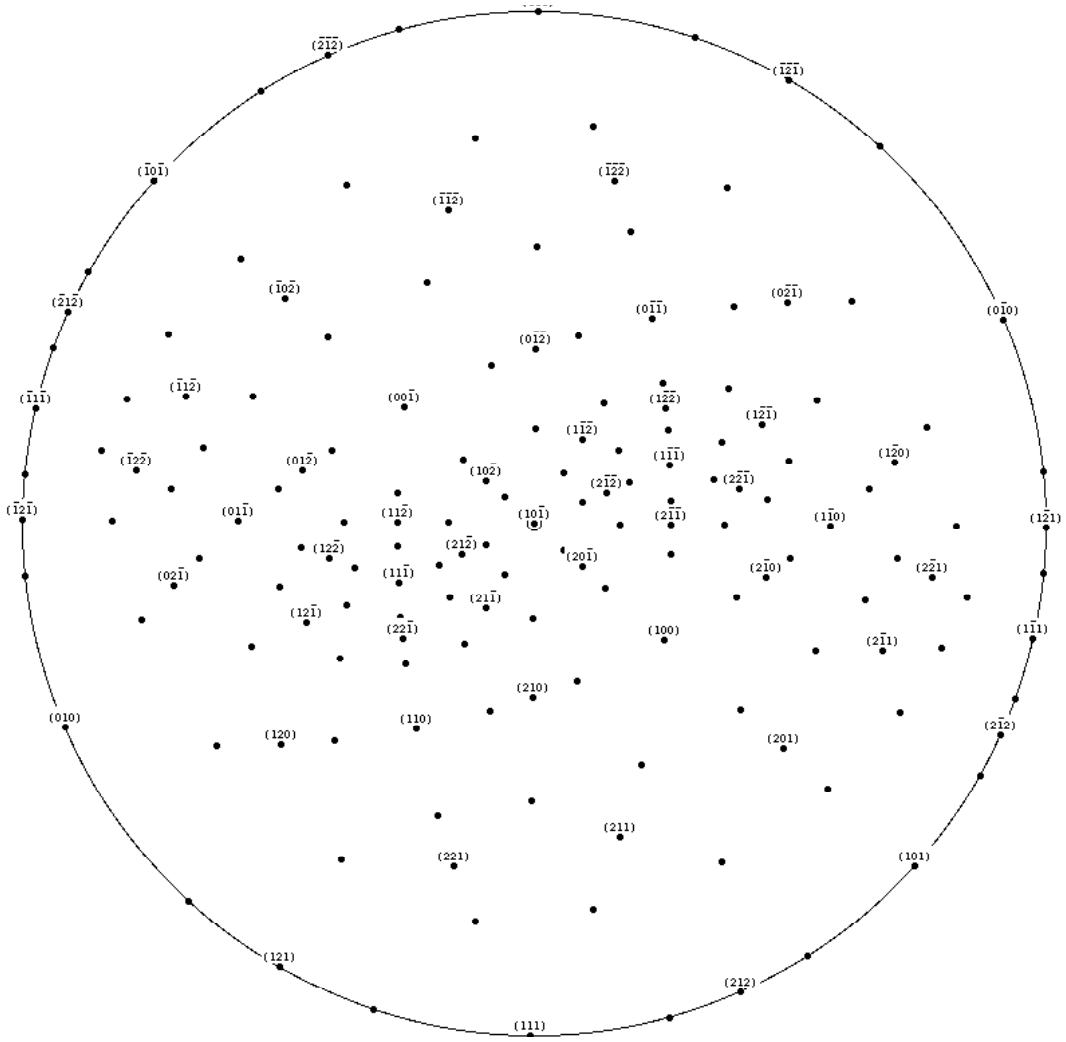

(10-1) stereo projection

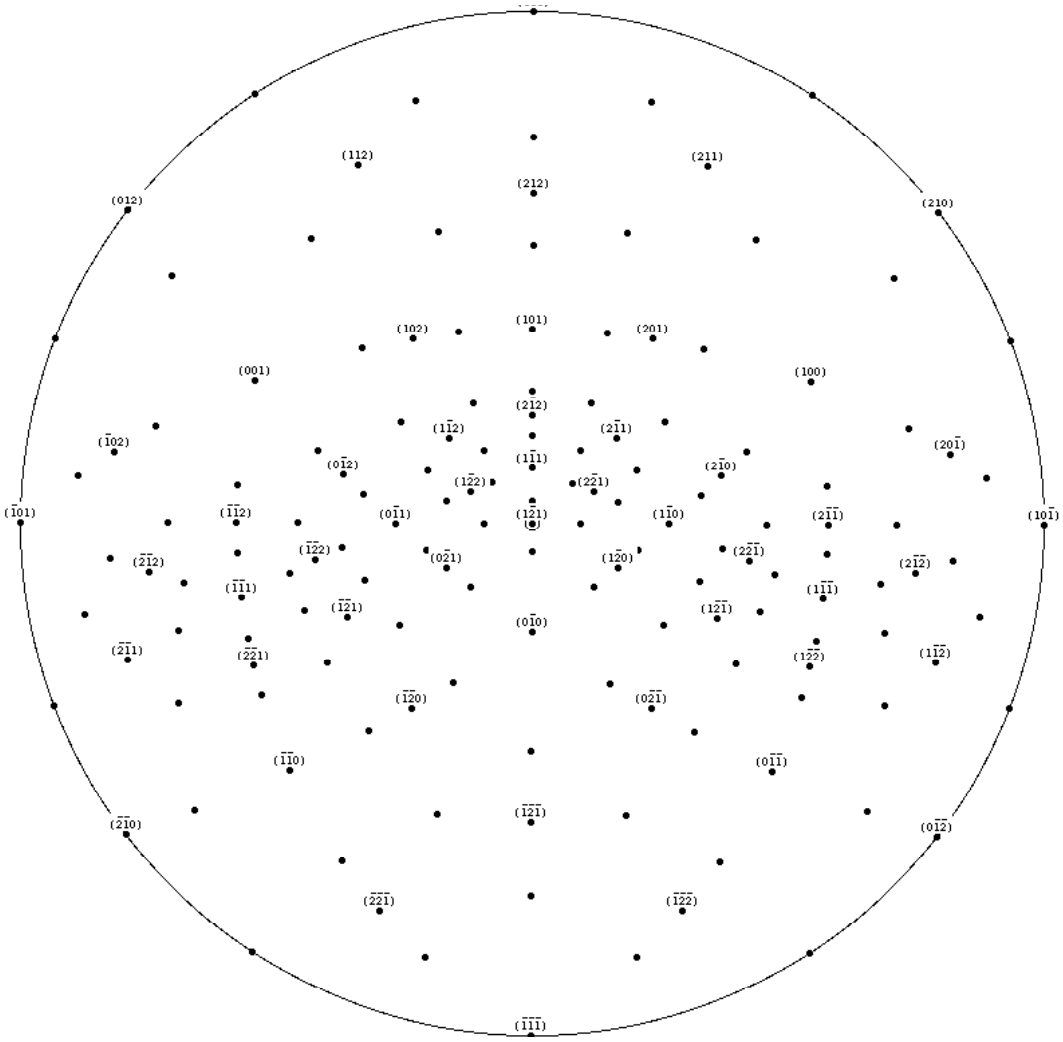

(1-21) stereo projection